FABRICATION OF GRAPHENE BASED DEVICES AND STUDY OF THEIR ELECTRICAL AND OPTICAL PROPERTIES

UNIVERSITÀ DEGLI STUDI DI SALERNO

Facoltà di Scienze Matematiche Fisiche e Naturali

A thesis submitted for the degree of
Doctor of Philosophy
in Teorie, metodologie e applicazioni avanzate per la comunicazione, l'informatica e la fisica (XI Ciclo – Nuova Serie)

Coordinatore del Dottorato:
Prof. Giuseppe Persiano
Università di Salerno

Candidato:
Dott. Salvatore Santandrea

Relatore:
Prof. Antonio Di Bartolomeo
Università di Salerno

ANNO ACCADEMICO **2012 / 2013**

Chapter 1
General Introduction

1.1. Motivation

Carbon nanostructures, playing a central role in nanomaterials science and nanotechnology, are very attractive systems due to the wide diversity of their structural forms and peculiar properties.

When Lavoisier listed "Carbone" in his "Traite´ Elèmentaire de Chimie" as one of the newly identified chemical elements, for the first time just 220 years ago, he had already identified the versatility of carbon since he had shown that it was the elementary component of both diamond and graphite [1].

Since then, more allotropes of carbon have been reported and a large scientific community has been passionate about deciphering the properties of this element that can adopt many structures ranging from diamond and graphite (3D) to graphene (2D) [2], nanotubes (1D) [3] or fullerenes (0D) [4] as illustrated in **Fig. 1**.

The former three-dimensional allotropes have been known and widely used for centuries, whereas fullerenes and nanotubes have been only discovered and studied in the last two decades. With the exception of diamond, it is possible to think of fullerenes, nanotubes and graphite as different structures built from the same hexagonal array of sp^2 carbon atoms, namely graphene. Indeed, fullerenes and nanotubes can be mentally visualized as a graphene sheet rolled into a spherical and cylindrical shape, respectively, and graphite can be described as a stack of alternately shifted graphene sheets.
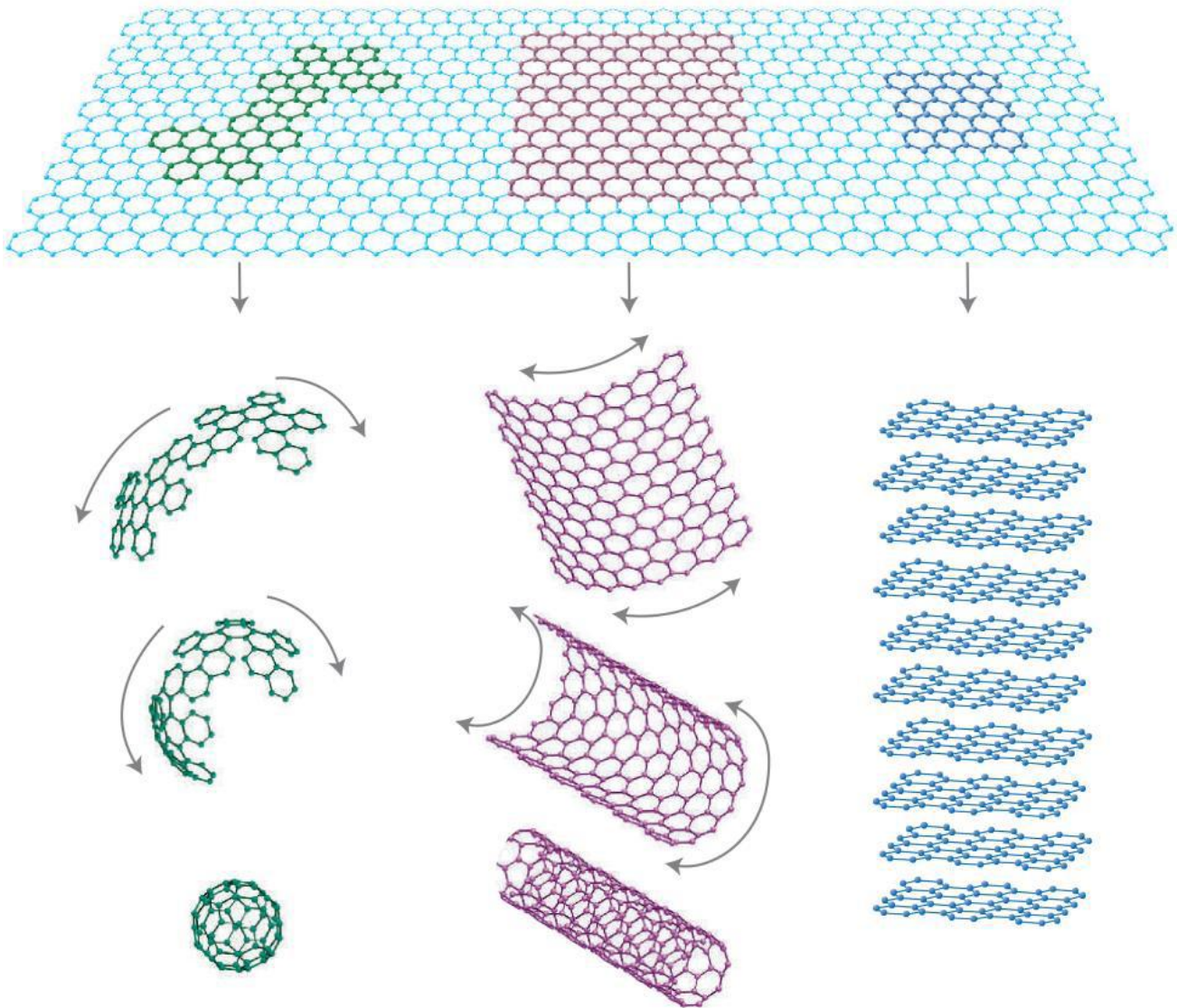
Figure 1. Graphene is a 2D building material for carbon materials of all other dimensionalities. Low-dimensional carbon allotropes: fullerene (0D),carbon nanotube (1D) and graphene (2D),[5].

The 2010 Nobel Prize in Physics honored Andre K. Geim and Konstantin S. Novoselov, who succeeded in producing, isolating, identifying, and characterizing graphene, [6].

The experimental isolation of single-layer graphene first and foremost yielded access to a large amount of interesting physics [8,9]. Initial studies included observations of graphene's ambipolar field effect [2], the quantum Hall effect at room temperature [10-15], measurements of extremely high carrier mobility [16,17-19] and even the first ever detection of single molecule adsorption events [20,21]. These properties generated huge interest in the possible implementation of graphene in a myriad of devices, in part because two-dimensional crystals were thought to be thermodynamically unstable at finite temperatures [22,23].

The linear energy dispersion relation at low energies is a unique property among all known materials and it is an attractive one because it makes electron motion mimic the properties of photons. The practical consequence of this fact is the very high charge carrier mobility [24,25,26]. Infinitely large sheets of graphene are inherently two dimensional (2D) with zero bandgap.

The high mobility, the high current carrying capacity [27], the 2D or 1D atomic structure and the compatibility with planar technology makes graphene an exciting and promising addition to silicon-based CMOS. The novel band structure holds promise for as-yet unrealized devices that exploit the massless Dirac-fermion like linear energy dispersion of electrons in the material.

There are a number of motivations for using graphene-based devices in future nanotechnologies. Among them, the use of graphene can improve the electronic devices intrinsic performance and power efficiency or enable new functionalities, such as ultra-high-sensitivity detection for chemical and biological applications.

So far most of the research efforts on graphene-based electronics have been directed towards digital applications. However, conventional or even tunnel-based graphene FETs suffer from the lack of a well-defined energy gap, ultimately leading to poor on/off current ratios unless extremely narrow (1-2 nm) graphene nanoribbons are used as channel material. In analog applications, where the FET is used as an amplifier, the on/off problem is much more relaxed and the huge potential of graphene can be fully exploited.

In particular, the most promising analog applications for graphene electronics can be identified in high frequency low-noise amplifiers and/or power amplifiers, where the experimentally verified exceptional properties of respectively low-noise and high thermal conductivity, together with the high carrier drift velocity and mobility, are best exploited. The potential applications of graphene extend far beyond electronic devices. It is being touted as a material that will literally change our lives in the 21st century, like plastics did hundred years ago. Not only is graphene the thinnest (and lightest) possible material that is feasible, but it's also ~200 times stronger than steel and conducts both heat and electricity better than any material known to man – at room temperature. Potential applications for the material include replacing carbon fibers in composite materials, to eventually aiding the production of lighter aircrafts and satellites or stronger wind turbines; embedding the material in plastics to enable them to conduct electricity or just to make them stiffer, stronger, lighter or leak-tight; increasing the efficiency of electric batteries or supercapacitors by use of graphene powder; graphene based optoelectronic components promise closing the "terahertz gap" [28]; transparent conductive coatings for solar cells and (touch-enabled) displays; stronger medical implants; better sports equipment; artificial membranes for separating liquids; or nanogaps in graphene sheets may potentially provide a new technique for rapid DNA sequencing. Since graphene is so light, it holds a high potential in nanoelectromechanical (NEMs) systems and components and can usher in vast improvements in the speed of, for example, NEMs RF resonators to GHz frequencies. Graphene can be a part of future meta-materials built from stacks of other 2D materials such as BN or MoS_2 [29,30].

These 2D materials have the inherent advantage of single layer nature with atomic smoothness, no dangling bonds or surface defects, high transparency and the possibility of easily controllable layer-by-layer growth. Such a device – including back insulation, channel, and gate oxide and interconnects – is not thicker than about 5 nm. Besides, there are no clear obstacles for the sub-10 nm lateral scaling either.

The future of graphene holds limitless possibilities into literally every corner of industry and manufacturing, and in the coming years it will likely become a commonplace substance, the way plastics are today.

While graphene has been known as a textbook structure to calculate band diagrams and predict unique electronic properties since the early 1940s, the experimental investigation of graphene properties, as a standalone object, has been almost inexistent until the very recent years because of the difficulty to identify and univocally characterize the single-atom thick sheet. Therefore, **Fig.2** presents graphene identification data from (a) optical, (b) scanning probe and (c) electron microscopy as well as (d) ARPES, (e) Raman and (f) Rayleigh spectroscopy techniques.
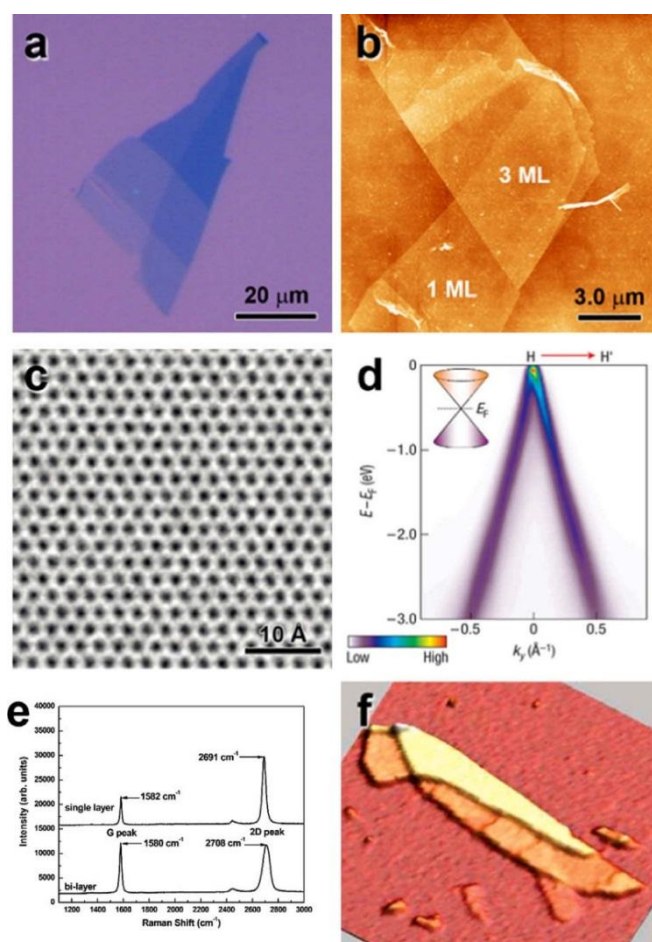

Figure 2. Major techniques for graphene characterization. (a) optical microscopy, (b) atomic force microscopy (AFM), (c) transmission electron microscopy (TEM),[31], (d) angle-resolved photoemission spectroscopy (ARPES), [32] (e) Raman scattering [33] and (f) Rayleigh scattering[34].

1.2. Outlines of the thesis

This work is dedicated to investigate the unique and excellent electrical and optical properties of graphene, through the fabrication and experimental study of several graphene based devices. Particular attention is paid to the details of all stages of the fabrication process which might have an effect on the properties of the final product. It also describes the characterization of graphene transistor structures, as well as experimental studies of charge transport.

I focused part of my research on optoelectronics and plasmonics of nanomaterials, in particular, I carried on a research that matched graphene and Plasmonics, the goal was to assess how the plasmonic response of metallic nanoparticles is modified by the presence of a graphene substrate, with results that could be very attractive as a starting point for the future optoelectronics applications.

This is how the thesis is planned: in the Chapter 2 I present a brief theoretical overview on the structural, electronic and optical properties of graphene.

In Chapter 3, I present the methods used for sample preparation, investigation of graphene flakes and the measurement setup. In particular, the identification of graphene is a very delicate step and involves the use of multiple techniques that complement each other. It is extremely difficult to find small graphene crystallites in the "haystack" of millions of thicker graphitic flakes. Thus, the identification is made by combining two or more of the following techniques: optical microscopy, Raman spectroscopy, SEM and the calculation of the contrast to give raise the best visibility.

The next, Chapter 4, is dedicated to the study of graphene based devices and their related features.

First, I fabricated 2D graphene FETs (GFETs) and explored several device designs to analyze transfer characteristic, mobility, and the influence of the contacts on the overall conductance.

The contacts between graphene and metal electrodes can significantly affect the electronic transport and limit or impede the full exploitation of the graphene intrinsic

properties. In this context I investigated the contact resistance on mono- and bi-layer graphene sheets by fabricating structures suitable for transfer length method measurements with Ni and Ti metals [36]. We also observed anomalies in GFET transfer characteristics, namely double dips, and here I present a work in which the origin of double dips in the transfer characteristics of GFET devices is explained [38].

In Chapter 5, I performed the characterization of Field Emission properties of several mono and bi layer graphene samples. I report the observation and characterization of field emission current from individual single- and few-layer graphene flakes laid on a flat SiO2/Si substrate. Measurements were performed in a scanning electron microscope chamber equipped with nanoprobes which allowed local measurement of the field emission current finding that the emission process is stable over a period of several hours and that it is well described by a Fowler–Nordheim model for currents over five orders of magnitude [37].

In the last Chapter 6, I present an exploration of the potential that electromagnetic surface waves known as surface plasmons may have in building both photonic elements and a new photonics technology based on nanostructured metals. I report results from an investigation into the plasmonic properties of metallic nanoparticles supported by substrates made of graphene, in order to extract information of its optical properties.

In summary: the main accomplishments of this work are to:

a) The Set-up of a routine procedure to identify graphene samples and make their morphological characterization.
b) The fabrication of graphene based electronic devices, like graphene field effect transistors and non-volatile memories.
c) The Study of the influence of different metal contact on the overall conductance, and the investigation of anomalies in GFET.
d) The investigation of quantum tunneling phenomenon in graphene.
e) The investigation of graphene as a substrate for plasmonics particles.

These results will be presented in due course.

Chapter 2
Properties of graphene

2.1. The graphene structure

Graphene is composed of sp^2-bonded carbon atoms arranged in a two-dimensional honeycomb lattice as shown in **Fig. 3**.
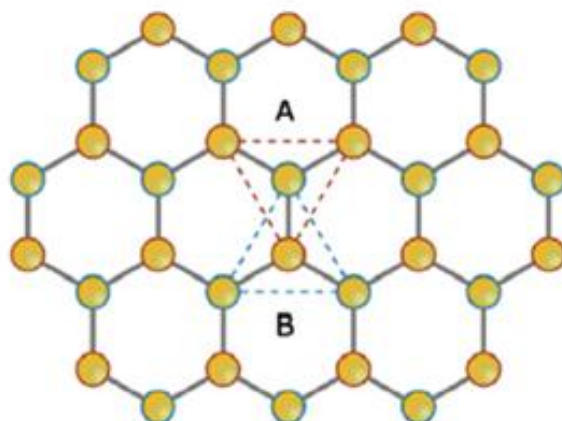

Figure 3. Atomic and electronic structures of graphene. (a) Graphene lattice consists of two interpenetrating triangular sublattices, each with different colors. The atoms at the sites of one sub-lattice, (i.e. A) are at the centers of the triangles defined by the other lattice (i.e. B), with a carbon-to-carbon inter-atomic length of 1.42A°.

It has been studied theoretically for a long time as building block of graphitic materials in other dimensions [39]. The most famous allotrope of graphene is graphite, consisting of stacked graphene layers, held together only by weak Van der Waals forces.

The lattice can be seen as consisting of two interpenetrated triangular sub-lattices, for which the atoms of one sub-lattice are at the center of the triangles defined by the other with a carbon-to-carbon inter-atomic length, a C–C, of 1.42A. The unit cell comprises two carbon atoms and is invariant under a rotation of 120° around any atom.

Each atom has one, s orbital, and two in-plane p orbitals contributing to the mechanical stability of the carbon sheet. The remaining p orbital, perpendicularly oriented to the molecular plane, hybridizes to form the π* (conduction) and π (valence) bands, which dominate the planar conduction phenomena [40].

2.2. Structural properties of Graphene

The structure can be seen as a triangular lattice with unit vectors $\mathbf{a_1}$ and $\mathbf{a_2}$, which enclose an angle of 60°, spanning the unit cell as shown in **Fig.4**.

The unit cell has a diatomic basis comprising two equivalent carbon atoms A and B .

The lattice vectors can be written as:

$$\mathbf{a_1} = \frac{a}{2}\left(3, \sqrt{3}\right) \quad , \quad \mathbf{a_2} = \frac{a}{2}\left(3, -\sqrt{3}\right) \tag{2.1}$$
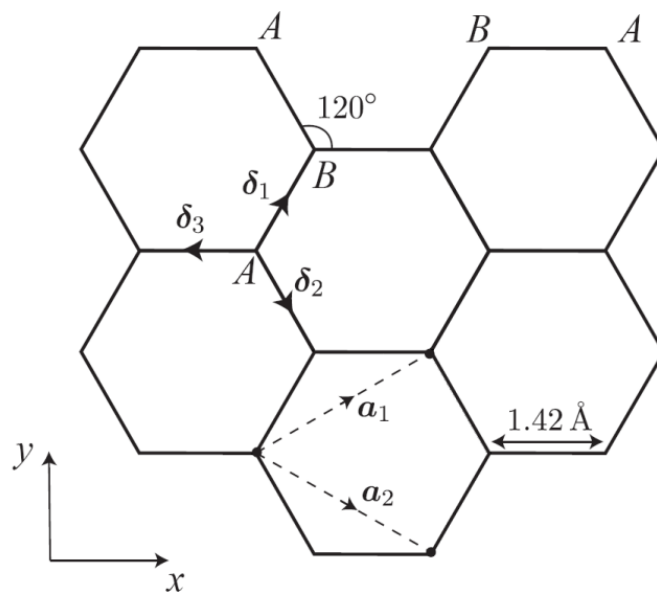

Figure 4. Hexagonal honeycomb lattice of graphene The primitive lattice vectors $a_{1,2}$ are defining the unit cell. There are two carbon atoms per unit-cell, denoted by A and B. Also shown are the vectors to the first nearest neighbors of an A atom $\delta_{1,2,3}$

Where **a ≈ 1.42 Å** is the nearest-neighbor C-C spacing, which is shorter than that in cubic diamond and the value of lattice constants is **a₁=a₂=2.46Å**.

When extending the graphene layer , we consider the other three next nearest neighbor vectors in real space, given by:

$$\boldsymbol{\delta_1} = \frac{a}{2}\left(1, \sqrt{3}\right), \quad \boldsymbol{\delta_2} = \frac{a}{2}\left(1, -\sqrt{3}\right), \quad \boldsymbol{\delta_3} = -a(1,0) \qquad (2.2)$$

Starting from the unit vectors **a₁** and **a₂** the reciprocal lattice vectors **b₁** and **b₂** are defined by the condition **ai · bj = 2π δij**. From that the first Brillouin zone of graphene is readily constructed (see **Fig. 6**).

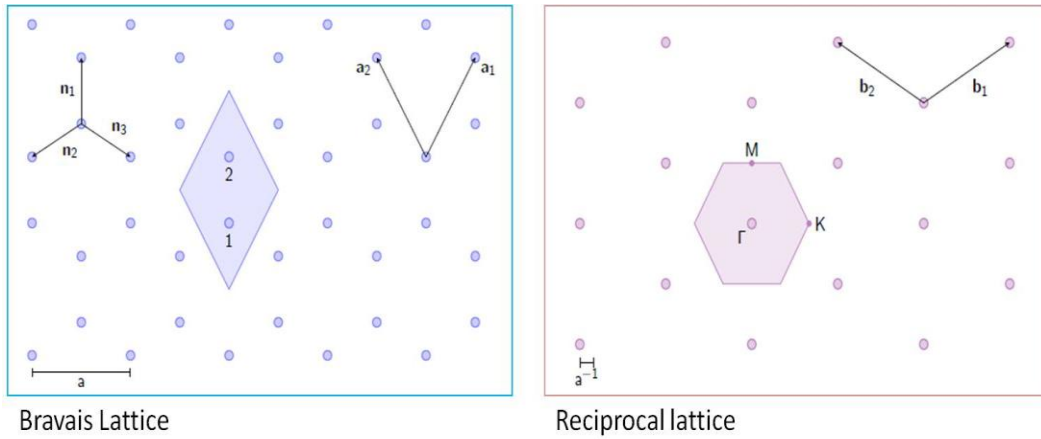Bravais Lattice   Reciprocal lattice

Figure 5.

$$b_1 = \frac{4\pi}{2a}\left(1, \sqrt{3}\right), \quad b_2 = \frac{4\pi}{2a}\left(1, -\sqrt{3}\right) \qquad (2.3)$$

In reciprocal space, the first Brillouin zone also has hexagonal shape (**Fig. 5, 6**). Among the high-symmetry points, the points K and K' at the corner of the Brillouin zone will be of special interest for the band structure.
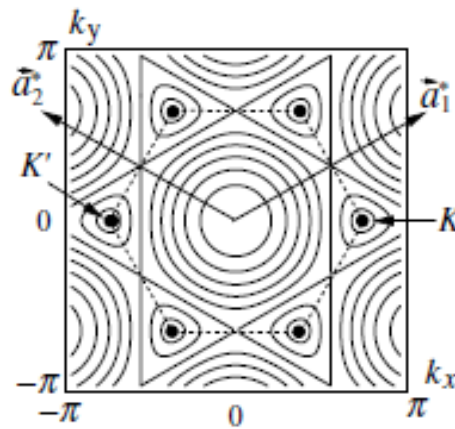
Figure 6. The equal energy contours are drawn, and the Brillouin zone (BZ) is indicated by dashed lines. The Dirac points *K* and *K'* are marked by arrows, and the reciprocal lattice vectors $\vec{a}^{\,*}_{1,2}$ are also drawn. It is clear that the six points at the corners of the first Brillouin zone fall into two groups of three which are equivalent, so we need to consider only two equivalent corners that we denote as K and K'.

There are two types of graphene structure namely the zigzag and the armchair type. These structures differ according to the orientation and the direction of the edges. By looking at the figure and considering the edge along the y-axis, we see an armchair structure. Using the edge along the x-axis, it is possible to recognize the zigzag shape, **fig.7**.
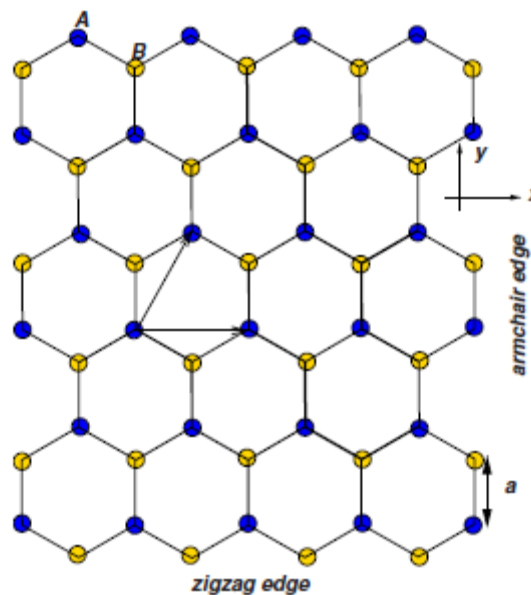

Figure 7: Graphene structure

2.3. Electronic band structure of the graphene lattice

After defining the lattice structure, the next step is to determine the band diagrams.

One of the reasons justifying the interest in graphene lies in its energy band spectrum and in its electronic properties which are very special and different from standard semiconductors. Basically, according to their the electronic properties, materials are classified as metal, semi-metals, semiconductors or insulators. This classification is derived from the densities of states and band structures of the material.

In condensed matter physics, the Schrödinger equation rules the world, usually being quite sufficient to describe electronic properties of materials.

Charge carriers in semiconductors have a non-zero effective mass, and their behavior can be well described by the Schrodinger equation.

Graphene is an exception: its charge carriers mimic relativistic particles and are easier and more natural to describe starting with the Dirac equation rather than the Schrödinger equation [41-49].
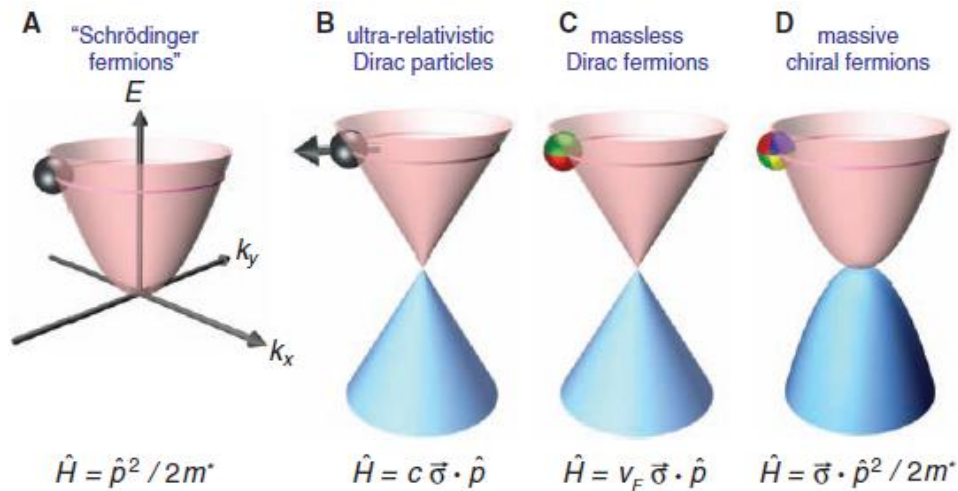

Figure 8. (A) Charge carriers in condensed matter physics are normally described by the Schrödinger equation with an effective mass m* different from the free electron mass (p is the momentum operator). (B) Relativistic particles in the limit of zero rest mass follow the Dirac equation, where c is the speed of light and σ is the Pauli matrix. (C) Charge carriers in graphene are called massless Dirac fermions and are described by a 2D analog of the Dirac equation, with the Fermi velocity $v_F \approx 1 \times 10^6$ m/s playing the role of the speed of light .(D) Bilayer graphene provides us with yet another type of quasi-particles that have no analogies. They are massive Dirac fermions described by a rather bizarre Hamiltonian that combines features of both Dirac and Schrödinger equations. The pseudospin changes its color index four times as it moves among four carbon sublattices (2–4).

Although there is nothing particularly relativistic about electrons moving around carbon atoms, their interaction with a periodic potential of graphene's honeycomb lattice gives rise to new quasiparticles that at low energies E are accurately described by the (2+1)-dimensional Dirac equation with an effective speed of light $\mathbf{v_F \approx 10^6 m/s}$. These quasiparticles, called massless Dirac fermions, can be seen as electrons that lost their rest mass $\mathbf{m_0}$ or as neutrinos that acquired the electron charge $\mathbf{e}$. The relativistic-like description of electron waves on honeycomb lattices has been known theoretically for many years, never failing to attract attention, and the experimental discovery of graphene now provides a way to probe quantum electrodynamics (QED) phenomena by measuring graphene's electronic properties.

In the high-energy limit, the linear energy–momentum relation is no longer valid and the bands are subjected to a distortion leading to anisotropy, also known as trigonal warping [6]. Upon stacking layers on top of each other, one first obtains bilayered graphene, which exhibits its own set of very specific properties. The center of the aromatic rings of the upper graphene sheet sits on top of an atom of the lower sheet, so that the symmetry is trigonal rather than hexagonal. With the inter-plane interaction, the charge carriers acquire a mass and the dispersion recovers a parabolic dispersion described by the Schrodinger formalism. Nevertheless, bilayer graphene remains gapless if one ignores trigonal warping.

The lateral confinement of the 2D lattice into nearly 1D ribbons causes band gap opening, which opens the possibilities to exploit the electronic properties of graphene in semiconductor device applications.

We use a "tight binding" (TB) or linear combination of atomic orbitals (LCAO) method for calculating the energy band structure, which stands as the basis of all electronic (and optical) properties of graphene. A common approximation is to neglect the on-site overlap (p_z ground state energy) and the overlap between wave functions centered at different atoms (i.e. the σ skeleton). The electrons populating the p_z orbitals in the periodic lattice of carbon atoms can be described with the following wave function:

$$\Psi_k(r) = \sum_j C_{kj}\,\Phi(r - r_j) \tag{2.4}$$

in which $\mathbf{\Phi(r)}$ is the wave function for free electron moving in the electric field of isolated atom and $\mathbf{C_{kj}}$ are the Fourier coefficients. To construct periodic Bloch functions, let , $\mathbf{C_{kj}} = \mathbf{N^{-1/2}e^{ik.Rj}}$ where $\mathbf{N}$ is the number of atoms in the system. Thus,

$$\Psi_k(r) = \frac{1}{\sqrt{N}}\sum_m e^{ikr_j}\,\Phi(r - r_j) \tag{2.5}$$

The band structure is calculated by evaluating the eigenvalues of the Hamiltonian matrix for the $\mathbf{k}$ values. The Hamiltonian of the system is in the form:

$$\widehat{H}(\boldsymbol{k})\Psi_k(r) = \varepsilon(k)\Psi_k(r) \tag{2.6}$$

where is $\widehat{H}(\boldsymbol{k})$

$$\widehat{H}(k) = \begin{pmatrix} H_{11}(k) & H_{12}(k) \\ H_{21}(k) & H_{22}(k) \end{pmatrix} \tag{2.7}$$

The diagonal matrix elements represent the $\boldsymbol{p_z}$ orbital ground state energy and can be chosen as the reference point of the energy i.e. to zero.
The off-diagonals are given by:

$$\langle \boldsymbol{k}|\boldsymbol{H}|\boldsymbol{k}\rangle = \frac{1}{N}\sum_{j,m} e^{ik(r_j - r_m)}\langle \Phi_m|H|\Phi_j\rangle \tag{2.8}$$

where $\mathbf{\Phi_m = \Phi(r\text{-}r_m)}$ Using $\varrho_m \mathbf{=r_m\text{-}r_j}$ to connect the matrix element

$$\langle \boldsymbol{k}|\boldsymbol{H}|\boldsymbol{k}\rangle = \sum_m e^{-ik\rho_m}\int dV\,\Phi^*(r - \rho_m)\boldsymbol{H}\,\Phi(r) = \gamma_0\sum_m e^{-ik\rho_m} \tag{2.9}$$

14

and

$$\gamma_0 = \int dV \, \Phi^*(r - \rho_m) \boldsymbol{H} \, \Phi(r) \tag{2.10}$$

is the hopping parameter for the nearest neighbor. Its value for graphene is $\boldsymbol{\gamma_0}$ **~2.8 eV**. Plugging the coordinates of the nearest neighbors into the expression yields:

$$H_{12}(k) = \gamma_0 \left(e^{-ik_x a} + e^{-ik_x \frac{a}{2} + ik_y \frac{\sqrt{3}a}{2}} + e^{-ik_x \frac{a}{2} - ik_y \frac{\sqrt{3}a}{2}} \right) \tag{2.11}$$

or

$$H_{12}(k) = \gamma_0 e^{-ik_x a} \left(1 + 2e^{-ik_x \frac{a}{2}} \cos \frac{\sqrt{3}}{2} k_y a \right) \tag{2.12}$$

The eigenenergy of *H(k)* is specified by the secular equation:

$$\left| \hat{H}(\boldsymbol{k}) - \varepsilon(k) \right| = \begin{vmatrix} -\varepsilon(k) & H_{12}(k) \\ H^*_{12}(k) & -\varepsilon(k) \end{vmatrix} = 0 \tag{2.13}$$

We get the energy dispersion (or band structure) of 2D graphene to be:

$$\varepsilon(k) = \pm |H_{12}(k)| = \pm \gamma_0 \sqrt{1 + 4\cos^2 k_y \frac{a}{2} + 4\cos k_y \frac{a}{2} \cos k_x \frac{\sqrt{3}a}{2}} \tag{2.14}$$

This relation (plotted in **Fig. 9**) looks linear for low energies near the six corners (*K* or Dirac-points) of the two-dimensional hexagonal Brillouin zone. Let's call **k = K + dk** and examine this linearity by expanding the expression for **H₁₂(k)**, eq.2.12, around K (0,4π/3):

$$H_{12}(k) = \gamma_0 \left[(1 + ik_x a) + \left(1 - \frac{ik_x a}{2} \right) 2 \left(-\frac{1}{2} - sin \frac{2\pi}{3} \frac{\sqrt{3}k_y a}{2} \right) \right] \qquad (2.15)$$

$$= \gamma_0 \left[\frac{3}{2} ik_x a - \frac{3k_y a}{2} \right] = \frac{3\gamma_0 a}{2} (ik_x - k_y) \qquad (2.16)$$

The Fermi velocity υ_F, is defined as

$$v_F = \frac{3\gamma_0 a}{2\hbar} \cong 0.9 \frac{10^6 m}{s} \qquad (2.17)$$

If we had expanded around K' we would have obtained the complex conjugate of Eq.2.15. To determine the energy relation near the K point we can write the Hamiltonian in the form:

$$\widehat{H} = \hbar v_F \begin{pmatrix} 0 & k_x + ik_x \\ k_x - ik_x & 0 \end{pmatrix} = \hbar v_F \hat{\sigma}.p \qquad (2.18)$$

and the **E-k** relationship comes out in the form

$$\varepsilon(k) = \pm \hbar v_F |k| = \pm \hbar v_F \sqrt{k^2{}_x + k^2{}_y} \qquad (2.19)$$

Due to this linear dispersion relation at low energies, electrons and holes near these six points behave like relativistic particles described by the Dirac equation for spin 1/2 particles. That is why the electrons and holes are called Dirac fermions, and the six corners of the Brillouin zone are called the Dirac points.

The linear energy dispersion relation makes graphene quite different from most conventional three-dimensional semiconductors, which exhibit parabolic bands (energy is proportional to the square of the momentum) and a band gap. Intrinsic graphene can be thought of as a semi-metal, or a zero-gap semiconductor, as shown in **Fig. 8**.
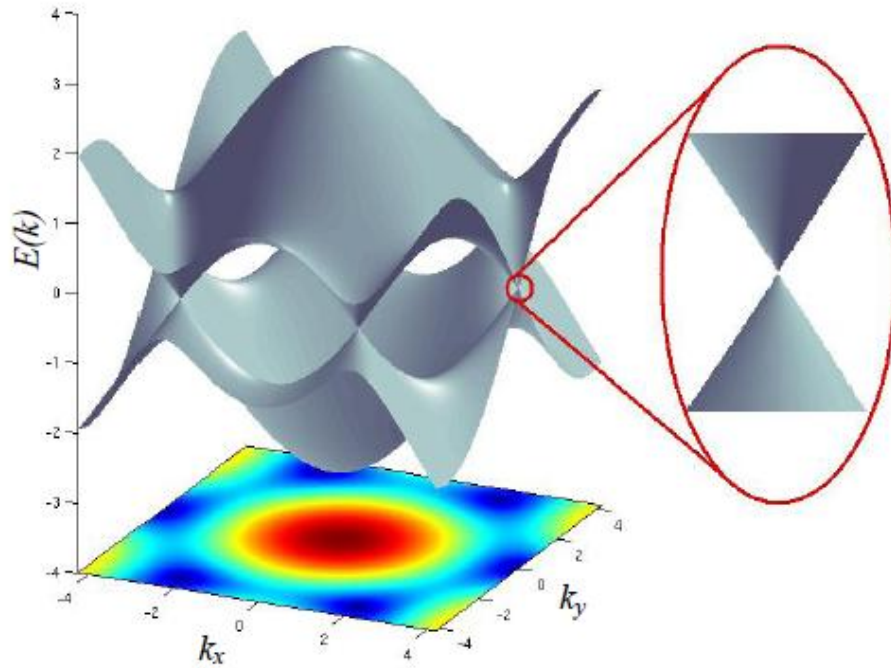
Figure 9. Energy bands of graphene. (left) Energy spectrum in units of γ_0 = 2.8 eV (nearest neighbor hopping energy) as a function of momentum k_i. (right) Zoomed portion of the linear energy band near the Dirac point. The maximum energy at k = 0 can be estimated from Eq.2.14

2.4. Carrier statistics and mobility in graphene (Inserire immagine)

Graphene's quality clearly reveals itself in a pronounced ambipolar electric field effect (**Fig.10**) such that charge carriers can be tuned continuously between electrons and holes in concentrations **n** as high as 1.10^{13} cm^{-2} carrier concentration [50] and remarkably high electron mobility at room temperature with reported values in excess of **µ** ~ 15 000 cm²/Vs.

Moreover, the observed mobility weakly depend on temperature *T*, which means that µ at 300K is still limited by impurity scattering and, therefore, can be improved significantly, perhaps, even up to ≈ 100,000 cm²/Vs.

Although some semiconductors exhibit room-temperature μ as high as ≈ 77,000 cm^2/Vs (namely, InSb), those values are quoted for undoped bulk semiconductors. In graphene, μ remains high even at high n (>10^{12}cm^{-2}) in both electrically and chemically- doped devices [51] , which translates into ballistic transport on submicron scale (up to ≈0.3 μm at 300K).
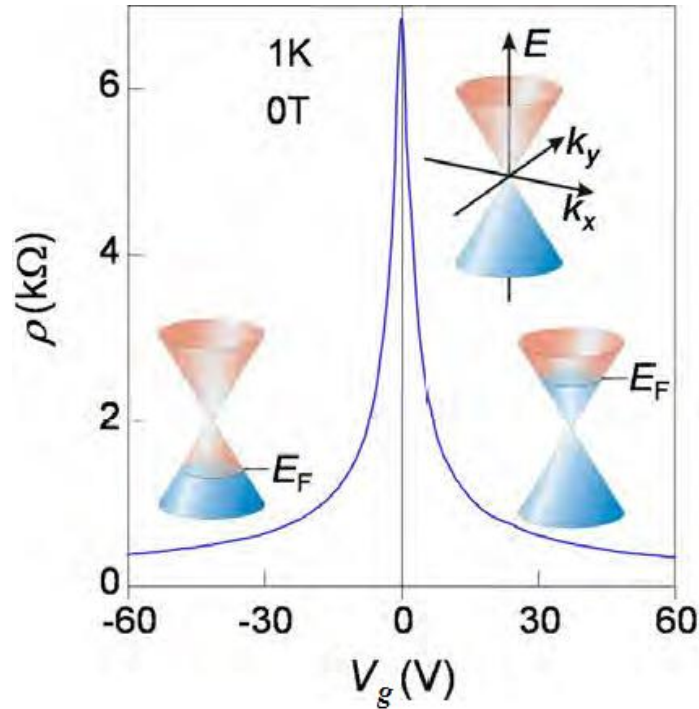

Figure 10. Ballistic electron transport in graphene. Ambipolar electric field effect in single-layer graphene. The insets show its conical low-energy spectrum $E(k)$, indicating changes in the position of the Fermi energy E_F with changing gate voltage Vg. Positive (negative) Vg induce electrons (holes) in concentrations $n = \alpha Vg$ where the coefficient α ≈7.2·10^{10}cm^{-2}/V for field-effect devices with a 300 nm SiO$_2$ layer used as a dielectric [52-54]. The rapid decrease in resistivity ϱ with adding charge carriers indicates their high mobility (in this case, μ ≈ 15,000cm^2/Vs and does not noticeably change with temperature up to 300K).

Scattering by acoustic phonons in graphene limits the low field room temperature μ to 200 000 cm^2/Vs at a carrier density of **n** ~ 2.10^{11} cm^{-2}, which was experimentally achieved in suspended graphene [25]. However, for graphene in contact with oxides or dielectrics, scattering of electrons by optical phonons of the substrate dominates at room temperature.

18

The intrinsic optical phonon energy in graphene is $\hbar\omega_{op} \approx 160$ meV, thus emission is not possible in the case of low energy transport. It has been shown that the surface optical (SO) phonon energy of common dielectrics is lower, in the $20 - 80$ meV range [55].

Impurity scattering can be an important factor too, depending on the impurity concentration of the substrates. High-$\varkappa$ dielectrics have lower energy SO modes thus the mobility has a lower limit. On the other hand the higher dielectric constant screens the impurity charges more effectively. The two competing effects renders the maximum achievable mobility to $\sim$10 000 cm^2/Vs at room temperature and is more or less independent of the choice of the dielectric at $n_{imp} \sim 5.10^{11}$ cm^{-2} impurity concentration and at $n \sim 10^{12}$ cm^{-2} charge density [55].

The relation between the scattering rate $1/\tau$ and mobility in semiconductors is $\mu = \tau q/m^*$, where **q** is the electron charge and **m*** is the effective mass.

For graphene it is [56]:

$$\mu = \frac{qv_F}{\hbar\sqrt{\pi n}}\tau \tag{2.20}$$

where v_F is the Fermi velocity and **n** is the carrier concentration.

Equation 2.20, turns the attention towards an interesting fact, namely that the mobility is highly dependent on the carrier concentration in graphene, which is examined in detail in the following.

Using the energy dispersion relation of graphene, which is conical at low energies (Eq. 2.19) to determine the 2D density of states ($\varrho(E)=kdk/\pi$, DOS), it can be written:

$$\rho(E) = \frac{g_v g_s}{2\pi(\hbar v_F)^2} |E| \tag{2.21}$$

where $g_v=2$ is the valley degeneracy and $g_s=2$ is the spin degeneracy. Only some of these states are populated by carriers and it is defined by the Fermi-Dirac distribution at a given Fermi level E_F:

$$f(E) = \frac{1}{1 + e^{(E-E_F)/kT}} \tag{2.22}$$

To find the electron density, the product of the Fermi-Dirac distribution and the DOS has to be integrated over the whole energy range:

$$n = \int_0^\infty \rho(E)f(E)dE \tag{2.23}$$

The integral can be evaluated [31] if we introduce $u = E/kT$ and $\eta = E_F/kT$:

$$n \text{ or } p = \frac{2}{\pi}\left(\frac{kT}{\hbar v_F}\right)^2 \Im_1(\pm\eta) \tag{2.24}$$

Where

$$\Im_1(\pm\eta) = \frac{1}{\Gamma(j+1)\int_0^\infty duu^j/(1 + e^{u-\eta})} \tag{2.25}$$

is the Fermi-Dirac integral with $j = 1$, $\Gamma(...)$ is the gamma function and the sign on η is + for electrons and – for holes. In the special case when the Fermi level is at 0eV Eq. (2.24) simplifies to:

$$n_i = \frac{\pi}{6}\left(\frac{kT}{\hbar v_F}\right)^2 \tag{2.26}$$

Where n_i is called the intrinsic carrier concentration. Unlike in case of materials with bandgaps, the intrinsic carrier concentration in graphene does not depend exponentially on temperature, but quadratically.

This is a very interesting and unique phenomena but it has not yet been observed because it requires samples with very low residual impurity concentration. A way to get rid of the effect of impurities is to suspend graphene.

It is well known that mobility is a function of carrier concentration in graphene and very high mobility values can be obtained only at very low carrier concentrations.

Starting from the equation for the drift current of a graphene FET:

$$\boldsymbol{J} = en\mu\boldsymbol{E} \tag{2.27}$$

where $\boldsymbol{n}$ is the 2D carrier concentration, and $\boldsymbol{E}$ is the electric field along the channel. The conductivity is $\boldsymbol{\sigma = J/E}$, and one can extract the mobility specifically for a 2D graphene field effect transistor geometry:

$$\mu_{CON} = \frac{\sigma}{en} = \frac{I_D}{V_{DS}}\frac{L_G}{W}\frac{1}{en} = \frac{I_D}{V_{DS}}\frac{L_G}{W}\frac{1}{C_{OX}(V_{GS} - V_0)} \tag{2.28}$$

where **e** is the electron charge, **n** is the 2D carrier concentration, $\mathbf{L_G}$ is the gate length, **W** is the channel width, $\mathbf{V_{DS}}$ is the source-drain bias, $\mathbf{V_{GS}}$ is the gate bias and $\mathbf{V_0}$ is the threshold-or Dirac-point voltage. This definition of the mobility is inversely proportional to carrier concentration therefore it gives extremely high mobility values for low carrier concentrations. This can be called conductance based mobility ($\boldsymbol{\mu_{CON}}$). We can also define a field-effect mobility ($\boldsymbol{\mu_{FE}}$) as the change in the sheet conductivity of graphene due to carrier density modulation **Δn** as:

$$\Delta\sigma = \Delta ne\mu \tag{2.29}$$

The expression can be modified to the form:

$$\mu_{FE} = \frac{\Delta\sigma}{\Delta n}e = \frac{L_G}{W}\frac{g_m}{C_{OX}V_{GS}} \qquad (2.30)$$

Where $g_m=dI_D/dV_{GS}$ is the transconductance. As opposed to μ_{CON} the field-effect mobility μ_{FE} goes to zero at the lowest carrier concentrations at the Dirac point, since the drain current reaches a minimum when the gate bias equals the Dirac point, and by definition $g_m=dI_D/dV_{GS}=0$.

2.5. Some interesting properties

2.5.1.1. Stability in two dimensions

The fact that two-dimensional atomic crystals do exist, and moreover, are stable under ambient conditions [148] is amazing.

More than 70 years ago, Landau and Peierls argued that strictly two-dimensional (2D) crystals were thermodynamically unstable and could not exist.

A standard description [149] of atomic motion in solids assumes that amplitudes of atomic vibration *u* near their equilibrium position are much smaller than interatomic distances *d*, otherwise the crystal would melt according to an empirical Lindemann criterion (at the melting point, $u \approx 0.1d$).

For instance, the melting temperature of thin films rapidly decreases with decreasing thickness, and they become unstable (segregate into islands or decompose) at a thickness of, typically, dozens of atomic layers. For this reason, atomic monolayers have so far been known only as an integral part of larger 3D structures.

The argument was later extended by Mermin [147] and is strongly supported by a whole omnibus of experimental observations.

As a result of this small amplitude, the thermodynamics of solids can be successfully described using a picture of an ideal gas of phonons, i.e. quanta of atomic displacement waves (harmonic approximation).

In three-dimensional systems, this view is self-consistent in a sense that fluctuations of atomic positions calculated in the harmonic approximation do indeed turn out to be small, at least at low enough temperatures.

In contrast, in a two-dimensional crystal, the number of long-wavelength phonons diverges at low temperatures and, thus, the amplitudes of interatomic displacements calculated in the harmonic approximation diverge [150-151].

According to similar arguments, a flexible membrane embedded in three-dimensional space should be crumpled because of dangerous long-wavelength bending fluctuations [152]. However, in the past 20 years, theoreticians have demonstrated that these dangerous fluctuations can be suppressed by inharmonic (nonlinear) coupling between bending and stretching modes [152-154]. As a result, single-crystalline membranes can exist but should be 'rippled'. This gives rise to 'roughness fluctuations' with a typical height that scales with sample size L as $L\zeta$, with $\zeta \approx 0.6$. Indeed, ripples, **fig. 11**, are observed in graphene, and play an important role in its electronic properties [154].
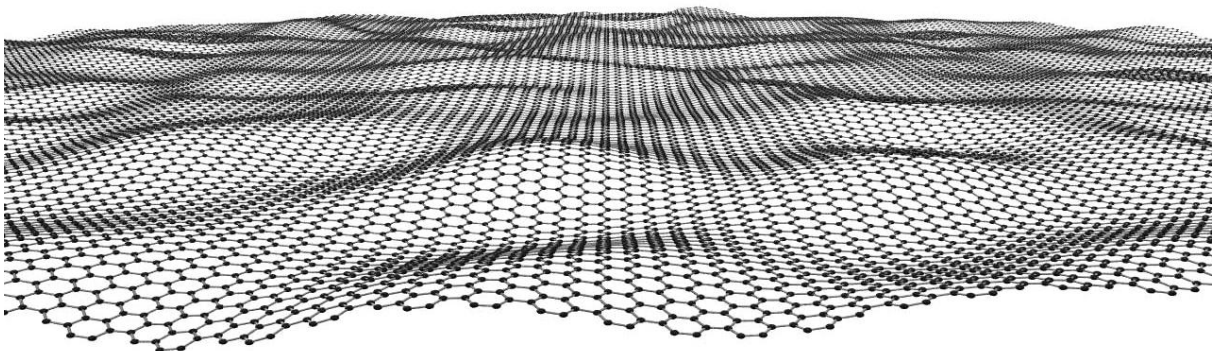

Figure 11: Illustration of a single-layer graphene sheet with out-of-plane corrugations. The thermodynamic stability of the 2D crystal is believed to be accounted for mainly by such ripples [7]. (Image source: J. Meyer [7])

2.5.1.2. Anomalous Integer Quantum Hall Effect

Classically, an electrical conductor carrying a current I in a perpendicular magnetic field $\mathbf{B_\perp}$ will show a potential difference $\mathbf{U_{xy}} = \mathbf{U_H}$ across the opposite sides of the conductor. The hall resistance $\mathbf{R_H} = \mathbf{U_H/I} = -\mathbf{B_\perp/(n \cdot e \cdot t)}$ is the ratio of the potential drop divided by the current, where $\mathbf{n}$ is the charge carrier density, $\mathbf{e}$ is the electron charge, and $\mathbf{t}$ is the thickness of the conductor. The Hall Effect is a consequence of the Lorentz force acting on the charge carriers: the transverse magnetic field deflects the carriers, causing them to accumulate at one side of the conductor.

In two dimensional electron gases (2DEGs) at low temperatures and high magnetic fields, it was found [57] that the Hall conductivity $\mathbf{\sigma_H} = \mathbf{\varrho_H}^{-1}$ takes on discrete values of

$$\sigma_H = N \ \frac{\nu e^2}{h} \quad N = 0,1,2 \dots \tag{2.31}$$

Where $\mathbf{h}$ is the Planck constant, $\mathbf{e}$ is the electron charge and $\mathbf{\nu}$ is due to the spin and the valley degeneracy of the 2DEG. This is due to the fact that in a perpendicular magnetic field, the electrons in the 2DEG are forced to move in quantized cyclotron orbits with discrete energy levels. These energies, known as Landau levels (LLs), are given by:

$$E_N = (N + 1/2) \ \hbar \omega_C \tag{2.32}$$

Where $\mathbf{\omega_c} = \mathbf{eB/m^*}$ is the cyclotron frequency. The Hall conductivity σ_H remains constant when the Fermi energy E_F is between two LLs and increases by a discrete value, when E_F passes the next higher LL.
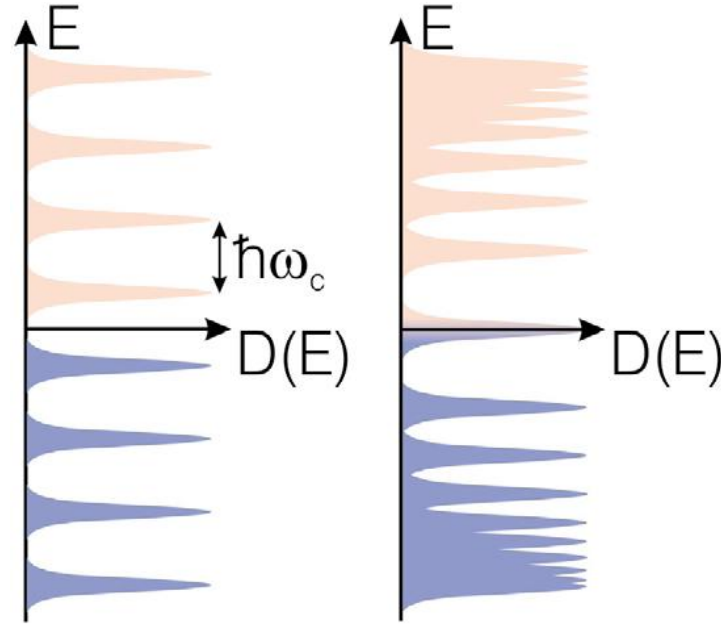
Figure 12. (Left) Landau levels for Schrödinger electrons with two parabolic bands touching each other at zero energy. (Right) Landau levels for Dirac electrons.

The QHE in single layer graphene (SLG) differs from that in conventional 2DEGs in the sense that the Hall conductivity plateaus are shifted [4] and form at

$$\sigma_H = \left(N + \frac{1}{2}\right)\frac{4e^2}{h} \quad N = 0,1,2 \dots \tag{2.33}$$

This so-called half-integer QHE of SLG was first measured by Novoselov *et al.* [54] (see **fig.13**) and Zhang *et al.* [58]. The reason for this shift of *2e²/h* is that in graphene, the LL energies are given by:

$$E_N = \pm v_F\sqrt{2e\hbar BN} \tag{2.24}$$

An important peculiarity of the Landau levels for massless Dirac fermions is the existence of zero-energy states (with $\nu = 0$ and a minus sign in the equation).
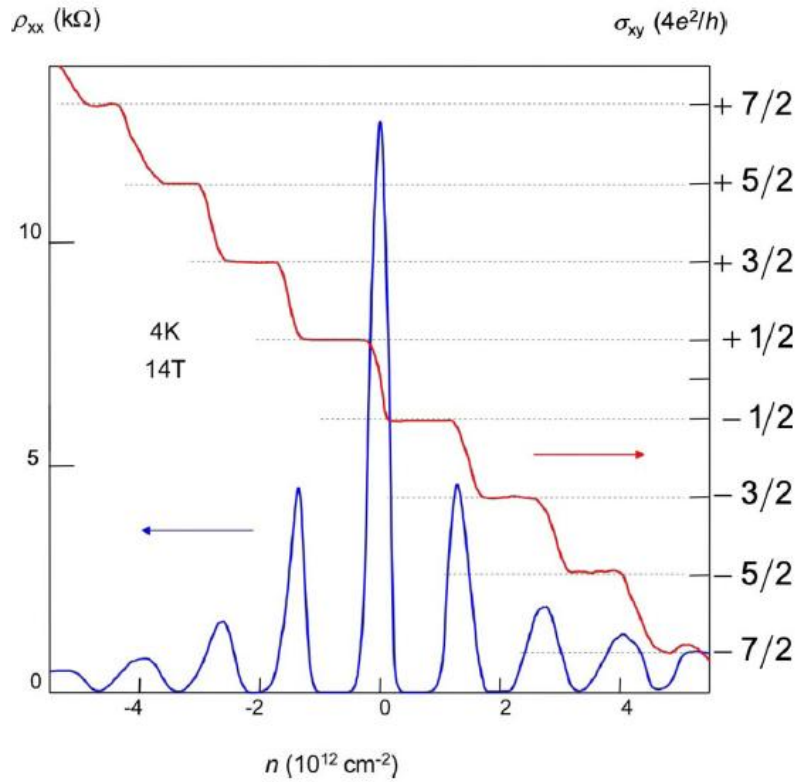
Figure 13: QHE measurements at 4 K/14 T of a single layer graphene device by Novoselov *et al.* [54].The Hall conductivity $\sigma_{xy} = \varrho^{-1}_{H}$ as a function of the carrier concentration *n* forms plateaus at half-integer values of **4e²/h** (red curve), while the longitudinal resistivity ϱ_{xx} vanishes at these values of **n** (blue curve).

This situation differs markedly from conventional semiconductors with parabolic bands where the first Landau level is shifted by ½ħω$_c$. As shown by the Manchester and Columbia groups [54,58] the existence of the zero-energy Landau level leads to an anomalous QHE with ***half-integer*** quantization of the Hall conductivity (**Fig.13**), instead of an ***integer*** one (for a review of the QHE, see, for example [59]). Usually, all Landau levels have the same degeneracy (number of electron states with a given energy), which is proportional to the magnetic flux through the system. As a result, the plateaus in the Hall conductivity corresponding to the filling of first ν levels are integers (in units of the conductance quantum e²/h). For the case of massless Dirac electrons, the zero-energy Landau level has half the degeneracy of any other level.

This anomalous QHE is the most direct evidence for Dirac fermions in graphene [15, 16].

2.5.1.3. Klein paradox

Quantum tunneling

Quantum tunneling is a consequence of very general laws of quantum mechanics, such as the Heisenberg uncertainty relations. A classical particle cannot propagate through a region where its potential energy is higher than its total energy . However, because of the uncertainty principle, it is impossible to know the exact values of a quantum particle's coordinates and velocity, and thus its kinetic and potential energy, at the same time instant. Therefore, penetration through the 'classically forbidden' region turns out to be possible. This phenomenon is widely used in modern electronics, beginning with the pioneering work of Esaki [60].

When a potential barrier is smaller than the gap separating electron and hole bands in semiconductors, the penetration probability decays exponentially with the barrier height and width. Otherwise, resonant tunneling is possible when the energy of the propagating electron coincides with one of the hole energy levels inside the barrier.

Surprisingly, in the case of graphene, the transmission probability for normally incident electrons is always equal to unity, irrespective of the height and width of the barrier [61-63].

In QED, this behavior is related to the Klein paradox [61,64-66]. This phenomenon usually refers to a counterintuitive relativistic process in which an incoming electron starts penetrating through a potential barrier, if the barrier height exceeds twice the electron's rest energy $\mathbf{mc^2}$. In this case, the transmission probability T depends only weakly on barrier height, approaching perfect transparency for very high barriers, in stark contrast to conventional, and non relativistic tunneling. This relativistic effect can be attributed to the fact that a sufficiently strong potential, being repulsive for electrons, is attractive to positrons, and results in positron states inside the barrier. These align in energy with the electron continuum outside the barrier. Matching between electron and positron wave functions across the barrier leads to the high probability tunneling described by the Klein paradox.

In other words, it reflects an essential difference between non relativistic and relativistic quantum mechanics. In the former case, we can measure accurately either the position of the electron or its velocity, but not both simultaneously. In relativistic quantum mechanics, we cannot measure even electron position with arbitrary accuracy since, if we try to do this, we create electron-positron pairs from the vacuum and we cannot distinguish our original electron from these newly created electrons.

We first note that the wave function for Dirac fermions in graphene can be given by:

$$\psi(k) = \frac{1}{\sqrt{2}} \begin{pmatrix} 1 \\ \pm e^{i\Phi(k)} \end{pmatrix} \tag{2.25}$$

where $\Phi(k) = \tan^{-1} k_y/k_x$. We now consider scattering by a finite potential well of magnitude V_0 and width D, as shown in **fig.14**. There are thus three regions as marked in the figure. In region I, we have:

$$\psi_I(r) = \frac{1}{\sqrt{2}} \begin{pmatrix} 1 \\ se^{i\Phi(k)} \end{pmatrix} e^{i(k_x x + k_y y)} + \frac{r}{\sqrt{2}} \begin{pmatrix} 1 \\ se^{i(\pi - \Phi(k))} \end{pmatrix} e^{i(-k_x x + k_y y)} \tag{2.26}$$

Which has a right and left moving component, where s $=\pm 1$, and in polar coordinates, and considering fermions with Fermi momentum k_F , we have $k_y = k_F \sin \Phi(k)$ and $k_x = k_F \cos \Phi(k)$. In region II:

$$\psi_{II}(r) = \frac{a}{\sqrt{2}} \begin{pmatrix} 1 \\ s'e^{i\theta} \end{pmatrix} e^{i(q_x x + k_y y)} + \frac{b}{\sqrt{2}} \begin{pmatrix} 1 \\ s'e^{i(\pi - \theta)} \end{pmatrix} e^{i(-q_x x + k_y y)} \tag{2.27}$$
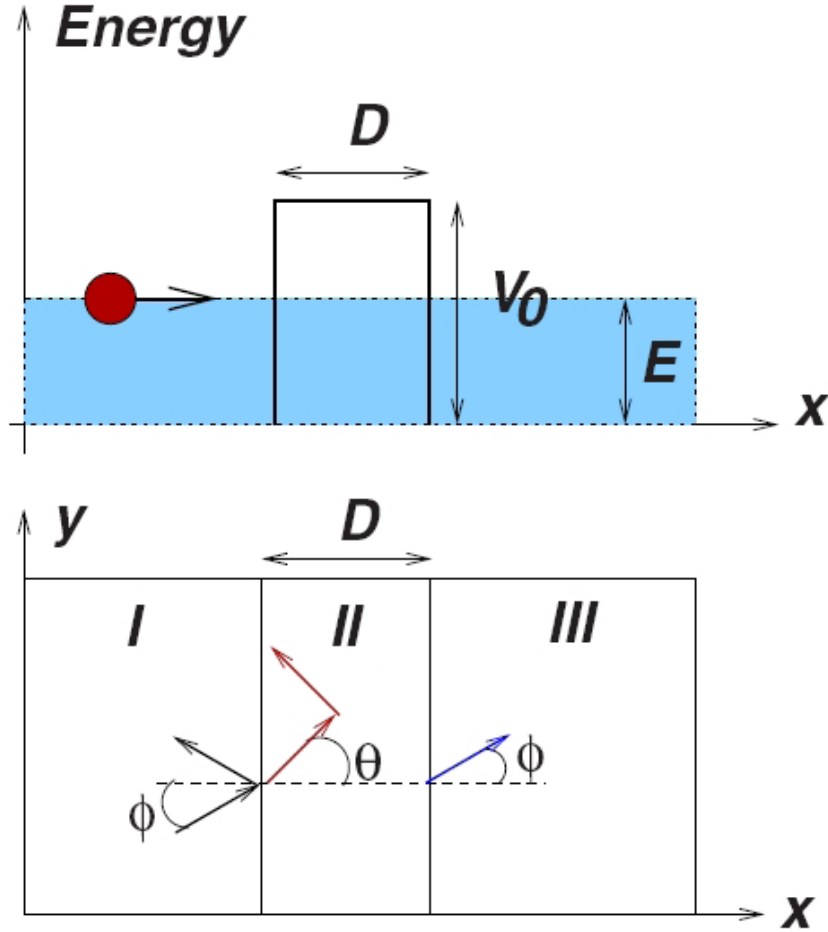
Figure 14: The proposed setup to demonstrate the Klein paradox. An incoming Dirac Fermion hits a finite potential well of magnitude V_0 and width D. The transmission is calculated as usual in elementary quantum mechanics by demanding the continuity of the wave functions. Figure from reference [67]

Where $\theta = \tan^{-1} k_y/q_x$ and $q_x = \sqrt{\frac{(V_0-E)^2}{(v_F)^2} - k_x^{\,2}}$ and for the region III we have only a right moving component:

$$\psi_{III}(r) = \frac{t}{\sqrt{2}}\begin{pmatrix} 1 \\ se^{i\Phi(k)} \end{pmatrix} e^{i(k_x x + k_y y)} \qquad (2.28)$$

Where **s** = sign(E) and **s'** = sign(E-V$_0$). According to the standard prescription, the coefficients of the wave functions must be determined such that continuity is preserved at the boundaries x = 0, D, but the derivative need not be matched in this case, unlike with the Schrodinger equation. The transmission as a function of incident angle is T(Φ) = tt*, and is given by:

$$T(\Phi) = \frac{cos^2\theta cos^2\Phi}{(cos(Dq_x)cos\Phi cos\theta)^2 + sin^2(Dq_x)(1 - ss'sin\Phi sin\theta)^2} \quad (2.29)$$

What is unusual about this result is that for Dq$_x$ = nπ, the barrier becomes completely transparent (T(Φ) = 1), which includes normal incidence (Φ→ 0).

This is the Klein paradox, and is unique for relativistic electrons. Some nice results are reported in **fig.16** , where, depending on the value of V$_0$, there are several points with complete transmission.
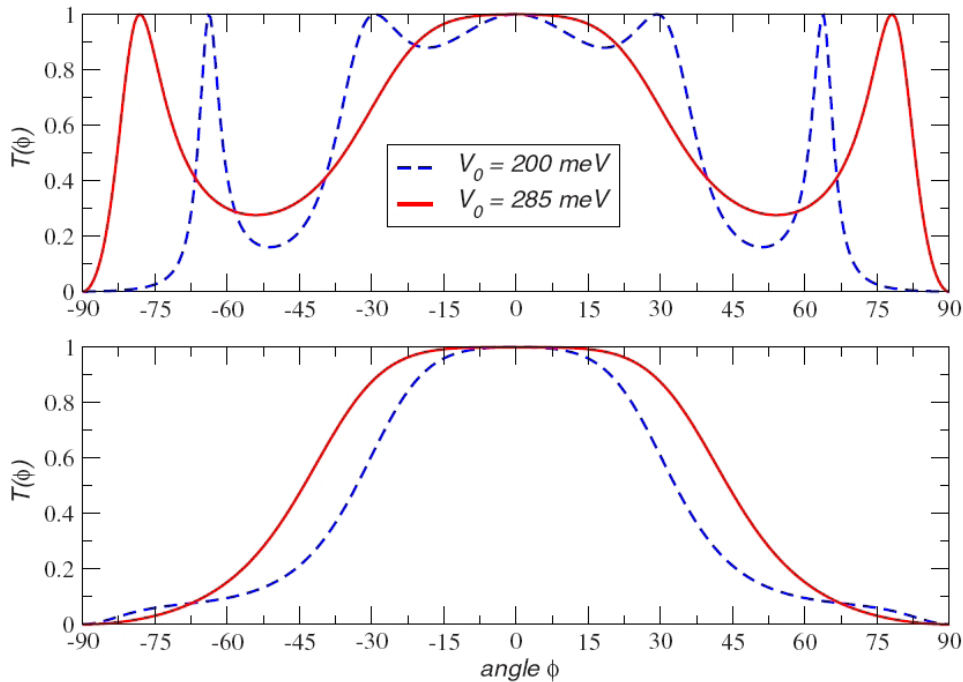
Figure 15. The transmission results from equation 7 for different values of V$_0$, where D = 110nm (top), and D = 50nm (bottom). Aside from normal incidence there are potentially other points of absolute transmission as well. This absolute transmission is a manifestation of the Klein paradox. Figure from reference [67]

2.5.1.4. DOS for Graphene and Semiconductors

Fig. 16 shows a comparison between the electronic structure of graphene and a two-dimensional electron gas (2DEG) in a standard semiconductor. The band structure of graphene has a linear dispersion, and valence and conductance band touch at the K and K' points: $\mathbf{E(q) \approx \pm \sim \hbar \upsilon_F |q|}$ (**Fig. 16(a)**). Considering the fourfold degeneracy due to spin and valley degeneracy, this dispersion relation leads to a two-dimensional density of states $\mathbf{D_{2D}(E) = 2|E|/\pi \hbar^2 \upsilon_F^2}$. The density of states is linear in energy and vanishes at the Dirac point for ideal graphene. (**Fig. 16(b)**).

The dispersion relation of a typical direct band gap semiconductor is depicted in **Fig. 16(c)**. It is parabolic with a gap between valence and conductance band.

The conductance band dispersion can be described as $\mathbf{E = E_C + \hbar^2 k^2 / 2m^*}$, for the valence band it is similar. The two-dimensional density of states is zero for the region of the band gap, and constant in the valence and conductance band region: $\mathbf{D_{2D}(E) = m^*/\pi \hbar^2}$.
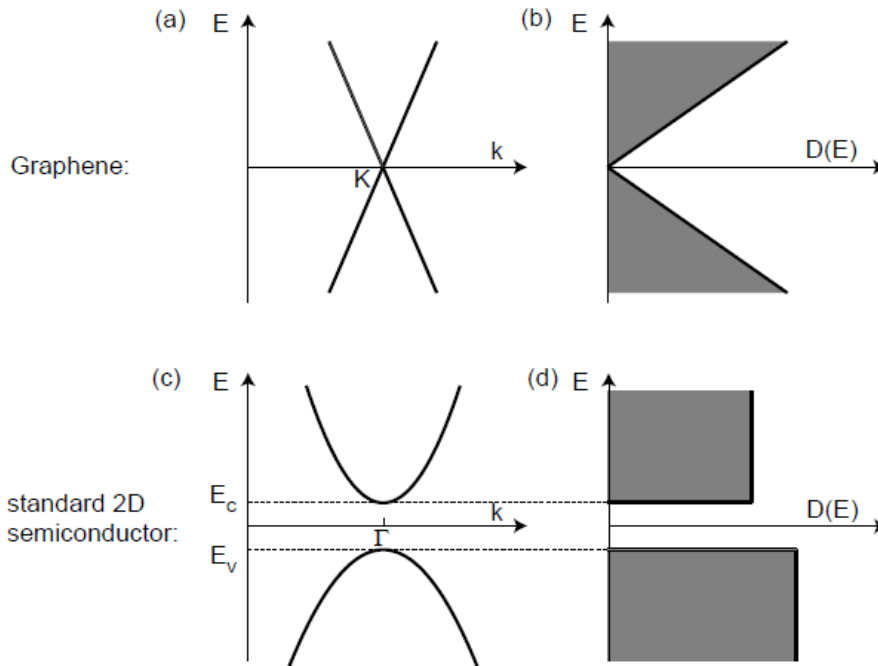
Figure 16: Comparison between graphene and standard 2D semiconductor electron gases. (a) Schematic drawing of the band structure of graphene around the K-point. (b) Density of states of graphene. (c) Schematic drawing of the band structure of a standard semiconductor with direct band gap. (d) 2D density of states for a standard semiconductor.

The unusual properties mentioned here are just a few examples of the many interesting properties of graphene based materials. The literature on graphene, despite its relatively young age, is enormous, and it is almost impossible for one to keep abreast of the rapid progress that this field is currently undergoing. This makes graphene an exciting field to be involved in.

2.6. Optical properties

Graphene can be profitably used in photovoltaics, thanks to the remarkably high optical transmission over a wide spectral range, coupled to the mentioned high electron mobility, extremely useful for charge collection in solar cells [68, 69].

In optoelectronics, graphene based devices have been designed and studied for high-speed radiation detection [70], light emission from organic LED [71], as transparent conductive sheets substitutive of ITO, for example for touchscreens, liquid crystal displays or photovoltaic cells [72-74], or ultracapacitors for energy storage [75], and solid state mode-lockers in fiber lasers [76].

In view of the optimization of the graphene performances, it is evident that optical properties, such as reflectance, transmittance and absorption, deserve particular attention.

In general the optical properties of graphene are governed by its dynamical conductivity $\sigma(\omega)$. For frequencies greater than the typical inverse scattering time $\omega >> t^{-1}$ the optical conductivity $\sigma(\omega)$ within a single-particle tight-binding theory can be written as [77, 78] :

$$\sigma(\omega) = \frac{ie^2\omega}{\pi\hbar}\left[\int_{-\infty}^{+\infty}\frac{|\epsilon|}{\omega^2}\frac{df_0(\epsilon)}{d\epsilon}d\epsilon - \int_{0}^{+\infty}d\epsilon\frac{f_0(-\epsilon)-f_0(\epsilon)}{(\hbar\omega+i\delta)^2-4\epsilon^2}\right] \qquad (2.30)$$

where $f_0 = (\exp[(\epsilon - \mu)/k_BT] + 1)^{-1}$ is the Fermi function, μ is the chemical potential, k_B is Boltzmann's constant, and T is the temperature. The first integration in Eq.2.30 gives the contribution from intraband processes, which after integration read as:

$$\sigma^{intra}(\omega) = \frac{2ie^2 k_B T}{\pi\hbar(\omega + i\tau^{-1})} \ln\left[2\cosh\left(\frac{\mu}{2k_B T}\right)\right] \tag{2.31}$$

which for temperatures $\mathbf{k_B T} \ll \mu$ reduces to

$$\sigma^{intra}(\omega) = \frac{ie^2|\mu|}{\pi\hbar(\omega + i\tau^{-1})} \tag{2.32}$$

The second term in equation 2.30 describes the contribution to the conductivity from interband processes.

After integration of the second term we arrive at

$$\sigma^{inter}(\omega) = \frac{e^2}{4\hbar}\left[\theta(\omega - 2\mu) - \frac{i}{2\pi}\ln\frac{(\omega + 2\mu)^2}{(\omega - 2\mu)^2}\right] \tag{2.33}$$

Where $\theta(\omega - 2\mu)$ is the step function. We can see that for transition frequencies $\omega \gg \mu$, the logarithmic singularity is cut off with the temperature and the expression for σ ^{inter} reduces to:

$$\sigma^{inter}(\omega) = \frac{e^2}{4\hbar} \tag{2.34}$$

This result has important implications for the optical properties of graphene. Since σ ^{inter} is constant, optical properties such as the transmission T and absorption A should also be constant according to:

$$A = 1 - T = \frac{4\pi}{c}\sigma = \pi\alpha = 2.3\% \tag{2.35}$$

The relationship A = 1 − T holds because the reflectance R is negligible (R = $1/4\pi^2\alpha^2$T < 0.1%). Experimental verification of this theoretical prediction has been given by Nair et al. [79] **Fig. 17** shows the results obtained by Nair et al..

For light transmission throughout the visible, graphene indeed only absorbs 2.3% of impinging light. Further, absorption as a function of graphene layers is additive which points towards a negligible interlayer coupling with respect to the optical properties of graphene.
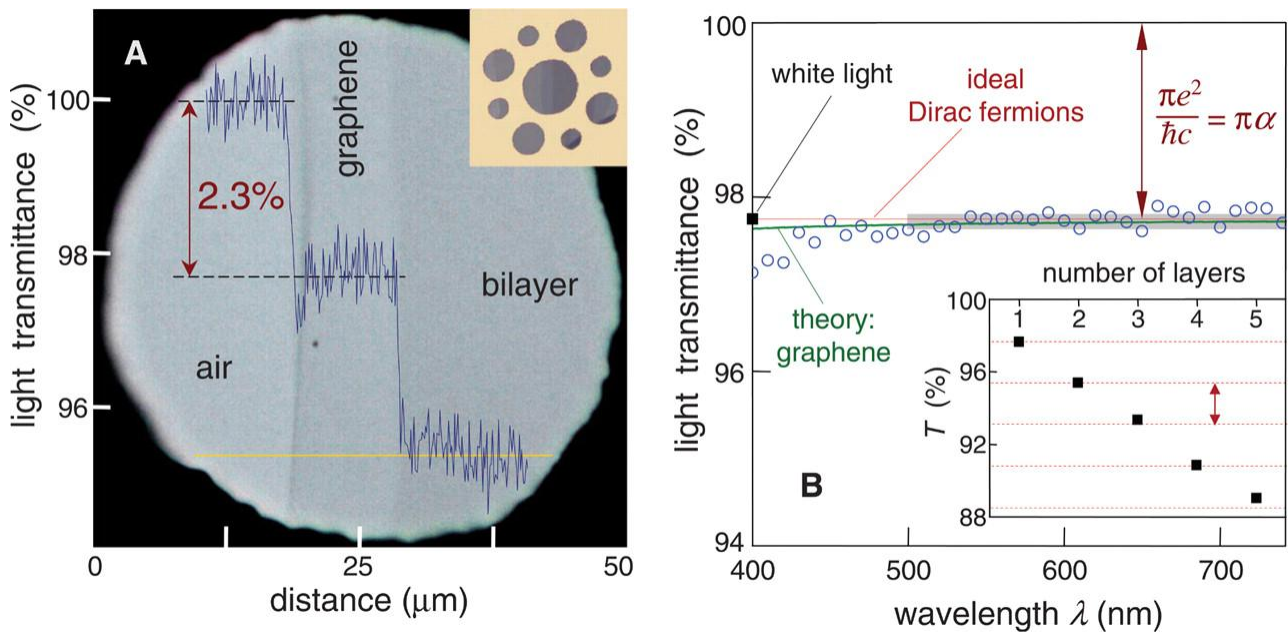
Figure 17: Universal transmission of graphene. (a) Experimental setup for measuring the optical transmission of graphene; micromechanical exfoliation of graphene on a copper grids with apertures of varying size. (b) Constant transmission through a freely suspended graphene layer over visible wavelength range. The inset shows transmission values as a function of the number of graphene layers. Images are taken from [79]

Chapter 3
Graphene production and graphene characterization techniques

3.1. Introduction

Despite the intense interest and the continually experimental progress, widespread implementation of graphene devices has yet to occur. This is primarily due to the difficulty of reliably producing high quality samples, especially in any scalable fashion [80]. The challenge is really 2-fold because performance depends on both the number of layers present and the overall quality of the crystal lattice [81- 84]. So far, the original top-down approach of mechanical exfoliation has produced the highest quality samples, and a number of alternative approaches to obtaining single layers have been explored.

One of the key elements in graphene discovery, and still nowadays in handling it in most studies, resides in the use of an appropriate substrate that maximizes the optical contrast of the carbon atom monolayer in the wavelength range of maximal sensitivity for the experimentalist.

3.2. Graphene production

In all my experiments single layer graphene was produced by a micromechanical cleavage exfoliation technique by sticky "scotch"-tape of graphite to peel-off a few layers of graphene.

Graphite is a polycrystalline material originating from one of the following sources:

1. Highly Ordered Pyrolytic Graphite (HOPG);

2. Kish graphite;

3. Natural graphite.

HOPG is a synthetic product widely used in different scientific experiments as a substrate. The controlled growth of HOPG, based on thermal decomposition of hydrocarbon, allows it to be chemically clean and AB stacked, however it may still have lattice defects, and it was principally used in this thesis for graphene production.

The second type, Kish graphite is a byproduct of the metal industry and is produced during the cooling of molten steel. Therefore, it is expected to have metallic impurities, yet can also be chemically purified. Natural graphite is mined around the world in the form of a lump, amorphous and crystalline flake graphite and its properties strongly depend on the geography. However, even good quality monocrystals of natural graphite may contain up to 5 % of rhombohedral phase which is known to have smaller average interlayer distance [102]. The choice of this particular type is based on the big lateral size of monocrystalline areas it is made of and therefore the big size of graphene flakes extracted (up to 50 μm).
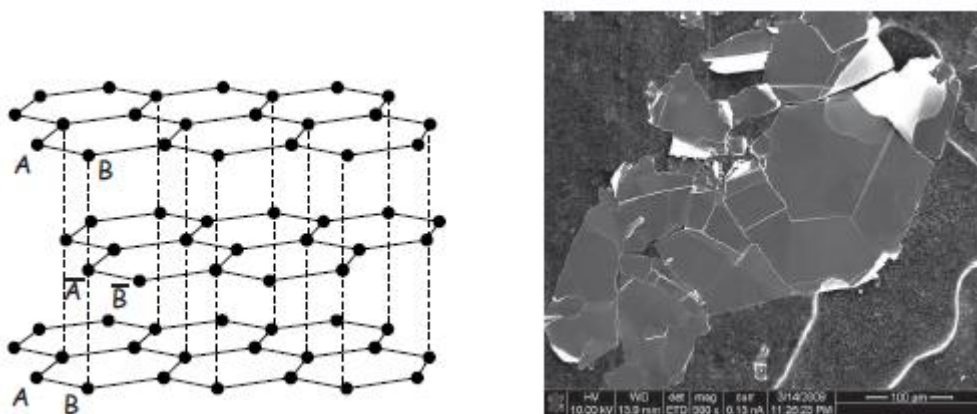
Figure 18: Hexagonal graphite lattice arranged in Bernal A-B stacking. SEM image of natural graphite, scale bar 100 μm.

Part of the fabrication process took place in a cleanroom. Since the air is a complicated mixture of common gases (nitrogen, oxygen, argon, carbon dioxide etc.) and a large number of traces of other species, it is impossible to count all contaminants arriving at a flake surface during and after its fabrication. In the ideal case graphene should not be exposed to the air, but this is difficult to achieve and at present moment no methods

have been reported whereby a graphene flake is always kept (when fabricated and measured) in a clean, controlled atmosphere.

An adsorption process is usually classified as chemisorption (e.g., a covalent bond formation) or physisorption (weak van der Waals forces), depending on the type of the force responsible for the attractive interaction. Graphene will easily physisorb different atoms and molecules and their presence can influence the charge transport. If the surface is heated, the energy transferred to the adsorbed species will cause it to desorb. Thus, in the presence of such species in the environment, there will be a dynamical balance between incoming and leaving adsorbates. The rate of leaving follows an activation rule, $\propto x \exp(-u/RT)$, where x is the fraction of the surface covered by adsorbate, u is the binding energy and T is the temperature of the surface. The rate of arriving is $\propto (1 - x) p$, where p is the partial pressure of the vapor. Therefore a contaminated surface can be cleaned by increasing its temperature (annealing) in a clean environment.

3.3. Experimental method for graphene fabrication

In order to locate and contact graphene flakes, an orientation grid is needed on the substrate, **fig.19**. Usually this is done by writing a matrix of cross-like markers or number referenced markers, **fig.20**, using electron beam lithography (EBL) and then evaporating Ti/Au or Cr/Au (2 nm/40 nm) and lift-off.
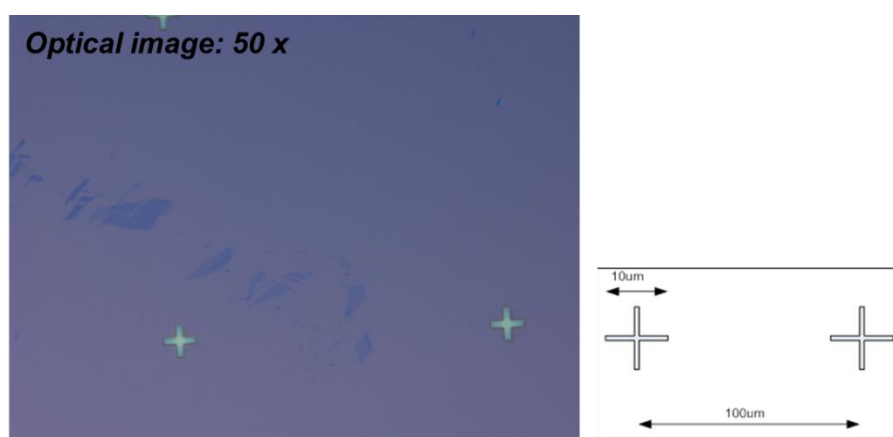
Figure 19. Cross-like markers with related size

Figure 20. A grid referenced-markers The distance is 75um along x and 40um along y .

So the wafers needed a cleaning treatment prior to graphene deposition, in fact, the surface can potentially get contaminated during the shipping and storage.

Here, I report two cleaning methods that I used:

1st Method

- Acetone, room temperature (ultrasonic aggravation, 5-10 minutes), wet transfer to

- IPA, room temperature (ultrasonic aggravation, 5-10 minutes),

- dry in N$_2$ flow.

2nd Method

- Acetone, boil 56∘C (ultrasonic aggravation, 5-10 minutes), wet transfer to

- IPA, room temperature (ultrasonic aggravation, 5-10 minutes),

- dry in N$_2$ flow.

The first method is a standard method of cleaning. The second is a more aggressive version of the first, utilizing normal behavior of organic solvents to increase its reactive ability at higher temperatures.

At this point, the exfoliation method took place: it consist to use a common adhesive tape and to repeat the stick and peel process a dozen times which statistically brings a 1 μm thick graphite flake to a monolayer thin sample.

Because the inter-layer Van der Waals interaction energy is of about 2 eV/nm^2, and the order of magnitude of the force required to exfoliate graphite is about 300 nN/μm^2 [85], this extremely weak force can be easily achieved with an adhesive tape.

Historically, the first method that succeeded in the isolation of a single graphene sheet has been the micromechanical exfoliation of highly oriented pyrolytic graphite (HOPG) in the very simple fashion method developed by Novoselov et al. in 2004 [2, 53,86].
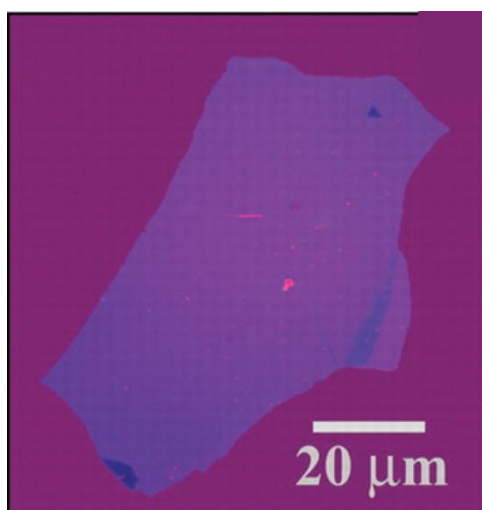

Figure 21. Single layer graphene was first observed by Geim and others at Manchester University. Here a few layer flake is shown, with optical contrast enhanced by an interference effect at a carefully chosen thickness of oxide.

In principle, any adhesive tape could be used for the cleavage of graphite into graphene, but we use single-side adhesive 'Nitto' tape (SWT-20), which is used in the semiconductor industry for wafer protection. The tape consists of a specially formulated acrylic adhesive ∼ 10 μm thick on a PVC film carrier.

A small piece of graphite (usually a few mm lateral size and less than 100 μm thick) is placed between two pieces of the tape and then two tapes are torn asunder, splitting the graphite piece into halves (**Fig.22**).
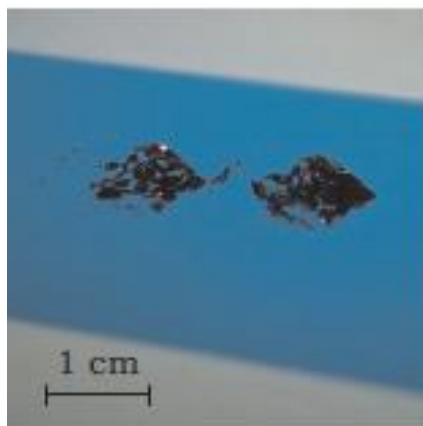
Figure 22. Nitto adhesive tape (blue) with graphite flakes (black)

This procedure is repeated a few times until the graphite covers a significant area on the tape surface and in order to cleave the graphite into thinner flakes (**Fig. 23**), so, each part has to be thinner than the original one.

Between five and ten folding events is a good number: if the tape is folded less often, the graphite is not cleaved enough, and the resulting graphene flakes are too thick. If folded too many times, the graphene flakes become smaller, with more glue residues. In a next step, the graphene flakes are transferred onto a wafer prepared with the alignment markers.
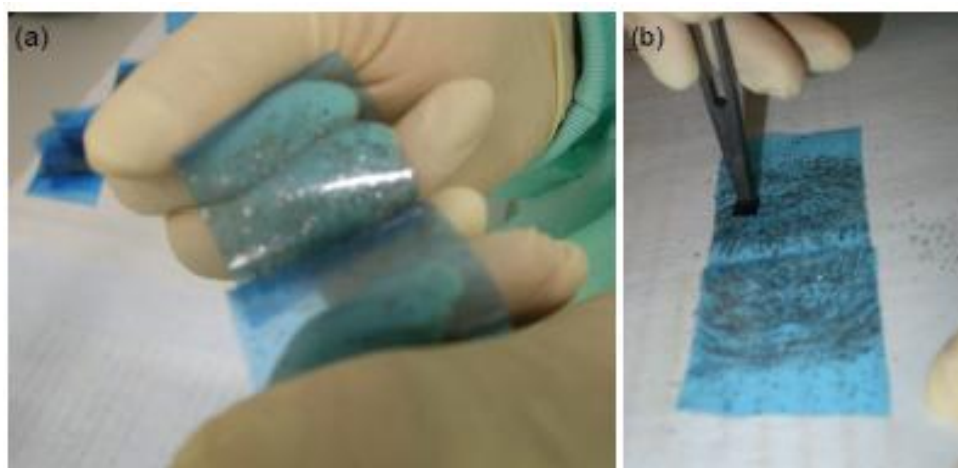
Figure 23: Deposition of graphene (a) Folding of the sticky tape, covered with graphite flakes (b) Transfer of the flakes from the tape to the Si/SiO2 substrate.

A chip is placed on top of the tape in a region where it is uniformly covered by graphite exfoliated, and then pressed against a freshly cleaned wafer with a pressure of 100 N/cm^2 with tweezers or with a finger, and removed straight away. This creates many flakes on the surface of the wafer with a variety of thicknesses from a monolayer up to a few microns held by the Van der Waals force. Once the tape is attached to the surface, the best result usually comes with the force applied perpendicular to the surface. Increasing the vertical pressure leads to an increase in the total flake density but can damage the surface oxide layer and leaves unwanted dust.

Typically, graphite flakes occupy a few percent (0-5 %) of the total wafer area. The presence of organic contamination (e.g. skin secretion, exhaled air, vacuum grease) on the surface often increases the flake adhesion and therefore the covering ratio.

After a number of graphene depositions done according to the procedure explained above, we have found that two depositions done in exactly the same way do not result in the same average flake density. The reason for this can be that the adhesion force depends on the environmental conditions.

So, another technique could be used: once the tape is attached to the surface of the chip, without pressing each other, it is possible to keep them in a vacuum chamber for 24 hours, and finally remove the tape gently.

The action of the pressure in the chamber that decreases the value regularly up to 10^{-6}Torr, plays the rule to press uniformly the tape on the all surface. The effect is to increase the total flake density and to improve the flake adhesion on the surface.

After removing the sample from the tape, glue residues can to be left on the sample, so limiting the carrier mobility [89,90]. A post-deposition cleaning and heat treatment, as well, is thus required to remove the residue.

Therefore, as already said, the chips are cleaned in acetone and isopropanol, and a short ultrasonic pulse is applied to make sure the flakes chosen for processing in the next step stick well to the surface, and if possible followed by 2 min of oxygen plasma ashing.

Others graphene preparation is attempted by different approaches, one of this that is a more "scalable" method to produce graphene is to grow it on a suitable planar surface using chemical vapor deposition (CVD), molecular beam epitaxy (MBE), or by the

reduction of SiC [93-95]. These methods can now produce both multilayer and single-layer graphene on large-area substrates. The clear advantage is that one can cover an entire wafer with graphene by such growth methods.

Neverthless, despite tremendous progress with alternatives, mechanical exfoliation with cellophane tape still produces the highest quality graphene flakes available and it remains the best method in terms of electrical and structural quality of the obtained graphene, primarily because it benefits from the high-quality of the starting single crystalline graphite source. The size of the deposit is also appreciable, and can be purchased on supporting substrate in the fraction of square millimeter. However it will be challenging to bring this approach to large scale production level, which is why other strategies have attracted a renewed interest.

3.4. Techniques for the detection and characterization of graphene flakes

After the deposition, the chip is covered by many graphene flakes of different thicknesses. An optical microscope (Nikon Eclipse LV-150) is used to detect thin flakes **Fig.24**.
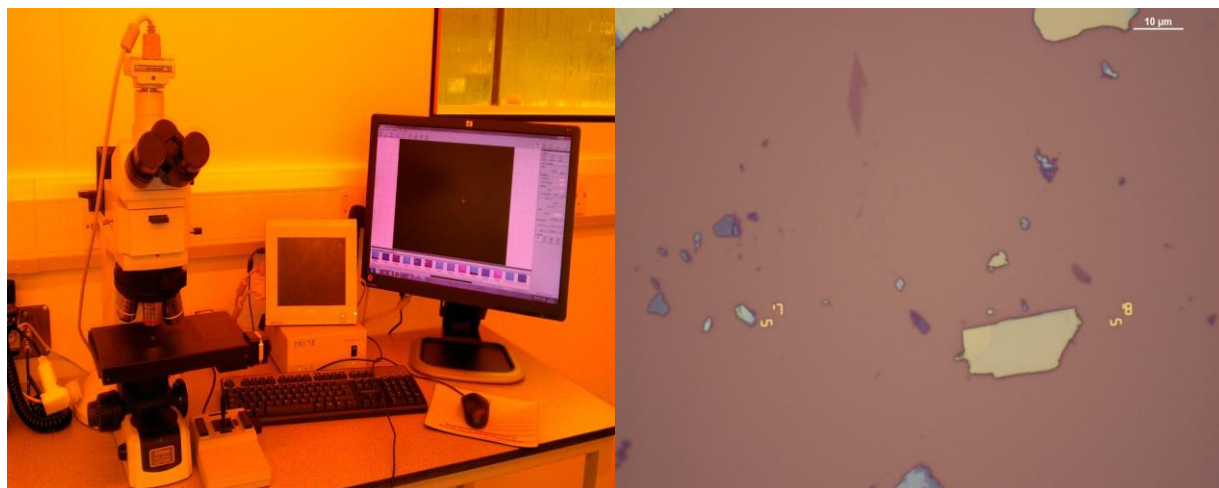
Figure 24: Optical Microscope and an image of the graphene flakes of different thicknesses captured by it.

3.4.1.1. Optical Microscope

The visibility of graphene has been studied theoretically [103] and experimentally [104]. Optical microscopy is a technique that allows to quickly discern the thickness before moving on to more precise and less direct methods such as Raman spectroscopy, used to selectively investigate small portions of the sample.

The advantages of the optical microscope imaging are: i) graphene can be viewed optically with minimal magnification (4x, 10x, 20x, 40x, 100x); ii) Approximate thickness is determined by color (black, white, blue, purple, pink).

Disadvantages of this technique lie on: the uncertainty of the identification and the invisibility of graphene when using an unsuitable substrate and/or inadequate source wavelength [103].

3.4.1.2. Study of contrast for rapid identification of Graphene

Graphene flakes with various thicknesses both single layer graphene (SLG) and few layer graphene (FLG), once the flakes are deposited on a dielectric substrate, can be rapidly identified by white light contrast analysis via an optical microscopy survey [2].

Contrast in optical image strongly depends on many parameters [110, 111]: the incident angle of the light source, the luminance of the source, the thickness of the dielectric film, the dielectric material, the substrate of the thin dielectric film, and, obviously, on the graphene flake thickness.

This rapid identification mechanism, is essentially based on the contrast raising from the interference of the reflected light beams at the air-to- graphene, graphene-to-dielectric and (in case of thin dielectric films) dielectric-to-substrate interfaces [103].

The thickness of the oxide layer has to be carefully chosen. It was shown that the flake's contrast oscillates as a function of the oxide thickness, due to the interference of the reflected light., and only for very specific thicknesses, the contrast of a single graphene layer is strong enough to be detected in white light due to the flake's opacity and the increased optical path [13].

Thin films of $SiO_2/Si(100)$ (300 nm) are the typical substrates used for such a rapid identification [109], for which the apparent contrast of graphene monolayer is at about 12% at 550 nm, where the sensitivity of the human eye is optimal. This phenomenon is easily understood by considering a Fabry–Perot multilayer cavity in which the optical path added by graphene to the interference of the SiO_2/Si system is maximized for specific oxide thicknesses [86, 87, 88].

Graphene is not completely transparent to the light source radiation, but it is visible thanks to the changes of optical paths of the light through the oxide thickness.

We can explain this phenomenon using Fresnel theory, a model for reflection and transmission of graphene based on normalized conductance that does not require the use of graphene's refractive index, but rather the use of the optical conductance.
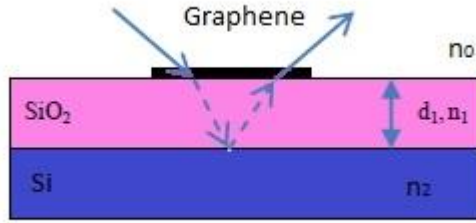
Figure 25. Optical paths of the light on Graphene/SiO_2/Si structure

The universal optical conductance of a graphene monolayer in the limit of massless Dirac fermion bandstructure is $\mathbf{Z_0} = \mathbf{e^2 / 4\hbar}$. By normalizing the optical conductance with free space impedance Z_0 we have:

$$Z_0 \sigma_0 = \sqrt{\frac{\mu_0}{\epsilon_0}} \cdot \frac{e^2}{4\hbar} = \pi \alpha \qquad (3.1)$$

where α is the fine structure constant. The universal conductance, when normalized by the impedance of free space, is a fundamental physical constant independent of unit system.

If **m** is the number of graphene layer normalized conductance is **Z = mσ₀Z₀=mπα**, we model graphene as a surface carrying a surface current, sandwiched between two materials, numbered as 1 and 2.

The boundary conditions **fig.28** for the electromagnetic fields are
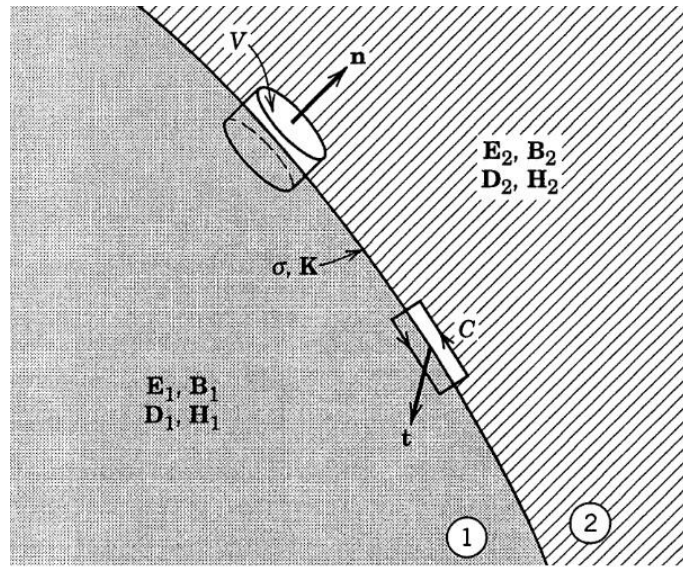
$$n \; x \; (E_2 - E_1) = 0$$

$$n \; x \; (H_2 - H_1) = J \tag{3.2}$$

Figure 26. A schematic diagram of boundary surface (heavy line) between different media.

where **n** denotes the interface normal between materials 1 and 2, E_i and H_i are the electric and magnetic field vectors in each medium, respectively, and $J_s = m\sigma_0 E_s$ is the surface current density with the optical conductance $\sigma_0 = e^2/4\hbar$ for each of the m layers. The Fresnel coefficients for **s** and **p** polarized incident light are:

$$r_s = \frac{n_1 \cos\theta_i - n_2 \cos\theta_t - m\pi\alpha}{n_1 \cos\theta_i + n_2 \cos\theta_t + m\pi\alpha}$$

$$t_s = \frac{2n_1 \cos\theta_i}{n_1 \cos\theta_i + n_2 \cos\theta_t + m\pi\alpha} \tag{3.3}$$

$$r_p = \frac{n_1 \cos\theta_t - n_2 \cos\theta_i - m\pi\alpha \cos\theta_i \cos\theta_t}{n_1 \cos\theta_t + n_2 \cos\theta_i + m\pi\alpha \cos\theta_i \cos\theta_t}$$

$$t_p = \frac{2n_1 \cos\theta_i}{n_1 \cos\theta_t + n_2 \cos\theta_i + m\pi\alpha \cos\theta_i \cos\theta_t} \tag{3.4}$$

where **θi** is the angle of incidence and $n_1 \sin\theta_i = n_2 \sin\theta_t$ defines the angle of refraction. For a finite aperture, we need to include the incident and the transmitted angles through our optical system. The intensity of reflected light for a finite aperture is:

$$I = \frac{1}{2}I_0 \int \left(|r_s(\theta_i)|^2 + |r_p(\theta_i)|^2 \right) d\Omega \tag{3.5}$$

where I_0 is the incident intensity and $d\Omega$ is the differential solid angle subtended by the imaging optics.

At normal incidence the power Transmittance is:

$$T = \frac{n_2}{n_1} |t|^2 \tag{3.6}$$

transmission coefficient is given by:

$$|t|^2 \approx 1 - \pi\alpha \tag{3.7}$$

Where:
$$\alpha = \frac{e^2}{4\hbar\pi c\varepsilon_0} \approx 1/137$$

Graphene only reflects < 0.1% of the incident light in the visible region, rising to ~ 2% for ten layers. Thus, we can take the optical absorption of graphene layers to be proportional to the number of layers, each absorbing $\textbf{\textit{A} ≈ 1 − \textit{T} ≈ π\alpha ≈ 2.3\%}$ over the visible spectrum.

The absorption of graphene can be modulated by an external gate field [176]. This is because interband absorption within a range of $2\Delta E_F$, where ΔE_F is the field-induced shift of the Fermi level from the Dirac point, should be blocked **fig. 27**.
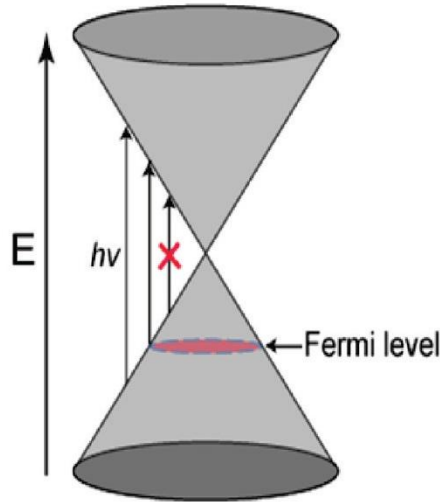

Figure 27. Schematic illustration of the optical transitions in a (field) doped single layer graphene. When the excitation (photon) energy is less than the difference $2\Delta(E_F - E_{Dirac})$, the transition is forbidden.

The best visibility of graphene can be obtained by ***contrast ratio***, also known as the visibility, which is simply the difference in reflected optical intensity from graphene and substrate, $I_{graphene}$ and $I_{substrate}$ respectively, and normalize the difference with respect to the substrate reflection intensity:

$$C = \frac{(I_g - I_s)}{I_s} \cdot 100\% \tag{3.8}$$

Where $\mathbf{I_g}$ is the reflected optical intensity of the graphene and $\mathbf{I_s}$ is the reflected optical intensity of the background.

On low-index substrates, such as glass $n_2 = 1.52$, graphene's conductance is sufficient to produce a 7% contrast ratio in optical reflection at normal incidence. High-index substrates, such as silicon, require a low-index layer of carefully controlled thickness to produce visibilities exceeding 1%, **fig.28**.
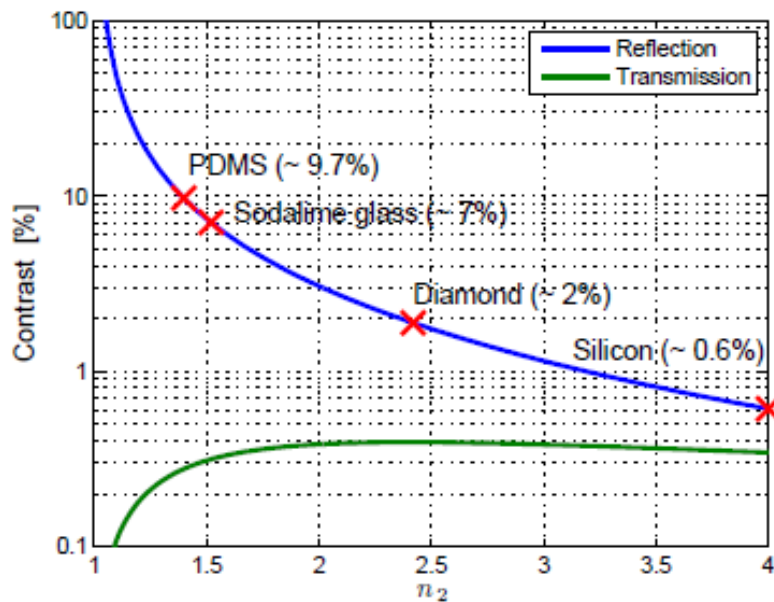
Figure 28. Reflection and transmission contrast as a function of substrate refractive index n_2. The transmission contrast here is plotted as a positive contrast

Fig.29 shows a photograph taken under an optical microscope of graphene flakes consisting of few-layer graphene, comprising also a single-layer region (indicated by circle). For increasing thickness of the graphite flakes, the color changes under the optical microscope.

Figure 29: Optical and SEM image of a monolayer
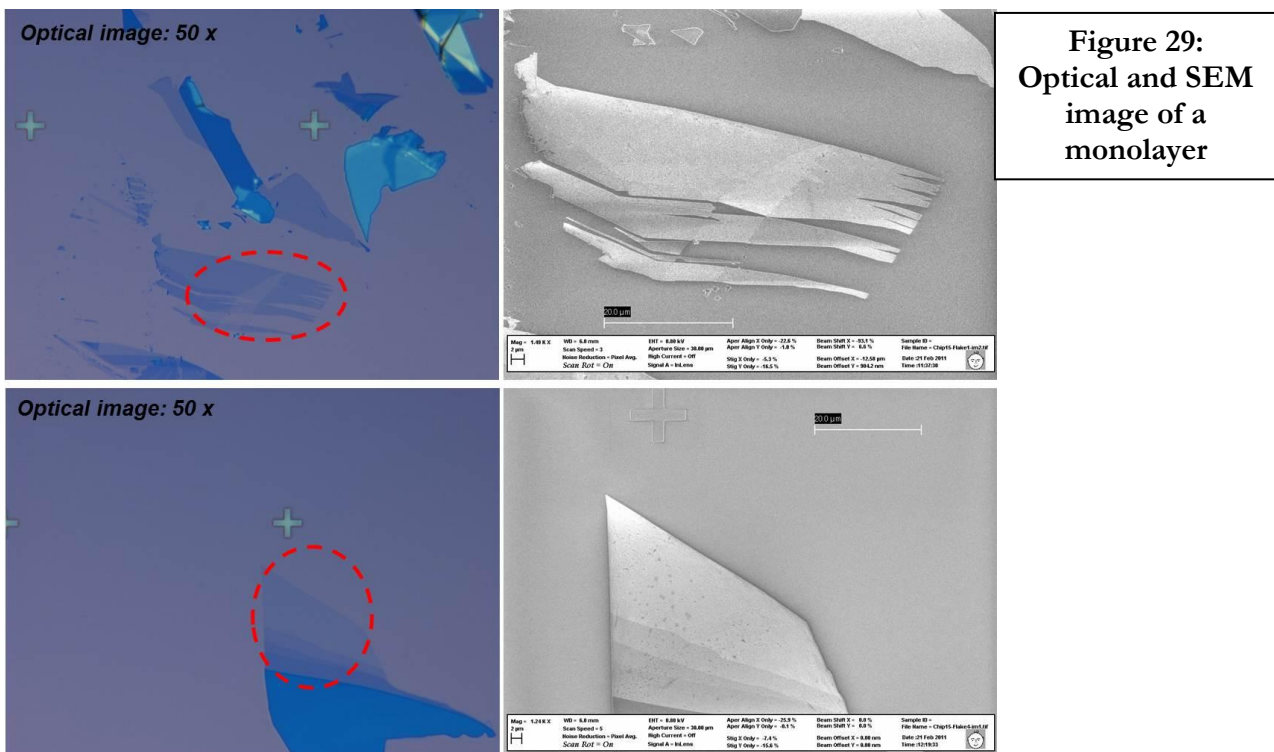
3.4.1.3.   Raman scattering

A corresponding assignment of graphene in the single, double and multi-layer phase is made with Raman spectroscopy.

Raman scattering is a fast and non-destructive technique that provides a direct insight on the electron–phonon interactions, which implies a high sensitivity to electronic and crystallographic structures. It has therefore been extensively applied to the structural investigation of carbon materials and more particularly of nanotubes [113].

In 2006, Ferrari et al. reported a method to identify few layer graphene flakes using Raman spectroscopy [114-116], the inelastic scattering of monochromatic light involving phonon creation / annihilation in the medium of interest is used to study vibrational and rotational modes in a material.

Raman spectroscopy is particularly well suited to molecular morphology characterization of carbon materials. Every band in the Raman spectrum corresponds directly to a specific vibrational frequency of a bond within the molecule. The vibrational frequency and hence the position of the Raman band is very sensitive to the orientation of the bands and weight of the atoms at either end of the bond.

Moreover, resonance Raman studies, where the energy of the excitation laser line can be tuned continuously, can be used to probe electrons and phonons near the Dirac point of graphene and, in particular allowing a determination to be made of the tight-binding parameters for bilayer graphene.

We use a laser excitation length of 532 nm (2.33 eV), delivered through a single-mode optical fiber, whose spot size is limited by diffraction. Using a long working distance focusing lens with a numerical aperture NA=0.80, we obtain a spot size of about 400 nm. As the used laser power is below 2 mW, heating effects can be neglected.

The two main signatures are the G peak at $\lambda \approx 1580$ cm^{-1} and the G' or 2D-peak at $\lambda \approx 2670$ cm^{-1}, for visible excitation (except for UV excitation, the Raman spectra of carbon films are dominated by the sp^2 sites, because visible excitation always resonates with the π states).

In the case of disordered sample or in the edges, we can see as showed in the figure below the disorder-induced D band at half of frequency of G' band, at 1360 cm^{-1}.

The D band is an efficient probe to assess the level of defects and impurities in graphene. It is for example completely silent for high-quality graphene such as micromechanically exfoliated, except in proximity of the edges.

Moreover, D'-band denotes another weak disorder-induced feature which appears at ≈ 1620 cm^{-1}. **Fig.30**
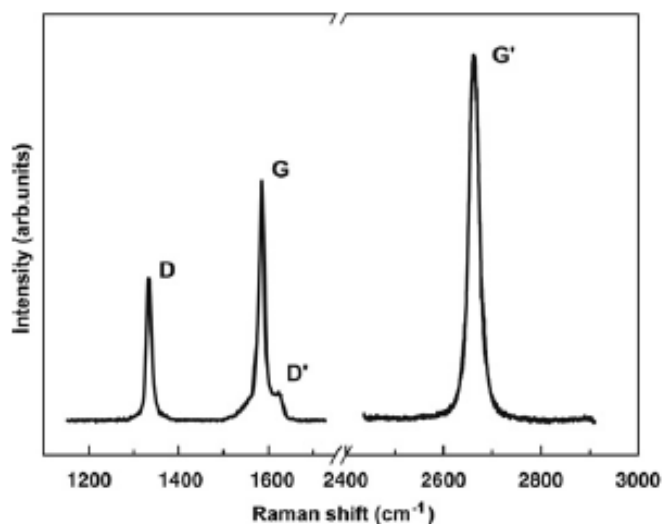
Figure 30. Raman spectrum of a graphene edge, showing the main Raman features ref. [117]

The D peak is due to the out-of-plane breathing mode of the sp^2 atoms and is active in the presence of a defect [117,118].

The G-band of graphite materials is caused by scattering of the incoming laser light due to in-plane bond stretching phonons with zero momentum, it corresponds to a doubly degenerate phonon mode (E_{2g} symmetry) at the Brillouin zone center.

The G' band is referred to as the 2D band; both 2D and G' are accepted names for this band. The evolution of the 2D-band for different graphene sheets has been used for determining graphene thickness as well as for probing electronic structures through the double resonance process.

Both the D and G' bands exhibit a dispersive behavior since their frequencies in the Raman spectra change as a function of the energy of the incident laser, E_{laser}.

The origin and the dispersive behavior in the frequency of the D and G' bands originate from a double resonance (DR) Raman process [119-121].
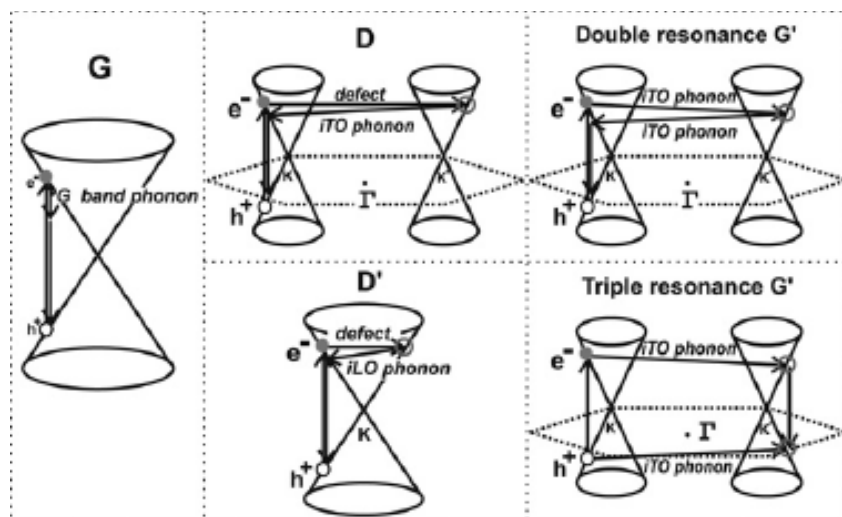

Figure 31: Intravalley and intervalley process

Here an example showing the difference in the Raman spectra between graphene and graphite **Fig.32**. The most obvious difference is that the G' band at 2700 cm^{-1}, is much more intense than the G band in graphene compared to graphite.
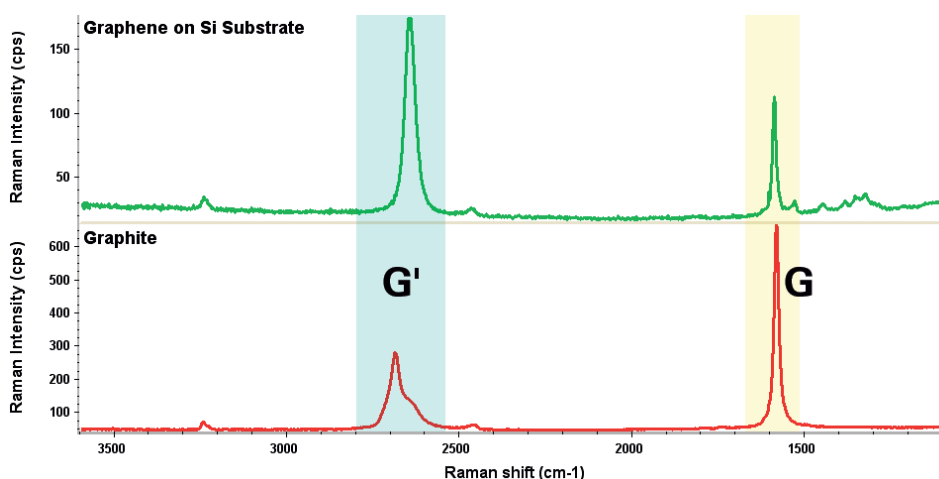

Figure 32: Raman spectroscopy is a powerful diagnostic tool for the study of graphene. The G (near 1584 cm^{-1}) and G' (near 2700 cm^{-1}) bands.

The shape, position and intensity relative to the G' band of this peak depend markedly on the number of layers [123,124] **fig.33**. For two or more layers, a second peak

centered on 1685 cm^{-1} emerges and eventually dominates the first peak for more than three layers. Beyond five layers, the Raman multi-peak profile becomes hardly distinguishable from that of bulk graphite that is a complex group of bands between 2600 and 2750 cm^{-1} [114].
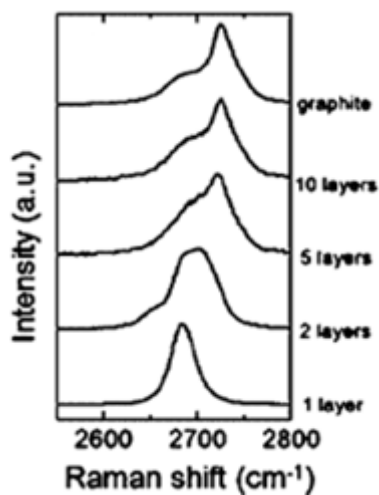
Figure 33: Significant changes due to the thickness of AB stacked flakes.

The G' band for monolayer graphene(1-LG) at room temperature exhibits a single Lorentzian feature centered on 2640 cm^{-1} , **Fig. 34** , which can shift to 2655–2665 cm^{-1} with a full width at half maximum (FWHM) of ≈ 24 cm^{-1}, this is a proof for the single-layer nature of the flake [113,125].
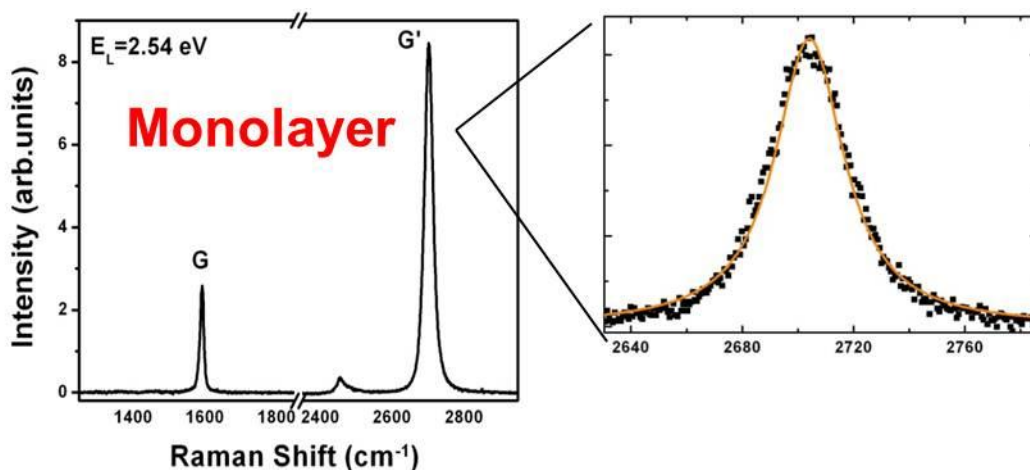
Figure 34. Monolayer, Symmetric and FWHM is ≤ 26 cm^{-1}

What is remarkable about this spectrum is the large intensity of the G' band relative to the G-band, and this large relative intensity of the G' band can be understood in terms of a triple resonance process shown in **Fig. 31**. This is a unique spectrum for all sp^2 carbons where all steps in the process (see **Fig. 31**) are resonant because of the linear E(k) dispersion.

In the case of bilayer graphene (2-LG) with Bernal AB layer stacking, both the electronic and phonon bands split into two components with special symmetries. The electrons in 2-LG have a parabolic E(k) dispersion relation showing a k^2 dependence near k=0 and have two conduction and two valence bands [126,127-129] as shown in **Fig.35.** The electrons are also affected by the interlayer interaction and they also split into symmetric and antisymmetric components. For the case of 2-LG, the DR conditions are more complex than in the case of monolayer graphene (1-LG) where there is only one main DR process contributing to the G' band.

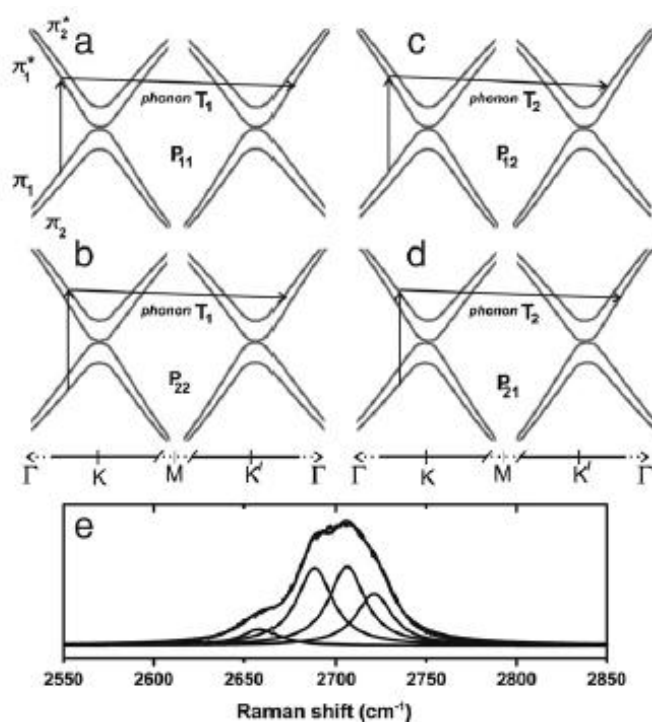Four different scattering processes occur as showed in the figure:

Figure 35: Schematic view of the electron dispersion of bilayer (2-LG) graphene near the K and K' points showing both π_1 and π_2 bands ref. [117]

These four different scattering processes give rise to four Raman peaks in the G'spectrum. **Fig. 35(e)** shows the Raman spectra of a bilayer graphene sample with AB stacking. The spectra is fitted with four Lorentzian **Fig.36** .
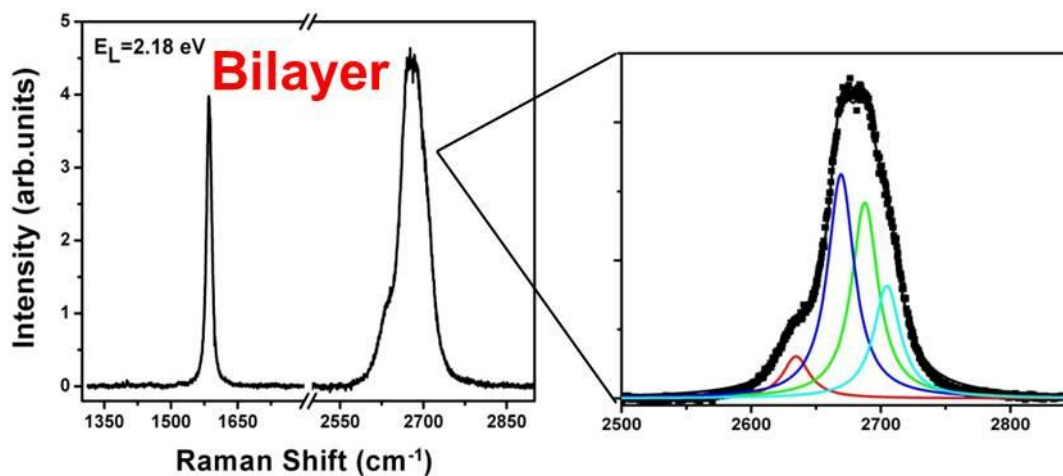

Figure 36: Asymmetric, and FWHM is ≥ 50 cm^{-1} Peak: 2666.7 cm^{-1}

Raman spectroscopy has proven to be useful to assess the quality of graphene and for counting layers [130, 131], but with few limitations because is only capable of distinguishing between the first three to four layers of graphene [132], more layers than that can not be identified except as few layer graphene flakes.

Raman spectroscopy is highly sensitive to doping [133, 134], defects and strain [135, 136, 137]. The phonons involved in Raman scattering interact strongly with defects, carrier concentration and strain fields, resulting in the utility of Raman scattering to infer such graphene sample information. However, interpreting Raman spectra becomes difficult due to the wide variety of phenomena that contribute to changes in the spectra.

Another technique, that I do not use in this work is AFM investigation that gives the most precise information on the layer thickness, and it was quite naturally one of the first techniques used to establish that the thinnest graphitic flakes first identified optically were indeed one-atom thick monolayers **fig.2b**

The typical thickness of graphene is 4 angstroms. The AFM measurements on monolayers also provide an estimate for the thickness of a dead layer between graphene and SiO_2. It changes from sample to sample and can vary between 5-10 angstroms [142]. The main disadvantages are the impracticability for systematic analysis on large area; it has also been found that AFM tips can destroy or scratch the layer surface.

Although AFM is too slow and limited in lateral scan size to be used as a primary identification method and in spite of the extra apparent height, AFM soft imaging modes are the best way to monitor the topological quality of substrate-supported graphene samples during the successive steps of device processing.

3.5. Analysis of Contrast and Raman Spectra of Graphene on different substrates.

The crucial experimental aspect lies in the choice of the substrate.

The role of interaction between substrate and the graphene sheets has not been sufficiently investigated and different conclusions were drawn by different groups. Wang et al [139], carried out systematical Raman study of monolayer graphene produced by mechanical cleavage on different substrates: standard SiO_2 (300 nm)/Si, Quartz single crystal, Si, Glass, PDMS, and NiFe.

In this thesis I have investigated the contrast and Raman spectra of graphene on several substrates (Glass, ITO, Diamond, etc..), because substrate effect is important for potential application and to realize optoelectronic devices (see Cap 6) of graphene.

3.5.1.1. Study of Best Filter

The optimization of the optical contrast of graphene with respect to the background color of the substrate has also been achieved by a number of image processing methods.

The simplest method, which is only suitable for 300-nm thick silicon oxide where the maximal contrast occurs at a wavelength of 550 nm, consists in displaying the green channel image normalized by its value on the bare substrate.

Alternatives to silica have been studied, here, and graphene is also visible in green channel image normalized on glass substrate.

With a simply program implemented in Matlab it is possible to extract the histogram (shown in **Fig.38**), that is designed to enhance the visibility of objects of interest in an image.

The intensity histogram, is a one-dimensional array that contains the frequency of each intensity value in an image. This is essentially a discrete representation of the probability density function for pixel intensities.

To calculate the intensity histogram we count up how many times we see each pixel value.

Figure 37, shows two optical images, under the same magnification and with blue and green filter, respectively, of the same flake exfoliated on a 1μm glass substrate.

The images are captured by a camera Nikon Eclipse LV-150, in reflection mode, on a small region of a glass-chip of 100um thick where natural graphite was exfoliated.
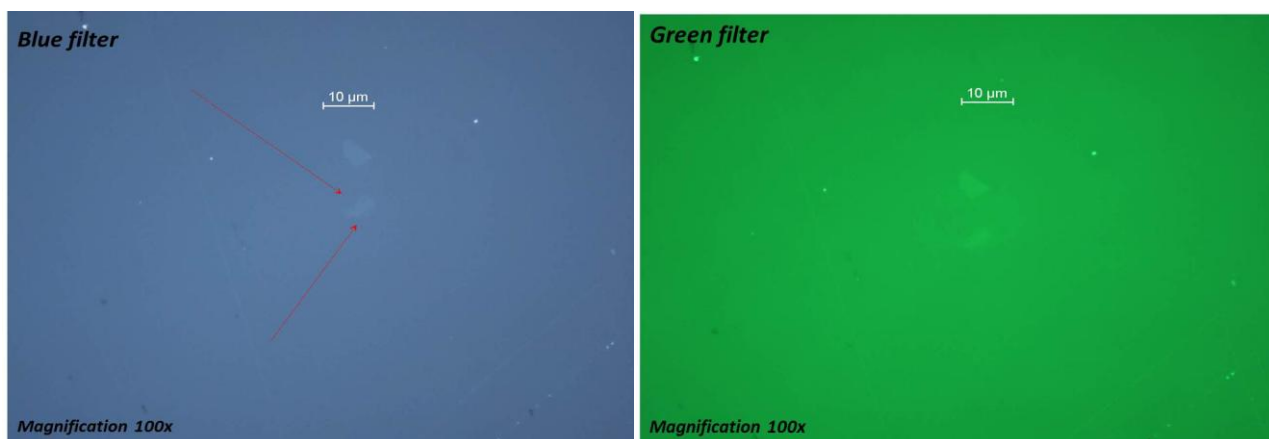

Figure 37. Exfoliated graphene on Glass 100μm substrate

An intensity image can be modeled as a function:

$$I: R^2 \rightarrow R$$

where the domain and codomain are continue, the domain is an Euclidean plane in the case of 2D images, while the codomain is proportional of the emitted source energy.

Continue image is converted in digital image through a samples process over spatial coordinates and followed by quantization, in which function values are digitalized.

The final result of the continue image processing is a matrix MxN, and a pixel is each unit cell of the matrix. The quantization process converts the codomain of the image in a discrete function with gray level values, L.

Thus, the histogram of a digital image with gray levels in the range [0, L-1] is a discrete function $\mathbf{h(r_k) = n_k}$, where $\mathbf{r_k}$ is the kth gray level (intensity) and $\mathbf{n_k}$ is the number of pixels in the image having gray level $\mathbf{r_k}$.

This histogram shows the number of pixels at each different intensity value found in that image.
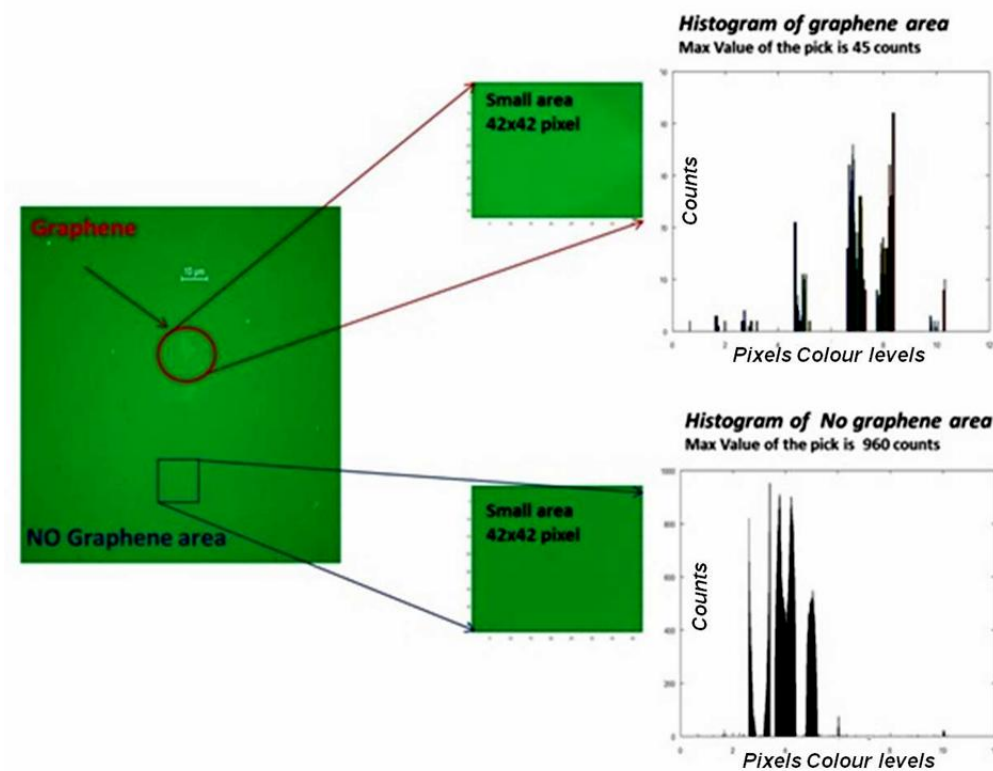

Figure 38: Histograms extracted with Matlab.

Taking in account the media intensity, for the selected objects in the perimeter:

$$I_M = \frac{\sum_k n_k r_k}{\sum_k n_k}$$

(3.9)

we can calculate the contrast ratio by eq. 3.8:

$$C = \frac{(I_g - I_s)}{I_s} \cdot 100\%$$

for two different filter: green and blue, we obtain:

$$C_g = 95\%$$

$$C_b = 44\%$$

So it is evident that the green Filter has the best contrast ratio because it increases the visibility.

If the value of the contrast is zero, the material is not detectable; if the value is between 0 and -1, the material appears darker than the substrate; and if it is between 0 and +1, the material is brighter than the substrate.

3.5.1.2. Contrast and Raman of Graphene exfoliated on Glass 100 μm

On highly transparent substrates such as glass, optical reflection microscopy gives a higher contrast ratio for graphene layer than transmission optical microscopy because the reflected light from the graphitic flake is compared against the low background reflection from the transparent substrate.

The use of graphene on glass is suitable for many applications:

- Solar Cells

- Transparent conductive coatings (TCO)

- ITO replacement (touch-screen applications)

- Graphene-enhanced optics

Our graphene flakes are deposited onto glass slides, by mechanical exfoliation.

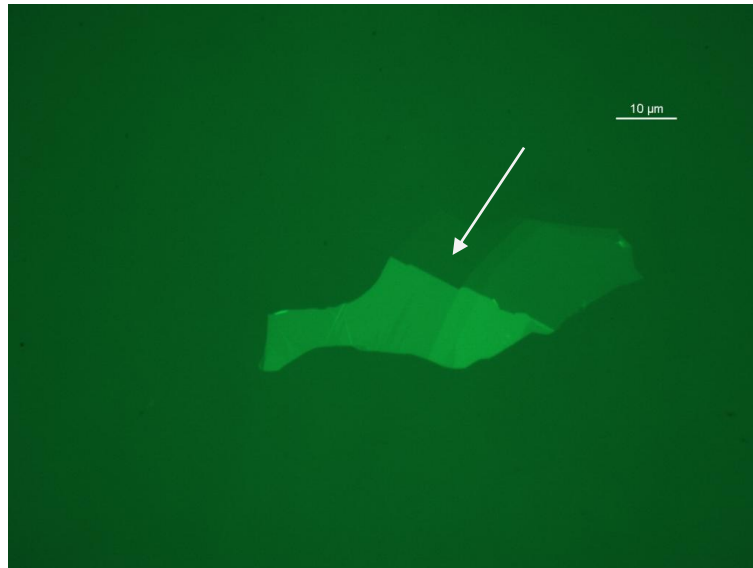After, the glass slides are cleaned with isopropanol then dried to remove dust, **Fig.39**.

Figure 39: Optical image of graphene flake with different layer on glass substrate

All optical contrast measurements reported in this thesis are taken with green light at a wavelength of 550 nm where the refractive index of the glass slides is 1,522±0,004. **Fig. 40** shows the optical reflection and transmission microscope setup.
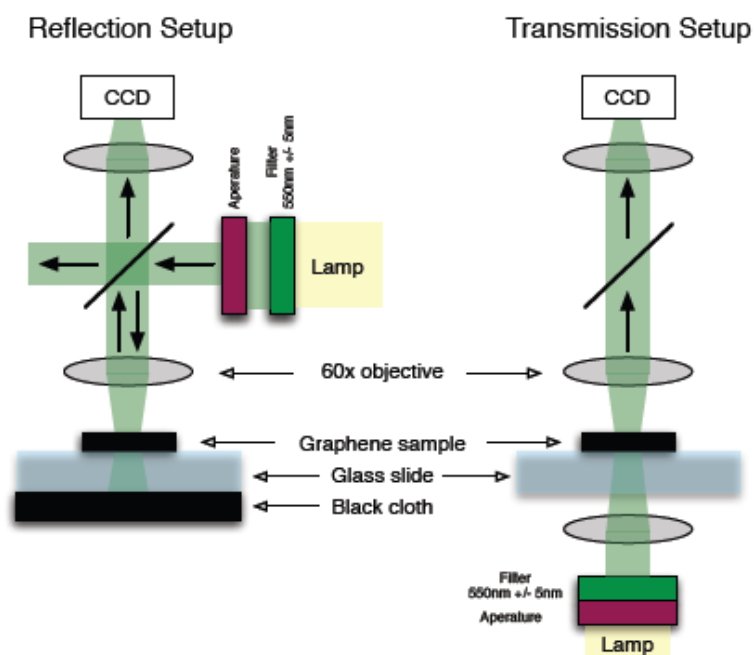

Figure 40: Microscopy setup

When light is incident on the graphene, it is both reflected to the objective and transmitted through the graphene to the glass slide. There the light is again reflected to the objective and transmitted through to the backside of the glass slide.

To minimize reflection from the backside, we place the glass slide on a black cloth.

With the reflected light passing through the objective, the beam splitter passes the light to either eye pieces or a camera mounted on the microscope. The measured optical intensity at each pixel is a function of numerous parameters such as lamp power, aperture size etc. but here we eliminate these effect by considering the reflection contrast CR as I described above, which is normalized to a pure glass.
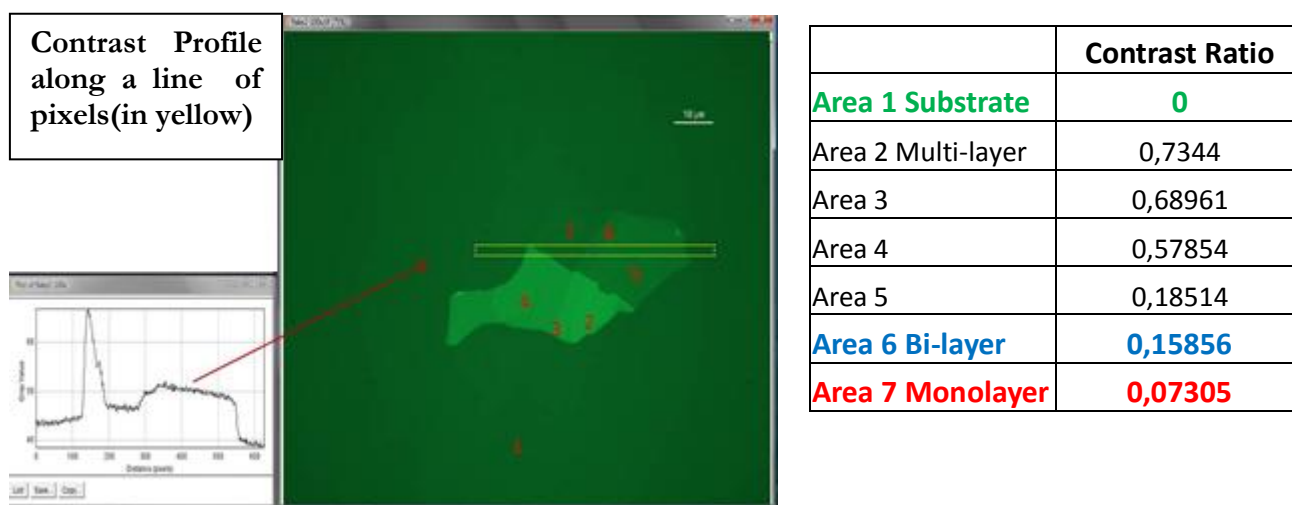

Contrast Profile along a line of pixels(in yellow)		Contrast Ratio
	Area 1 Substrate	**0**
	Area 2 Multi-layer	0,7344
	Area 3	0,68961
	Area 4	0,57854
	Area 5	0,18514
	Area 6 Bi-layer	**0,15856**
	Area 7 Monolayer	**0,07305**

Figure 41: Contrast Profile of the flake in figure 40 and Intensity and contrast values respectively.

For thin graphene sheets, the contrast value changes almost linearly with the number of layers. Moreover, there is more reflection from graphene than glass as Wang et al. reported in their work.

Glass slide substrates give a graphene reflection contrast of ≈ 7%, my results are in agreement to the contrast value extracted to other research group, **fig 42.**

In order to compare the contrast with others substrate, silicon gives only 0,6% reflection contrast, which is very low. Fortunately, graphene is deposited on a SiO_2/Si interferometer in many electronic devices and this increases the reflection contrast for

optical location of graphene samples. The contrast of a SiO_2/Si structure mostly depends on the refractive index and the thickness of the SiO_2, but an optimal structure can give $\approx$ 12% reflection contrast , only twice as large as what we obtain from bulk glass.
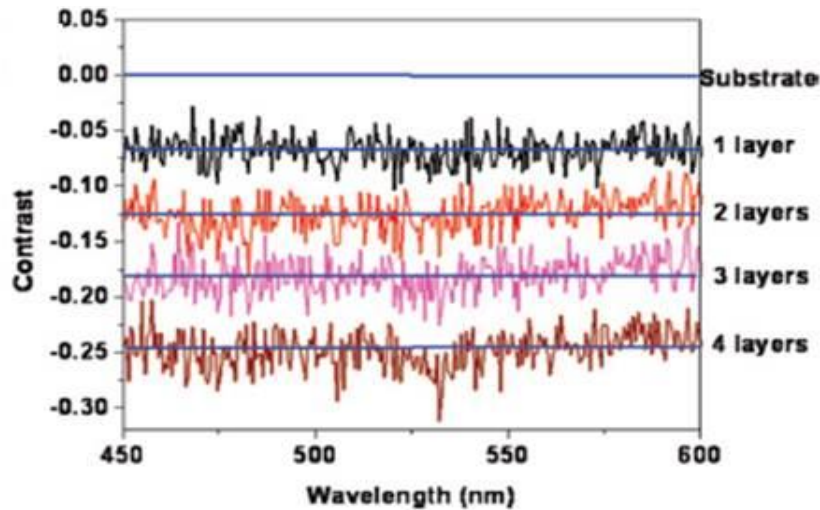

Figure 42: The contrast image of graphene sheets on quartz substrate, ref.[139]

Furthermore, I report the Raman Spectra of the bilayer area(5 in fig.41) , with the Lorentzian fit of the G' peak as well.

The results of this analysis confirm that the 1G peak at 1582 cm^{-1} has the same value as reported in [130-139], but the G' peak seems to be shifted up to 2683 cm^{-1}. Moreover the measured value of the FWHM is completely in agreement with the theory for bilayer graphene flake. Other measurements would be necessary to extract more information because no others works are present in literature.
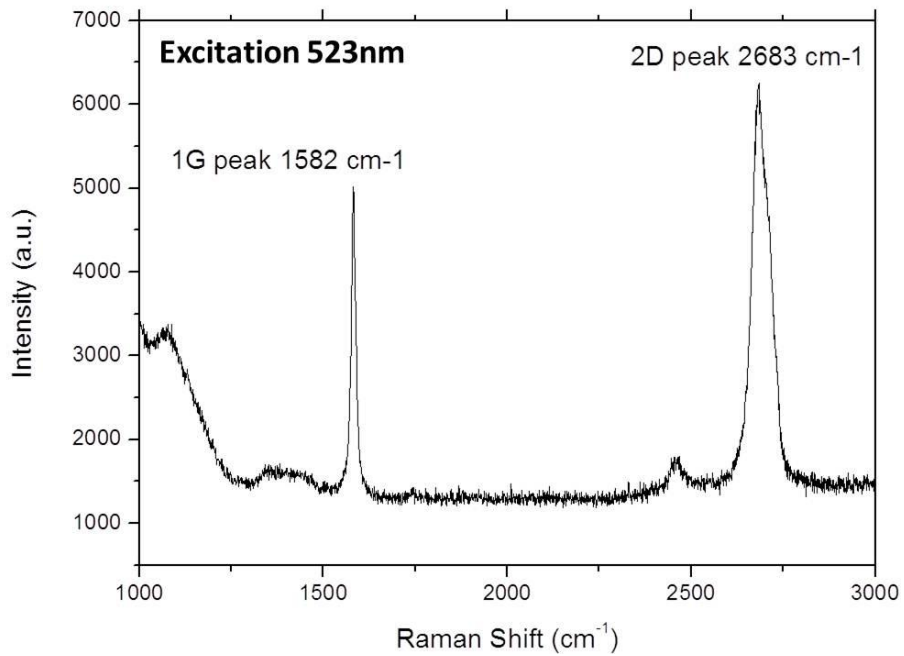
Figure 43: Raman Spectra of the area in the figure 41, indicated with the number 5. Spectra is displayed without any data manipulation, such as background subtraction or intensity attenuation.
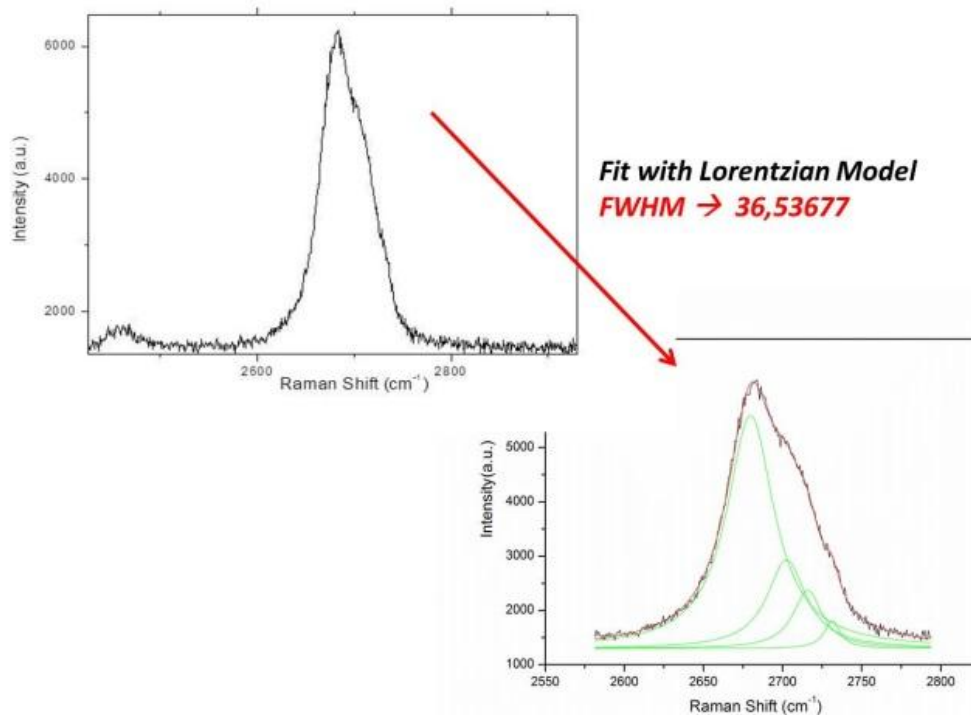

Figure 44: Lorentzian fit of the G' peak.

3.5.1.3. Contrast and Raman of Graphene exfoliated on ITO 40nm/1mm Glass

Since graphene is highly transparent and conductive, graphene could potentially be used as a transparent electrode in the visible spectrum in applications such as liquid crystal displays (LCD). Transparent electrodes are commonly made of indium tin oxide (ITO). ITO has several disadvantages, mainly high sheet resistance ($> 100 =2$), low mobility, large carrier density and only 70-85% transparency. Graphene outweighs ITO in all these fields: lower sheet resistance, much larger mobility, charge carrier density orders of magnitude lower and transparency of 94% for a monolayer. However, ITO can be deposited using sputtering, electron beam evaporation and physical vapor deposition.

The graphene flakes were transferred onto a conducting ITO substrate using mechanical cleavage. The left panel of **Fig. 45** shows an optical image of graphene flake on the ITO plate. The marked regions show different layers portions, from multilayer to single layer. Optically it is very difficult to identify a single layer on the ITO plate, whereas we can see a color contrast change for a few layer graphene.

The calculation of the contrast is reported in the right panel of the figure, confirming that for a monolayer the value is very low, 2.7 %.
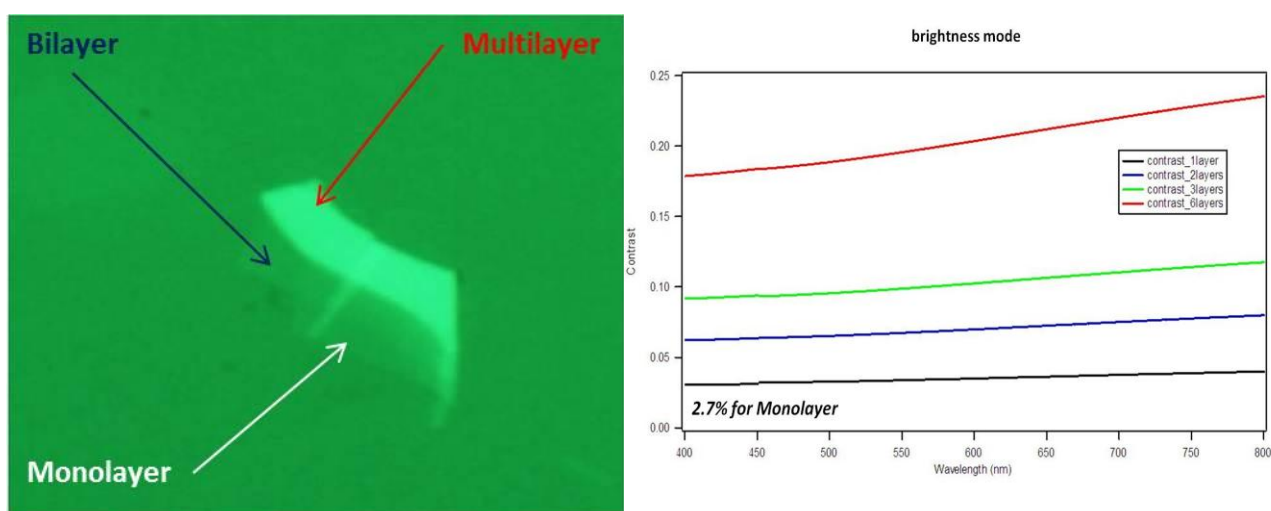

Figure 45: Optical Image and Contrast measurement of Graphene flake on ITO

The Raman measurement reported by Das et al in their paper [140] (as far as I know it is the only work conducted on the study of the Raman on ITO), shows the G and 2D bands appear at 1576 cm^{-1} and 2665 cm^{-1}, respectively. So the position of G and 2D bands are red shifted by 6 cm^{-1} and 20 cm^{-1}, respectively, compared to an undoped single layer graphene on the SiO$_2$/Si substrate.
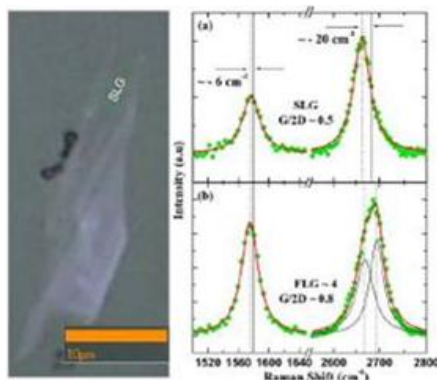

Figure 46. Raman spectra of graphene fakes on a different substrate like conducting indium tin oxide coated glass substrate.

Raman measurements I present here on a single layer part of the flake in **fig. 47**, are not completely in agreement with the work in ref [140].
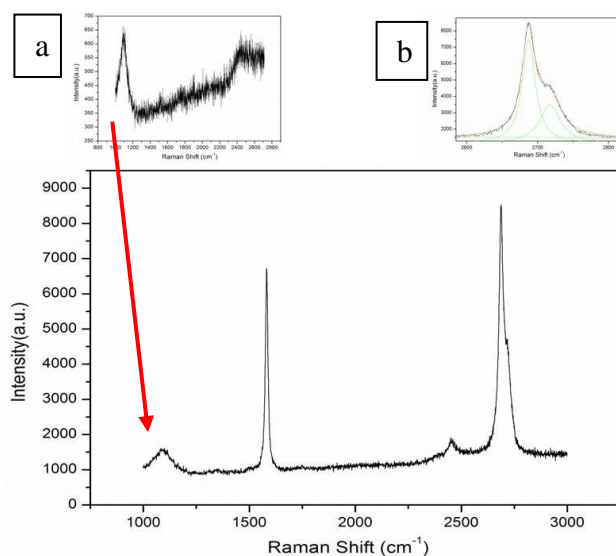

Figure 47. Raman Spectra of the graphene flake on ITO a) Raman of the substrate with a particular evidence of the peak at 1100cm^{-1}.b) Lorentian fit of the 2D peak with a drop probably due to the ITO behaviour.

First of all,the position of the 1G peak is at 1584 cm^{-1}, but the 2D peak is at 2720 cm^{-1} shifted rispect with the SiO$_2$/Si substrate. The value of FHMW is $\approx$ 22cm^{-1}, confirming that flake is a monolayer, but as the figure shows the 2D peak presents a not symmetrical shape with a drop, probably due to the ITO behavior.

Moreover the Raman spectra has the presence of another peak at 1100 cm^{-1},not reported in other works.

The origin of the red-shift is not yet fully understood as well as the asymmetrical shape of the 2G peak for a monolayer flake, and more studies are needed to understand the intriguing behavior of Raman spectra of graphene on conducting ITO plate.

3.5.1.4. Contrast and Raman of Graphene exfoliated on Diamond 40_50nm/SiO$_2$/p-Si

In order to conduct study of mobility of Graphene exfoliated on Diamond, it was necessary to study the property of contrast and Raman spectra before.

Fig.48, shows several area of the chip on which the graphite was exfoliated.

Graphene on the substrate made of 40-50nm Diamond upon SiO$_2$/Si structure is visible as yellow part, graphite is brown and diamond in the marked area in blue.

In the structure of Graphene on diamond, contrast has a low value as mentioned in the previous discussion, but in a three system layer using SiO$_2$/Si as substrate, the reflection intensity improves upon 20% and the visibility of graphene has the best contrast in the frequency of yellow **fig.49**.

It was demonstrated in [112] that, to enhance the optical contrast, the choice of a three interfaces system is preferable to the two interfaces one. Namely, the use of a thin dielectric film is preferable to the choice of a bulk dielectric as supporting substrate of graphene.
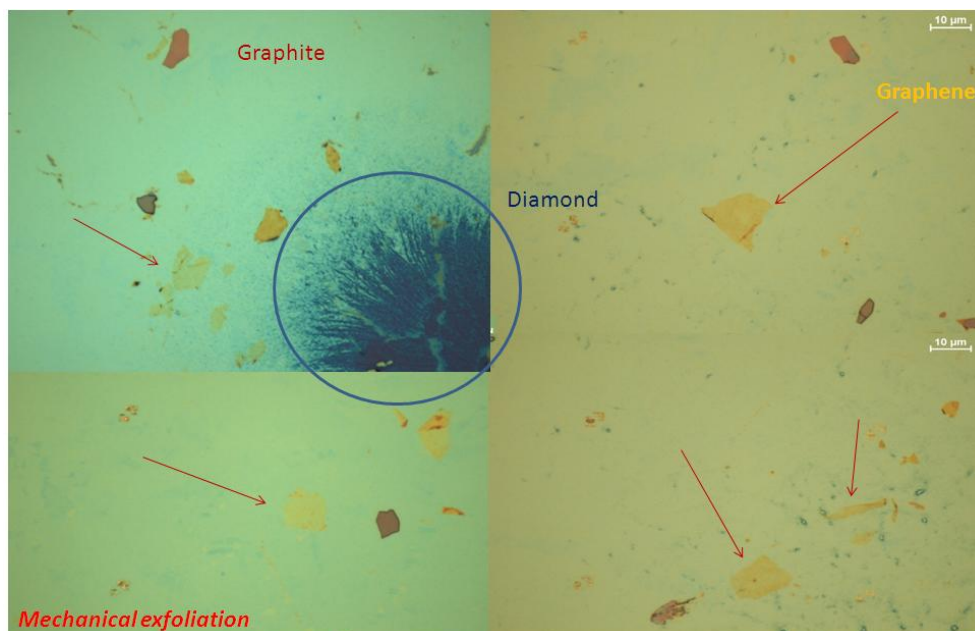
Figure 48: Different area of the sample on which Graphene, Graphite and Diamond are visible.
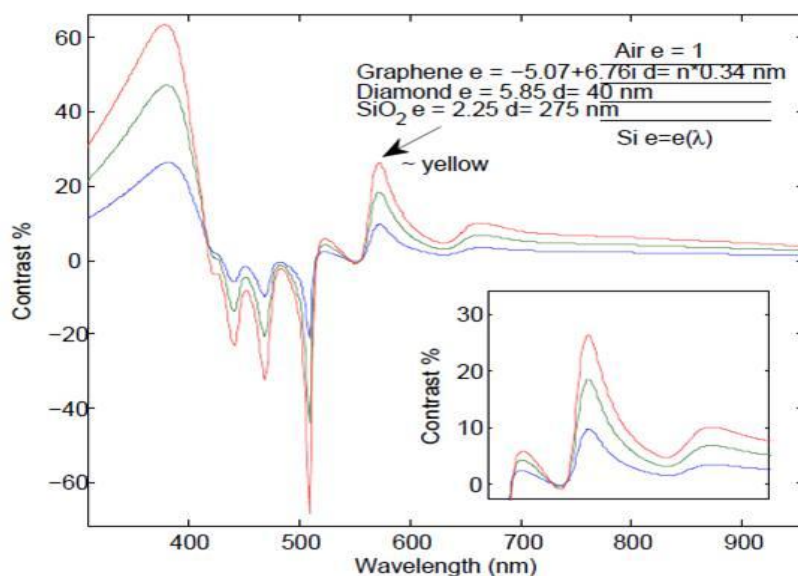

Figure 49: Calculation of the contrast of graphene in a three system layers. The simulation is supported by researchers of Centre for Graphene Science.

We individuated two flakes, over which the Raman Spectra in the **fig.50** presents characteristics peak of Diamond Spectra at 1332 cm^{-1} , the spectrum has also four extra features at 1150, 1350, 1480 and 1550 cm^{-1}. The peaks at 1350 cm^{-1} and 1550 cm^{-1} are the D and G peaks of amorphous carbon as reported in the **fig.51** by Andrea Carlo Ferrari and John Robertson ref. [141].
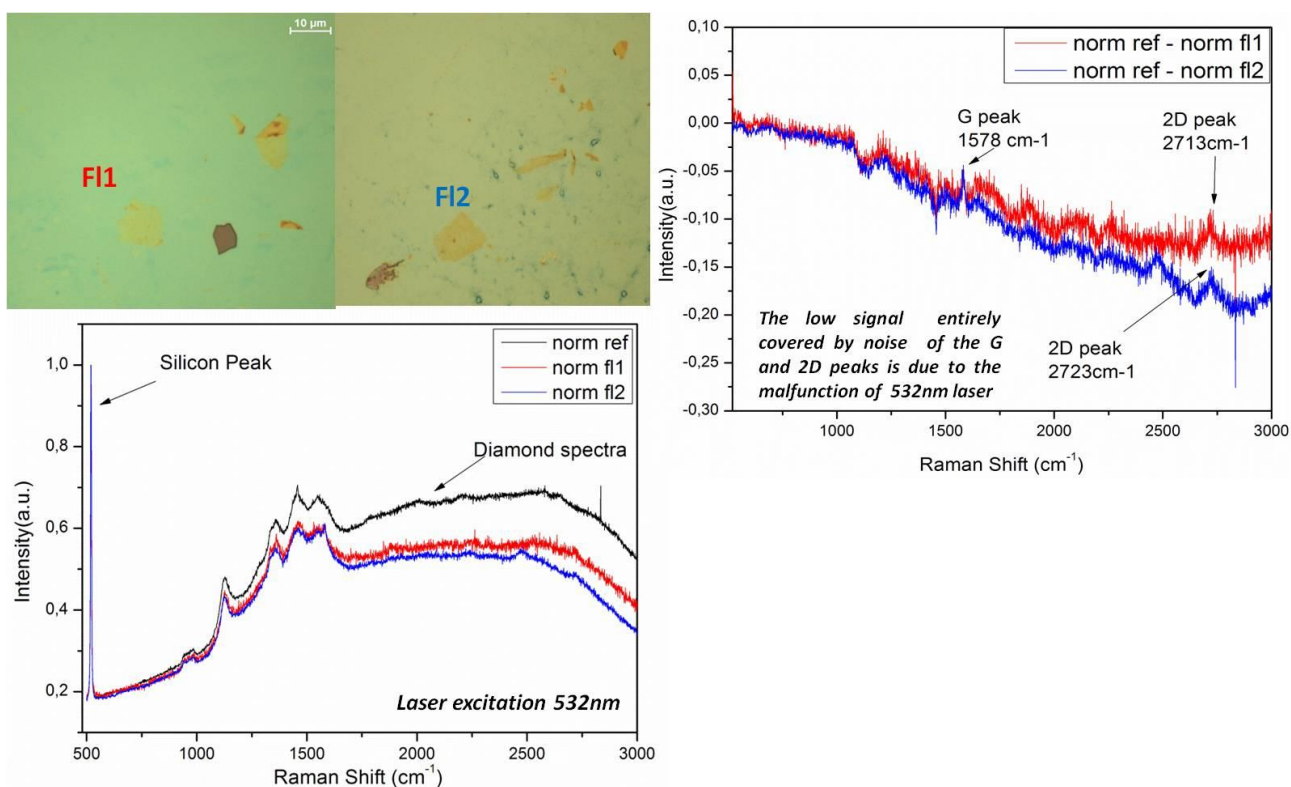
Figure 50: **Top**: Optical images of the graphene flakes in yellow, **on the left**: Raman of the background in black and the flakes normalized rispect with the silicon peak (520cm^{-1}), **on the right**: Raman of the flakes with background subtraction.

The low signal entirely covered by noise of the G and 2D peaks is due to the no correct alignment of 532nm laser, and it was not possible to extract the Lorentzian fit in order to recognize the structure of the individuated flakes, anyway what I describe is only a qualitative analysis, but more measurements are needed to clarify the nature of the diamond behavior and its sp^3 structure.
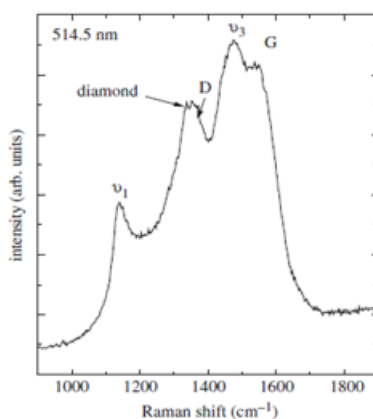

Figure 51: Raman spectroscopy of a typical nanodiamond sample. ref[141]
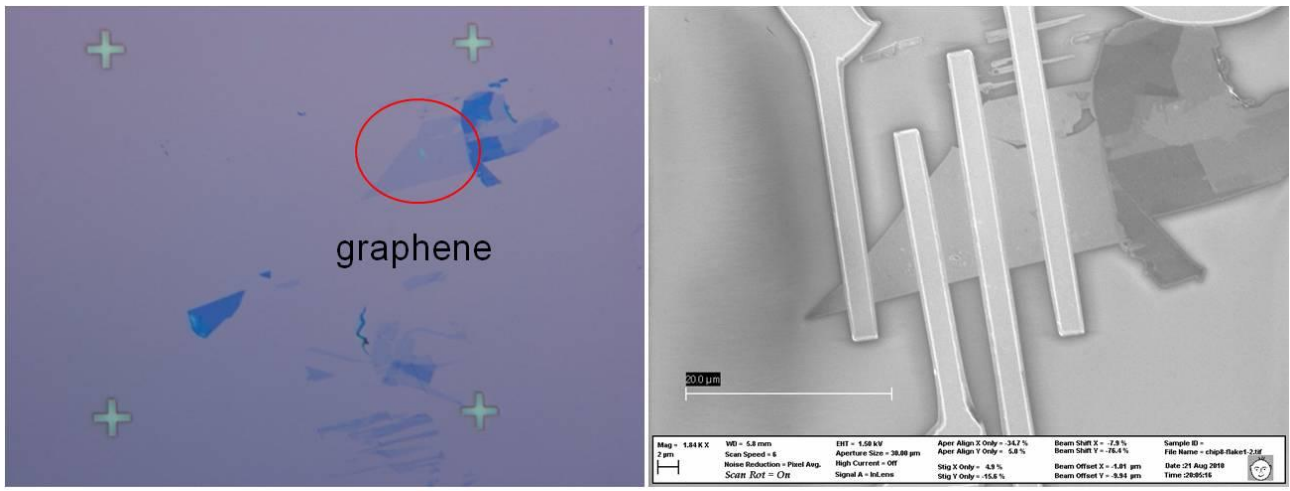
3.6. Processing of the flakes

After the selection and the characterization of the graphene flakes, SEM images of them are imported in a CAD tool which facilitates the design of contacts with given geometries for the fabrication of specific devices(transistor, TLM structures).

A graphene device is summarized in the following:

1. Cut the chip
2. Clean the chip

    – Rinse with DI water

    – Rinse with Acetone

    – Rinse with Isopropanol

3. Locate the flake under SEM and image it
4. Use this image to draw the metal pattern with respect to the closest alignment marker
5. MMA/PMMA (400nm) deposition

    – Spin at 4000 rpm

    – Dry each layer at 180 °C per 2 min

6. On the SEM align the chip and locate reference marker to write
7. Expose the MMA/PMMA covered chip to EBEM
8. Develop exposed MMA/PMMA
9. Check of the pattern on optical microscope; in case of mistake, remove MMA and PMMA and try again
10. Sputter metal, Cr/Au (2 nm/ 40 nm)
11. Lift-off to remove metal on the area with unexposed MMA/PMMA.
12. SEM image of the device
13. Electrical measurement

The result of the entire process is showed in the figure below **fig.52**, **fig 53** :
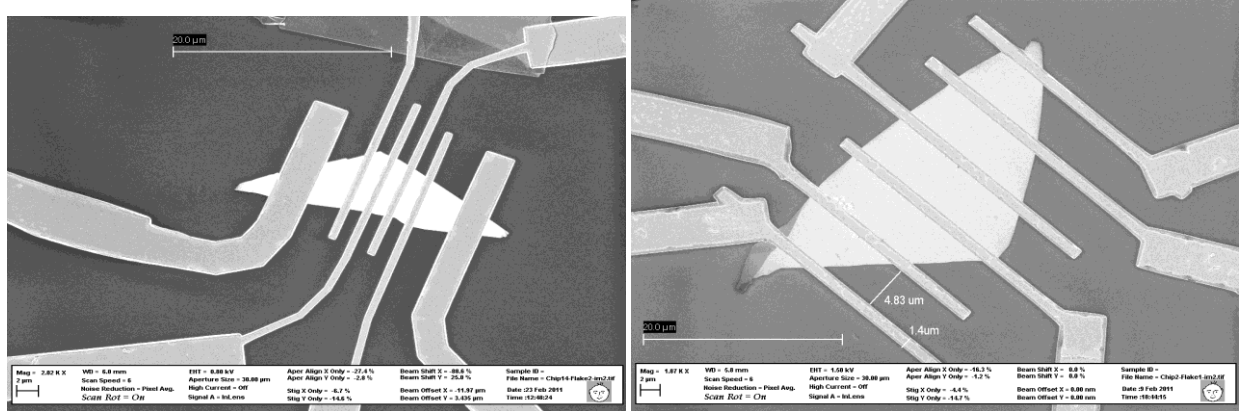
Figure 52: SEM images of the final structure on the graphene flakes during the research activities at Georgetown University
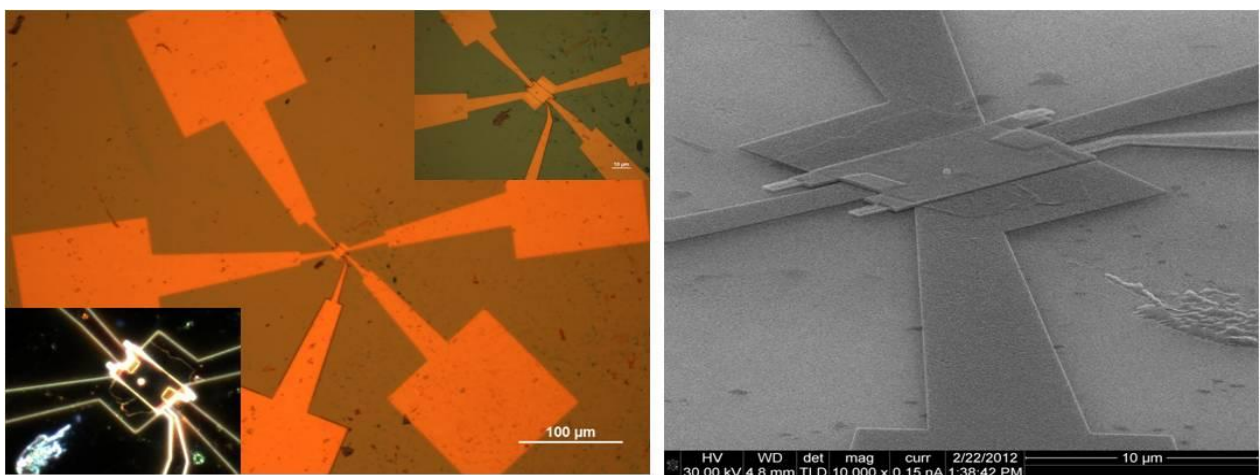

Figure53: Optical and SEM Images of GFET on Diamond /SiO$_2$ with supended Top Gate (Exeter Univesity). A particular of dark field optical microscopy set up (on the left).

Chapter 4
Graphene-based field-effect transistors

4.1. Graphene for Nanotransistors

A computer processor works through the use of silicon based transistors. A transistor can be used for various purposes, such as amplification, logic, and memory. All of these features are dependent on the physical properties of the material used to create the transistor. The current rapid progress in the field of electronics is largely dependent on advances in transistor technology. However, recently transistor technology has reached a plateau. The current methodology is centered on placing more transistors in the same unit area. Through this method the speed and throughput of processors have continued to rise switching speed of the transistor, has increased with the reduction of their dimension. This chapter will examine this new material, graphene, that could vastly increase the speed of a transistor as well as be a promising material to take over the Si-based technology.
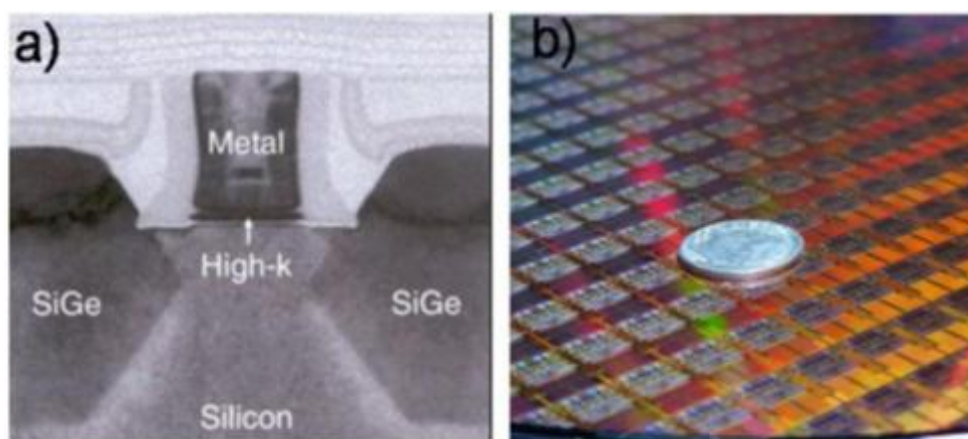

Figure 54: (a) Intel's 45 nm transistor which uses a Hafniun based dielectric. (b) A wafer of the 45 nm transistors photographed with a dime. The processors incorporate 410 million transistors for each dual core chip, and 820 million for each quad core chip. Figures taken from http://www.intel.com/pressroom/kits/45nm/photos.htm.

4.1.1.1. State of the art in graphene FET performance

Before the discovery of graphene, in recent years carbon nanotubes (CNTs) had attracted great interest for their extraordinary mechanical and electrical properties. For their high electron mobility, they are particularly suitable for electronic circuits . The high mobility results from the energy band structure of the graphene coupled with quantization when the graphene sheet is rolled up to form a CNT.

Simulations [155-160] of the electronic properties of Field Effect Transistors (FETs) based on CNTs suggest that they have great potential in future high speed electronic systems. However, in practice, it is difficult to control the chirality of carbon nanotubes and the structures cannot readily be integrated into an electronic system. The chirality is important because the energy bandgap of a semiconducting CNT is a function of it [161].

The advantage of graphene is that it is compatible with the planar technology employed within the semiconductor industry. Like CNTs graphene exhibits high electron mobilities [2,162,163], μ, in excess of 15,000 cm^2/Vs and it can be metallic or semiconducting.

When Novoselov et al. [2] first showed the existence of single layer graphene, they already extensively investigated the field effect behavior besides mobility and magneto-resistance. They fabricated back-gated Hall-bar structures, which were actually the first FETs demonstrated with graphene. Subsequent studies rapidly addressed issues central to FETs in the field of fabrication techniques [92,165], and modeling [166,167].

Graphene field-effect transistors (GFETs) have attracted substantial interest for applicability to high-speed electronics and spintronics and have been extensively used to investigate the electronic transport properties of graphene. In such devices, an electric current is injected/extracted from metallic electrodes (source/drain) through a graphene channel whose conductance is modulated by the electric field from a back- or top-gate, **fig.55**.
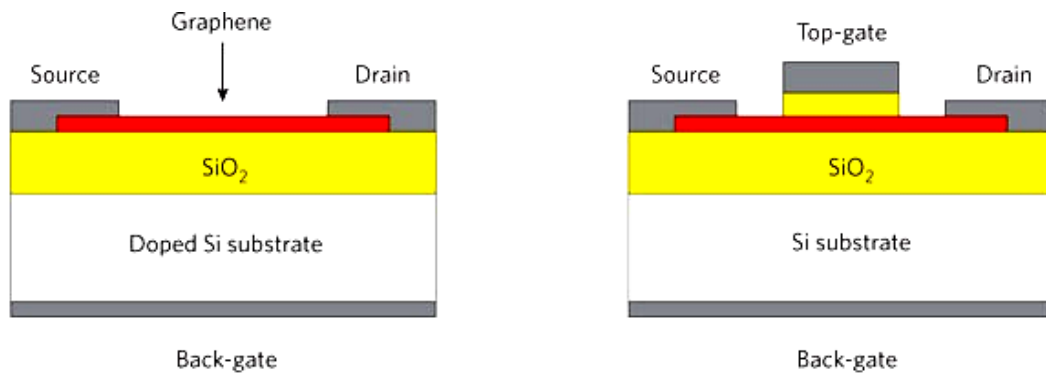
Figure 55. Schematics of different graphene MOSFET types: back-gated MOSFET (left); top-gated MOSFET with a channel of exfoliated graphene or of graphene grown on metal and transferred to a SiO_2-covered Si wafer (right).

The need to ever improve the performances of field effect transistors has made graphene an excellent candidate as channel material in nano-electronic applications. Graphene-based FETs (GFETs) [178] combine an ultra-thin body suitable for aggressive channel length scaling [179], with excellent intrinsic transport properties [180], such as the ability to tune the carrier concentration with electrical gates and a carrier mobility exceeding 10^4 cm^2/Vs at room temperature [2].

Transfer characteristics of GFETs, i.e. the drain-to-source current versus gate voltage, I_{DS}–V_{GS}, curves, typically display a symmetric V-shape, with a hole dominated conductance (p-branch) at lower V_{GS} and electron-type transport at more positive gate voltages (n-branch), separated by a valley corresponding to the charge neutrality condition (also known as the Dirac point) with equal electron and hole concentrations.
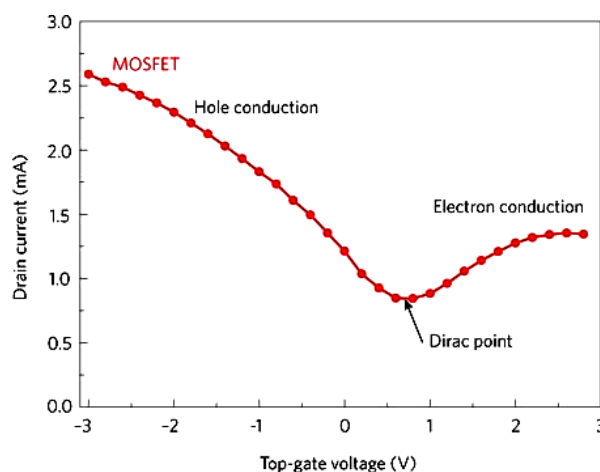

Figure 56. Typical MOSFET transfer characteristics with large-area-graphene channels.Unlike conventional Si MOSFETs, current flows for both positive and negative top-gate voltages[frank].

This V-shape reflects the energy distribution of the density of states, and a conductance dropping to zero at the Dirac point should be expected at low temperature; however, in actual devices, impurities and interaction with the surrounding dielectric introduce local fluctuations in the potential causing a finite density of states at the Dirac point; from the carrier viewpoint, these fluctuations result in localized puddles of electrons and holes which produce an appreciable conductance [192]. Noticeably asymmetric [193-194] and/or anomalously distorted p-branches [195-197] have been reported. The asymmetry between p and n-branches was initially explained in terms of different cross sections of electron/hole scattering from charge impurities [198-199], but more recently the metal/graphene interaction at the contacts has been considered as a key element [194, 200-203].

It has been found in particular that, even in the case of weak adhesion, as with Au, the metal electrodes cause the Fermi level E_F to shift from the conical point in graphene bands, resulting in doping of graphene either with electrons or with holes; the amount of doping can be deduced from the difference of the metal and graphene work functions $(\Phi_M - \Phi_G)$ and from the potential step ΔV due to the metal/graphene chemical interaction $E_F = \Phi_M - \Phi_G - \Delta V$. Depending on the polarity of carriers in the bulk of the graphene channel, charge transfer between metal and graphene leads to p–p, n–n or p–n junctions in the vicinity of the contacts which can cause asymmetry.

For high performance, the choice of materials and fabrication techniques - both for the contacts [181] and the gate dielectrics [182-184] play a very important role.

In particular, the contacts between graphene and metal electrodes can significantly affect the electronic transport and limit or impede the full exploitation of the graphene intrinsic properties [185].

Although ohmic contacts are easily obtained on graphene due to the lack of a bandgap, the very small density-of-state of graphene around the Dirac point may suppress the current injection from the metal contacts, thus resulting in non-negligible contact resistance [185-186]. A high contact resistance limits the total on-state current, and has a detrimental impact on the peak transconductance and on the linearity of current versus gate-voltage characteristic [187], which are defining transistor parameters.

Interface residuals, moistures, trapped charges, etc. may have high impact on the contact resistance and a careful control of the fabrication process is needed. Although in most experimental studies the effect of contact resistance on graphene devices can be suppressed by using a four-probe method, real applications require two-contact devices to achieve high integration. Therefore, understanding and controlling the contact resistance is important from a practical viewpoint other than from the basic physics related to the interface between a 3D metal and a 2D material.

4.2. Contact and edge effects in graphene devices

4.2.1.1. Introduction

The contact resistance and its dependence on fabrication procedure and measurement conditions have not been yet exhaustively studied.

The lowest value of edge specific contact resistivity has been achieved for Pd (230±20 $\Omega \cdot \mu m$ at room temperature [15]); for Ti leads, Ref.[16] quoted 0.8 k$\Omega \cdot \mu m$ independent of the number of graphene layers but sensitive to the gate voltage and controllable by the pressure in the evaporation chamber (lower pressure giving lower resistance). Previous work on Ni leads [17] reported an area specific contact resistivity of few k$\Omega \cdot \mu m^2$ independent from the number of graphene layers. A smaller value, 0.5 k$\Omega \cdot \mu m^2$, was reported in Ref. [13] for devices annealed in a H_2-Ar mixture. Robinson et al [8] propose a method based on O_2 plasma treatment of the graphene prior to metal evaporation to achieve area specific contact resistivity less than 10 $\Omega \cdot \mu m^2$ for any kind of metal, independently of their work function.

Thus, it is still unclear why the reported values of contact resistance R_c span a very broad range.

I present a study of the contact resistance on mono- and bi-layer graphene sheets by fabricating structures suitable for transfer length method (TLM) measurements with Ni

and Ti metals (materials of choice for micro/nanoelectronics industries) without any pre-metal treatment.

Profiting of a relatively high specific contact resistance which results in the main contributor to the total source-drain resistance, I show that the contact resistance is modulated by the back-gate voltage (Vg).

4.2.1.2. Sample preparation and measurement setup

Graphene flakes were obtained by exfoliation with adhesive tape from natural graphite (from NGS Natural graphite GmbH) and transferred to Si/SiO_2 substrates. A short dip (~ 60s) in warm acetone was used to remove glue residuals. The surface of the chip was inspected by optical microscopy **Zeiss Supra 55 VP FESEM** to identify suitable few- and mono-layer graphene flakes according to the color contrast [205].

Mono and bilayer graphene flakes were selected to fabricated TLM structures, each one consisting of parallel leads (often of different length from 1 to 3 μm, see **Fig. 57**) at varying distances along the flake. The Si substrate is covered by a 300 nm thermal SiO_2 that allows easy optical identification of few-layer graphene. The number of layers was further confirmed by Raman spectroscopy and SEM imaging [114]. A grid of reference markers, with a pitch of 100 μm in x and y directions, was used to localize the graphene flakes. The markers were patterned by optical lithography and etched in the SiO_2 with a remaining oxide layer of about 100 nm.

The metal leads were patterned by electron beam lithography and standard lift-off in acetone at room temperature. Depending on the length of the flake, we deposited up to 6 contacts with inter-electrode distance ranging from 1 to 13 μm. The Ti and Ni metal leads were sputtered after keeping the sample in vacuum (10^{-5} mbar) for about 24 hours to possibly remove adsorbates and mixtures from the graphene. The work functions of Ti and Ni (4.33 eV for Ti and 5.01 eV for Ni) are respectively lower and higher than that of graphite (4.5 eV). The Ni and Ti leads were 70 nm thick and were coated with a 50-70 nm Au layer to prevent oxidation and to ease connection to the measurement probes.

SEM images of typical devices are shown in **Fig.57**, on the right the sample is a monolayer contacted with Ni leads, while the sample on the left, is a bilayer with Ti contacts (the bilayer is further exfoliated to become a monolayer under lead 4).
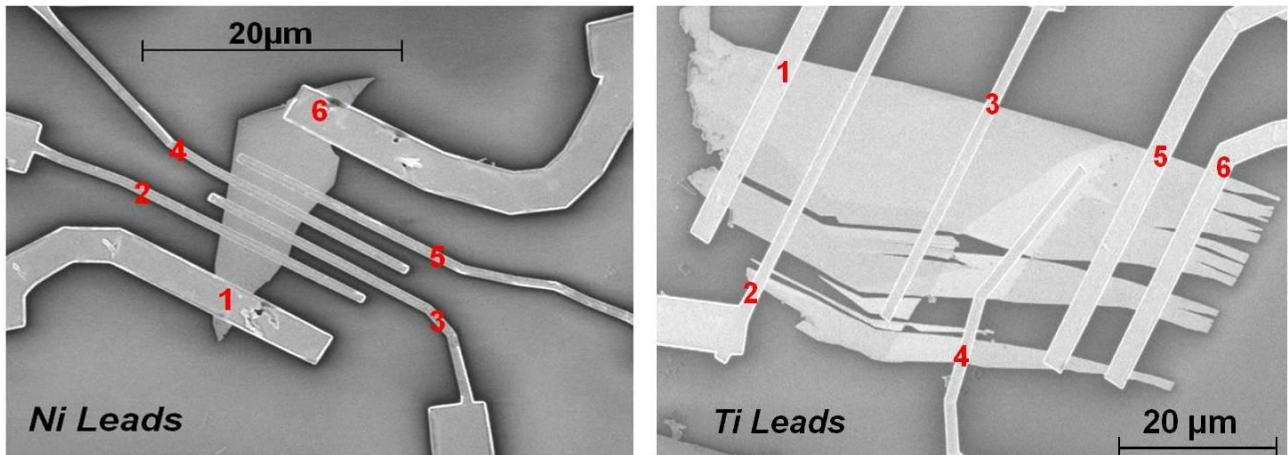

Figure 57. SEM Images of graphene flakes contacted with Ni and Ti Leads

Each couple of leads defines a FET with channel length (*L*) and width (*W*) and with back-gate formed by the highly p-doped silicon substrate. We chose to study devices with back-gate to avoid the risk that multiple-step processing – as necessary for a top gate – would impact the electrical properties of graphene.

Electrical measurements were performed at room temperature under ambient conditions with a Karl Suss probe station connected to a Keithley 4200 Semiconductor Parameter Analyzer. Three terminal measurements were performed, with the Si substrate as the back-gate, and all possible couples of metal electrodes as the source and drain. V_g sweeps, in the interval (-80V, 80V), were performed at constant drain bias (typically 5 to 20 mV). Higher gate voltages were avoided to prevent oxide damage as stresses at $|V_g|$ > 80 systematically caused either gate leakage or complete oxide breakdown.

4.2.1.3. Results and discussion

For an irregularly shaped sample (**Fig. 58**), with contacts of different lengths, d_1 and d_2 and different widths, W_1 and W_2, and at a distance L, the two-probe resistance, R =V/I, is the sum of the channel resistance R_{ch} and the contact resistances R_{c1} and R_{c2}. Despite the current crowding effect at the contacts, it has been proven [186,188] that the contact resistance is characterized by the lead area (the area specific contact resistivity being $\rho_c = R_c Wd$) rather than by the contact width (W) when the contact length (d) is shorter than the transfer length $d_T = (\rho_c/R_{sh})^{1/2}$, i.e. the effective length contributing to the current flow [186], which is typically longer than 1μm (R_{sh} is the sheet resistance of the graphene channel in $\Omega/\square$).
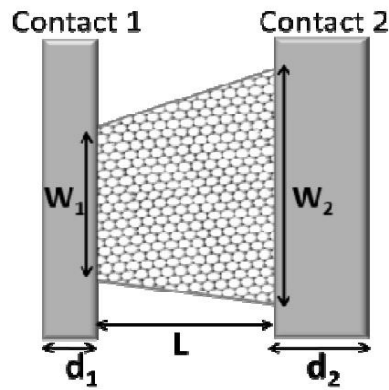

Figure 58. Schematic of a sample with varying channel width and with contacts of different lengths

Since the typical length of most of our contacts is of the order of 1μm, we decided to consider the area conduction rather than the edge conduction in our analysis. The total resistance of a trapezoidal graphene channel (see **Fig. 58**) can be written as:

$$R = R_{c1} + R_{c2} + R_{ch} \tag{4.1}$$

$$= \frac{\rho_{c1}}{W_1 d_1} + \frac{\rho_{c2}}{W_2 d_2} + R_{sh} \int_0^L \frac{dx}{W_1 + \frac{(W_2 - W_1)x}{L}} \tag{4.2}$$

$$= \frac{\rho_{c1}}{W_1 d_1} + \frac{\rho_{c2}}{W_2 d_2} + R_{sh} \frac{ln\left(\frac{W_2}{W_1}\right)}{W_2 - W_1} \tag{4.3}$$

If the contacts are made of the same metal, we can reasonably assume that $\rho_{c1} = \rho_{c2} = \rho_c$ and equation:

$$R_{eff} = \rho_{c+} \rho_{sh,eff} \frac{ln(W_2/W_1)}{W_2 - W_1} L \tag{4.4}$$

Where:

$$R_{eff} = R \left(\frac{1}{W_1 d_1} + \frac{1}{W_2 d_2}\right)^{-1} \tag{4.5}$$

and:

$$\rho_{sh,eff} = \rho_{sh} \left(\frac{1}{W_1 d_1} + \frac{1}{W_2 d_2}\right)^{-1} \tag{4.6}$$

Equation (4.4) shows that the specific contact resistivity ρ_c can be evaluated as the intercept of a plot of R_{eff} versus L for every couple of electrodes (TLM method).

Examples are given in **Figs. 59a)** and **59 b)**, where all the working combinations of electrodes were considered (some electrodes resulted in opens, some others were shorted by graphite flakes randomly present on the substrate). R_{eff} was obtained from the I-V curves (output characteristics) measured at given back-gate voltages V_g for all combinations on a flake.
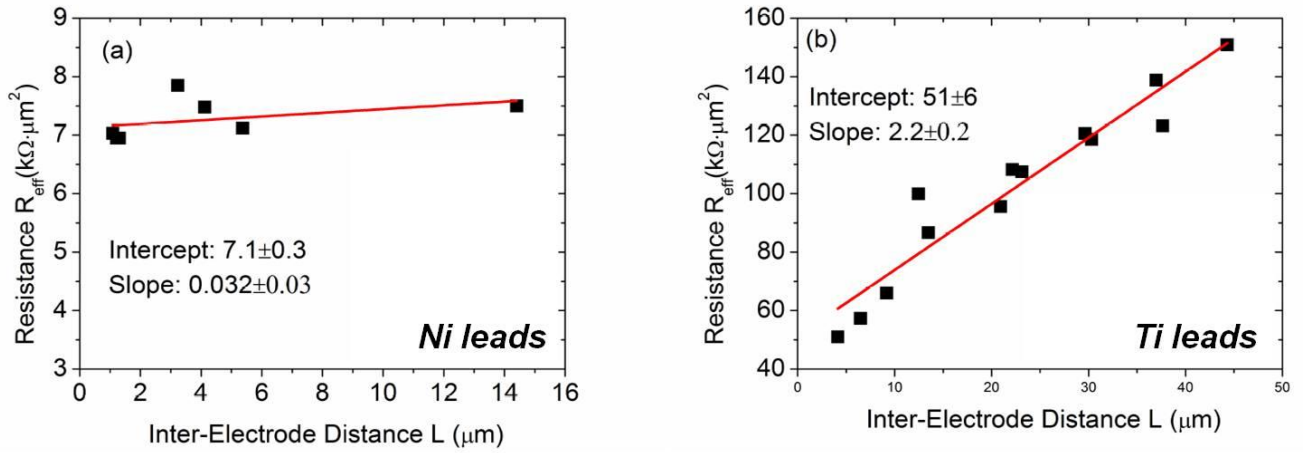
Figure 59. a), b) TLM plot of $R_{eff}(L)$ at a given Vg for the flakes in figure 57 respectively.

The output characteristics showed a linear behavior both for Ni and Ti contacts (an example is given in **Fig 60** for Ni contacts), evidencing that enough good contact is established between graphene and metals.
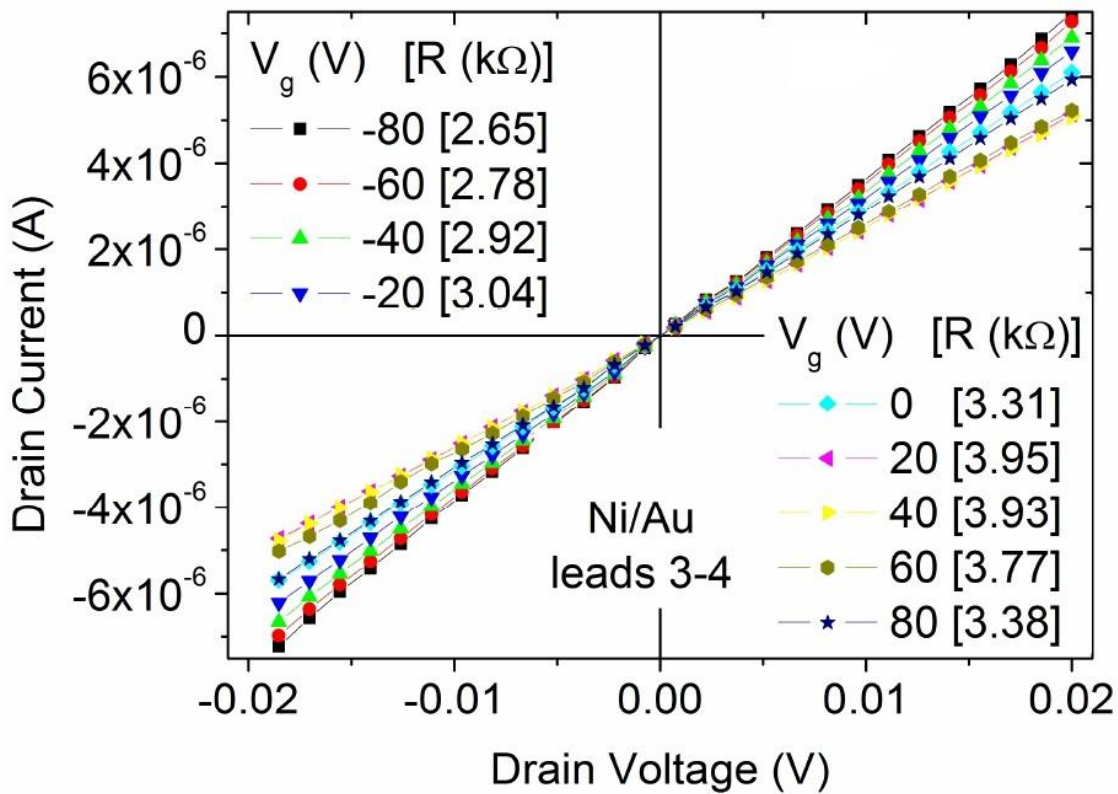

Figure 60. Output characteristics of transistors of Fig.57 using Ni-leads 3 and 4 as source and drain.

Figures 61 a) and **61 b)** show the dependence of ρ_c on $\mathbf{V_g}$ - both for Ni and Ti contacts- as extracted by TLM method; ρ_c is compared to the measured $R_{\textit{eff}}(\mathbf{V_g})$ for the couple of leads which had the low resistance. These figures clearly demonstrate that the specific contact resistivity is modulated by the back-gate voltage. Furthermore, they show that the specific contact resistivity dependence on the back-gate voltage has the same qualitative behavior as the total source-to-drain resistance (curve $R_{\textit{eff}}(V_g)$), with a peak around the Dirac point ($V_{gD} \approx 20 \div 40V$) and a decrease when the channel is field-doped by the back gate. This result agrees with the recent study in Ref. [189] on Pd contacted graphene transistors and confirms the gate modulation of the Fermi level relative to the energy at the Dirac point for the graphene underneath the metal [190].
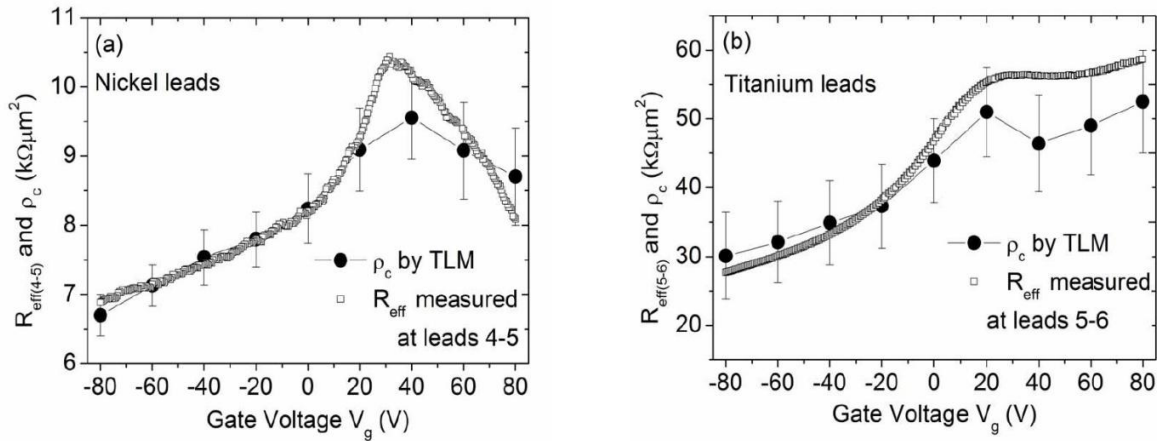

Figure 61. Contact resistivity ϱ_c and effective resistance $R_{\textit{eff}}$ as function of the back gate potential Vg for Ni and Ti contacts.

Furthermore, the superposition of the two curves $\rho_c(Vg)$ and $R_{\textit{eff}}(\mathbf{V_g})$ in the plots of **Fig.61** shows that the contact resistance is a major contributor to the resistance of the TLM transistors.

The minimum values of $\rho_c \sim 7$ k$\Omega \cdot \mu m^2$ and ~ 30 k$\Omega \cdot \mu m^2$ we measured for Ni and Ti, respectively, are higher than those achieved by other groups; this difference can be ascribed to the fact that we did not make any pre-metal deposition treatment or any post-fabrication annealing of the device. Moreover, we deposited metal by sputtering and not by evaporation that usually results in lower contact resistance [181].

Additionally, we cannot exclude that some oxidation took place at contacts for oxygen diffusion and that we have somehow overestimated the effective contact area.

The flake of **Fig 57** with Ti leads**,** allowed us to make a comparison between R_{eff} when both leads are on bilayer graphene and in the case where one of the contacts is on a single layer (lead 4). No significant difference was observed (for example, R_{eff} =42 kΩ μm^2 for leads 3-4 and, R_{eff} =44 kΩ μm^2 for leads 3-5 at Vg = -80V), thus, confirming the independence of the contact resistance on the number of graphene layers reported in [191].

In conclusion, I reported the area specific contact resistivity of Ti and Ni contacted graphene transistors. Resistivity is modulated by the back gate, with the same dependence as the channel resistance, i.e. a peak at the Dirac point and an asymmetric decrease for increasing $|Vg - V_{gD}|$.

4.3. Origin of anomalies in GFETs transfer characteristics

4.3.1.1. Introduction

Measurements of transfer characteristics of back-gated field effect transistors were performed on all our devices.

I study the source-drain conductance versus back-gate voltage, $G\text{-}V_g$ curves, and for the first time we discuss the observation of hysteresis as well as double dips on GFETs on Si/SiO$_2$ substrate with Cr/Au contacted long channel (10μm) [38], never presented before in others works.

Charge trapped in the surrounding dielectric and in particular in silanol groups at the SiO$_2$ surface is at the origin of the hysteresis; while, the gradient of carriers along the channel caused by electron transfer from the graphene to the Au/Cr contacts and the band shift induced by the back gate voltage and the SiO$_2$-trapped charge are proposed to account for the double dip feature.

We show in particular that p–n junctions are spontaneously formed by charge transfer between the graphene and the electrodes and that a double Dirac point can be achieved when low-resistivity contacts are fabricated. We further clarify the role of charge stored at the SiO_2 interface in the formation of the double dip and we propose partial charge pinning at the contacts to explain the current saturation observed at high back-gate voltages.

We finally show that the hysteresis, enhanced by a double dip, can conveniently be exploited to build graphene-based memory devices.

The peculiar appearance of a double dip, it has been observed and studied also on the previous devices (mono and bilayer graphene flakes contacted with Ni and Ti leads), that I report in a due time.

We explain this feature in both cases by assuming that the graphene under the contacts is locally doped by the metal electrodes [18-19].

A double dip in the transfer characteristic has been also discussed by Barraza-Lopez et al [205] with a first-principles study of the conductance through graphene suspended between Al contacts. They show that the charge transfer at the leads and into the freestanding section gives rise to an electron–hole asymmetry in the conductance; more importantly they suggest that, for sufficiently long junctions, this charge transfer induces two conductance minima at the energies of the two Dirac points of the suspended and clamped regions, respectively.

4.3.1.2. Transfer Characteristics in GFETS with Cr/Au contacts

Graphene Transistors with metal contacts of Cr/Au (5 nm/150 nm, with Cr as adhesion layer), were fabricated following the same procedure of (4.2.1.2).

Metal were sputtered after electron beam lithography and structured by lift-off on selected single-layer graphene flakes. Soon after, some devices were covered by 250 nm thick polymethyl methacrylate (PMMA). PMMA was spin-coated on the whole chip and

cross-linked, and thus made resistant to acetone etch, by exposure to 30 keV electrons at a dose of 3×10^4 μC cm^{-2} on the device area.

Figures 62 (a) and (b) show the layout and the SEM top view of a typical device before PMMA coverage, respectively.

All the measurements were performed in air and at room temperature using an HP4140B semiconductor parameter analyzer.
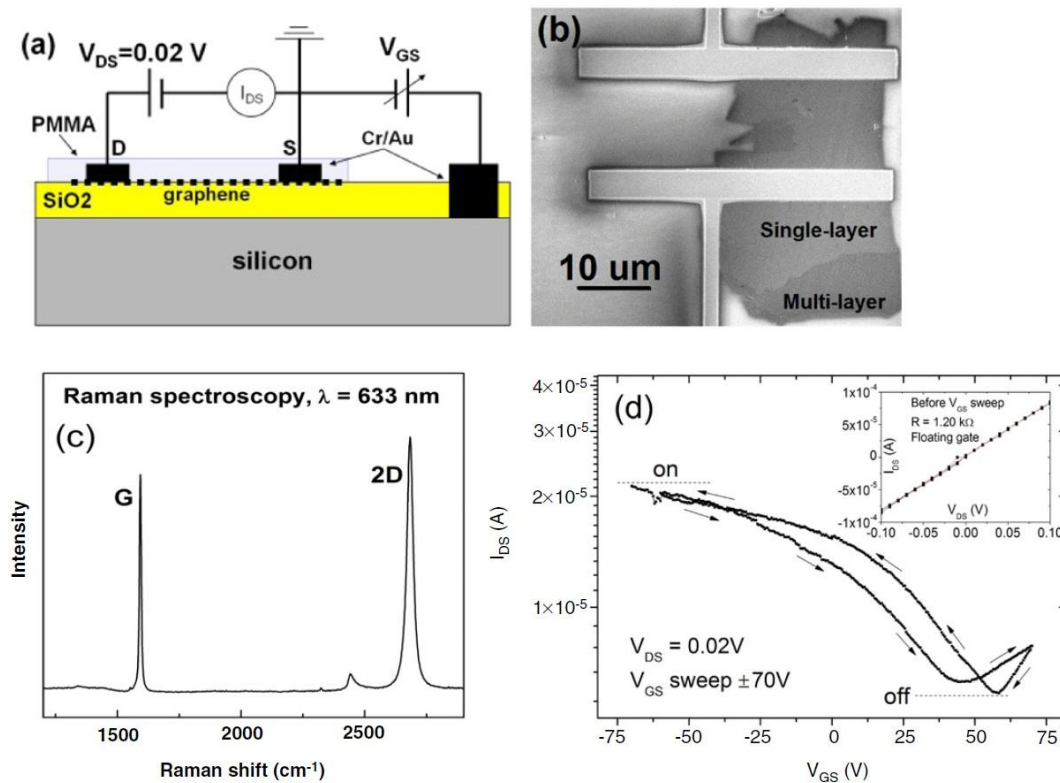

Figure 62. (a) Cross section of the device layout and electrical measurement setup. (b) SEM image of the graphene transistor with Cr/Au electrodes (source/drain). The channel width is $W \approx 23$ μm and the channel length is $L \approx 12$ μm. The effective device has been contacted such that it involves only the single-layer part of a multi-layer graphene flake. (c) Raman spectrum showing 2D and G peaks typical of single-layer graphene. (d) Transfer characteristic I_{DS}–V_{GS} of the device; the inset shows the source-to-drain current measured with floating back-gate.

Figure 62(d) shows the transfer characteristic of the device. A minimum I_{DS}, i.e. a lower conductance, corresponding to the charge neutrality point, is observed at V^*_{GS} $\approx$ 60 (45) V in an initial reverse (forward) V_{GS} sweep with an amplitude of 70 V; the low

on/off ratio of about 5 is expected for a graphene flake with low or zero bandgap. A positive charge neutrality point V^*_{GS} indicates that the graphene is unintentionally highly p-doped. We observed this behavior on all fabricated GFETs; indeed, the Dirac point was often located behind the sweeping upper limit of 80 V, especially for devices not covered by PMMA.

The formation of weak C–O bonds between graphene and SiO_2 has been proven [206-207] to support p-type conductivity in graphene by transfer of charge from the carbon in graphene to the oxygen of the SiO_2. This increases the hole concentration in graphene and favors the formation of p-type conductivity at an unbiased gate, thus forward shifting the Dirac point.

Moreover, molecules adsorbed on the surface of the channel or at the graphene/SiO_2 interface during the fabrication process, consisting mainly of hydrocarbons, carbon dioxide, oxygen and water, are known as a further cause of the forward shift of the charge neutrality point. Indeed, for H_2O [208], CO_2 and O_2 [209], it has been shown that there is an electron transfer from graphene to the adsorbed molecules, which results in p doping for graphene. The use of PMMA as coverage of our devices prevents further adsorption and helps to maintain the neutrality point within the swept V_{GS} range. This enabled us to measure and study both the p- and part of the n-branch of the transfer characteristic. A second important feature observed in the measured I_{DS}–V_{GS} curve of **figure 62 (d)** is a clear hysteresis between the forward and reverse sweeps. Several recent reports have shown a strong hysteretic behavior in the field-effect characteristics of Si/SiO2 supported GFETs. In analogy to single-walled carbon-nanotube-based field-effect transistors [210, 211], gate hysteresis has been attributed mainly to charge trapping in silanol groups (Si–OH) with surface-bound H_2O molecules facilitating the process of charge transfer and trapping [212, 213]. Consequently the concentration, distribution and reactivity of the silanol groups of the underlying SiO_2 play a decisive role in the transfer characteristics of a GFET. A high concentration of silanol groups makes the SiO_2 surface hydrophilic (in general dipolar molecules can easily attach to SiOH), but special treatment can turn this surface hydrophobic; indeed, nearly hysteresis free

GFETs have been achieved on SiO_2/Si substrates covered by a thin hydrophobic self-assembled organic layer of HMDS solution (hexamethyldisilazane/acetone 1:1) [214]. Thermal annealing or vacuum pumping can also help to reduce hysteresis [203]. Nevertheless, we decided not to apply any treatment or annealing (other than the electrical one) to avoid the risk of introducing unwanted damage or stresses. Charges can be trapped in the PMMA as well; nevertheless, since the back-gate field is screened by the graphene layer, tunneling between the graphene channel and the top PMMA layer is suppressed with respect to tunneling between graphene and SiO_2 during V_{GS} sweeps.

In **fig.63** we report the evolution of transfer characteristics for successive V_{GS} sweeps, acting as electrical annealing.
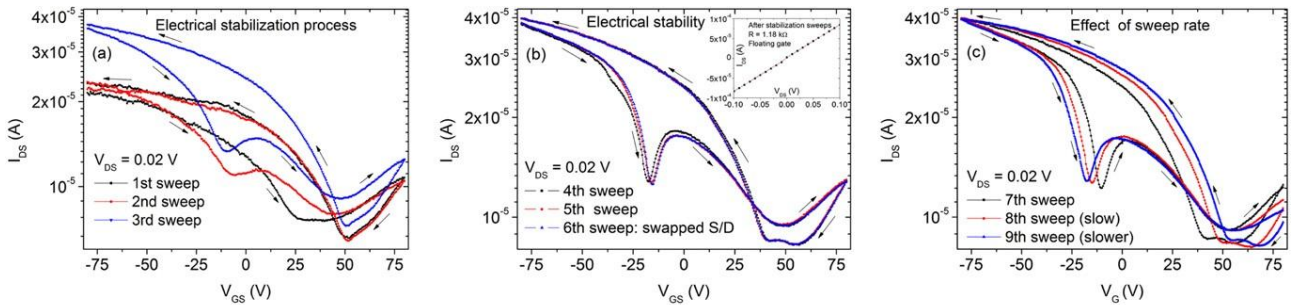

Figure 63. Transfer characteristics of the GFET of figure 58: (a) during the stabilization process and (b) after stabilization (inset: I_{DS}–V_{DS} for floating back-gate after stabilization). The stabilization results in higher current and in the appearance of a double dip. (c) Effect of the sweeping rate.

Remarkably, **fig. 63(a)** shows that the electrical cycles produce an increase of the current and the appearance of a double Dirac point, i.e. of two conductance minima. Further sweeps demonstrate the stabilization of the device (**fig.63(b)**). Swapping the drain and source has no effect. Two clear dips appear both in the reverse (where they are closer and less pronounced) and in the forward V_{GS} sweep. **Fig.63(c)** shows that a slower sweeping rate, which favors charge injection and trapping at the SiO_2 surface, widens the hysteresis loop. The electrical stabilization, due to current self-annealing, is mainly the result of graphene–electrode interface modifications, which reduce and stabilize the contact resistance; we exclude bulk channel changes since the PMMA layer prevents removal of contaminants from its surface [214] that may vary its conductance.

The contact resistivity [215], $\varrho_C=RW \approx 5$ kΩ μm (W is the width of the channel), is on the low side of the range usually reported for Cr/Au-contacted GFETs $(2 \times 10^3$ Ω μm $\leq \varrho_C \leq 10^6$ Ω μm) [217]; ϱ_C is estimated at $V_{GS}= -80$ V when the source-to-drain resistance is dominated by the contacts, the graphene bulk channel being at its maximum conductance. A further confirmation of the good contacts stems from the calculation of the mobility [217]. Despite the top coverage, which may affect the mobility [218] for the participation of π-orbitals in the van der Waals bonds to the PMMA, a hole mobility of ≈ 3000 cm^2 V^{-1} s^{-1}, thus exceeding the universal mobility of silicon, is achieved in our devices; this value is consistent with measurements performed on devices of comparable geometry where metals with better chemisorption to graphene have been used [219, 220]. The mobility μ has been estimated from the simple formula $\mu = \dfrac{dI_{DS}}{dV_{DS}} \dfrac{L}{W} \dfrac{d}{\varepsilon} \dfrac{1}{V_{DS}}$ where L and W are the channel length and width, d the SiO$_2$ thickness, ε its dielectric constant, dI_{DS}/dV_{GS} the transconductance calculated from the linear region of the I_{DS}–V_{GS} curves at the left side of the Dirac point. We emphasize that the double Dirac point is obtained while keeping the drain bias very low (20 mV). This suggests that a second dip does not necessarily appear as a result of charge trapped in the vicinity of the drain at the graphene/SiO$_2$ interface during a drain stress [221].

In the following we suggest that charge transfer between the graphene and the metal contacts and charge trapping at the SiO$_2$/graphene interface, as well as partial pinning of the Fermi level at the contacts, can fully explain the behavior of the I_{DS}–V_{GS} loop and, in particular, account for the double Dirac point. We demonstrate that the double dip is the result of a different Fermi level alignment within the graphene double-cone at the contacts with respect to the bulk channel; the Fermi level within the band diagrams is shifted by the back-gate voltage and is influenced by the charge trapped at the SiO2/graphene interface.

Due to different work functions (4.6 eV for Cr, 5.1 eV for Au and 4.5 eV for graphene [222]) electrons transfer from the graphene to the metal electrodes, thus forming a doping gradient from the contacts to the bulk channel. Underneath and close to the electrodes, the graphene is more p-doped than in the channel [200]. The doping of the

graphene by the contacts is not limited to only underneath the metal electrodes but extends for 0.2–0.3 μm [223] or longer [224] in the inner channel, since the graphene, having zero density of states at the Dirac point, is not able to absorb all the transferred charge at the interface. While charge-density pinning (i.e. gate uncontrollability of charge-density at the metal contacts) could occur at Au/graphene contacts, reactive materials have been proven to lead to charge depinning [196], especially when an oxide layer is formed at the graphene/metal interface. We assume here partial charge pinning with charge at the contacts controlled by the back-gate up to a certain limit, over which the charge cannot be increased; this means that the Fermi energy at the contacts can vary only within a limited range from the conical point of the graphene bands. This assumption can be seen as a consequence of the low contact resistance which makes the potential of the graphene at the contacts be anchored to the bias of source and drain; in such a case, the field of the back-gate is expected to affect mainly the carrier concentration in the bulk graphene channel. We will also show that the assumption of partial pinning leads to a good fit of the I_{DS}– V_{GS} curves on the whole V_{GS} range.

The effect of charge transfer at the contacts can be taken into account by shifting the energy band diagram (double cone) of the graphene upward with respect to that in the bulk channel for unbiased V_{GS} (**fig.64**).

The application of the back-gate voltage moves the Fermi level with respect to the double-cone, determining different conduction regions between source and drain. At $V_{GS} \geq 80$ V, n-type conduction takes place everywhere, thus giving a high conductance (point 1 in **fig. 64**).
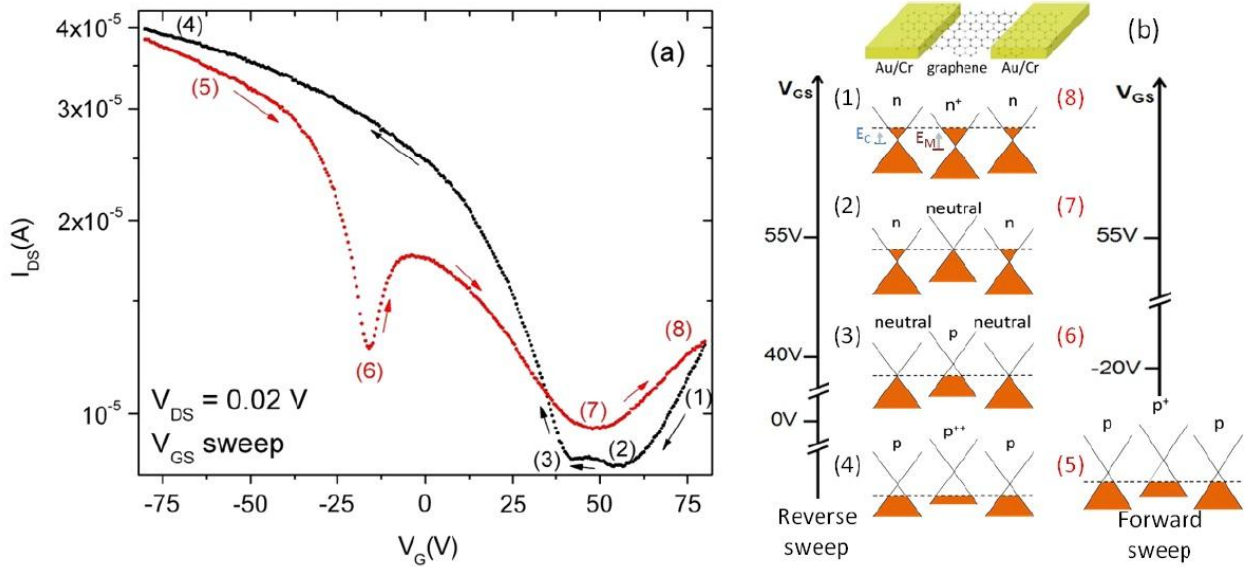
Figure 64. (a) Transfer characteristic of a GFET with hysteresis and a double dip. (b) Band diagrams of the graphene between the source and the drain and position of the Fermi level for different V_{GS}. For a floating gate, the double-cone, close to the contacts, is shifted upward with respect to the one in the bulk channel to account for the p-doping due to transfer of electrons from graphene to the Cr/Au leads.

The source-to-drain channel appears as an n/n+/n structure (graphene doping of source/channel/drain regions). When lowering V_{GS} (reverse sweep) the electrons move away through contacts, so a charge neutrality condition, i.e. a first Dirac point, is reached in the channel before that at the contact regions (where graphene stays n-doped for longer). Consequently, the n/n+/n junction gradually evolves into an n/neutral/n structure. The resistance associated with a neutral/n junction is larger than that of an equivalent n/n+ (or sharp n/p) junction, as can be easily understood within a diffusive carrier transport model, where the resistance is simply obtained by integrating the local resistivity along the length of the junction. Therefore this condition results in a conductance minimum which corresponds to the first valley (point 2) in the transfer characteristic. A further decrease in V_{GS} generates a p-type conduction in the inner channel, giving rise to an n−/p/n− structure, with slightly increased conductance. When the graphene at the contacts reaches the charge neutrality point (neutral/p/neutral junction) a second Dirac point (point 3) is observed.

The separation $\Delta V_{GS} \approx 10$ V of these two dips is related to the initial carrier concentration difference between the channel and the contact regions, i.e. to $\Delta E_{MC} = E_M - E_C$ at the beginning of the sweep (here E_M and E_C are the Fermi levels of graphene with respect to the local neutrality point in the channel and at the metal contacts, respectively). Going to more negative V_{GS} a low-resistance p-channel (p/p++/p structure) is formed. The partial pinning at the contacts avoids a further increase of the absolute value of E_C at high negative V_{GS}, thus causing a saturation of the conductance.

On the other hand, the high negative voltage applied during the reverse sweep causes positive charge to be stored at the SiO_2/graphene interface, which, as already said, is at the origin of the leftward shift of the transfer characteristic during the following forward sweep, i.e. of the hysteresis. This trapped charge acts as a reduction of the overall p-doping and can be taken into account with a down-shift of the graphene bands (configuration 5). During the forward sweep the p doping of the graphene is neutralized by attracting electrons from the contacts and a neutral condition is soon reached at the contacts, thus resulting in a first Dirac point (point 6 at $V_{GS} \approx -18$ V in **fig.64(a)**). Further increase of V_{GS} creates a second dip (at $V_{GS} \approx 48$ V) when neutrality is reached in the bulk channel (point 7). The second Dirac point happens at a V_{GS} value slightly below the one observed during the reverse sweep as an effect of the charge stored at the SiO_2/graphene interface; finally a low-conductance n/n+/n structure (point 8) is formed again. The $\Delta V_{GS} \approx 65$ V separation between the two dips in the forward sweep is increased with respect to the previous $\Delta V_{GS} \approx 10$ V since the downward band shift created by the SiO_2 trapped charge and the injection of electrons from the contacts greatly favors the appearance of a Dirac point in the contact regions. The position of this point, being related to the SiO_2 trapped charge, depends also on the maximum negative voltage applied during the previous reverse sweep.

The hysteresis observed in carbon-nanotubes-based transistors has been exploited to build memory devices [211, 225, 226]. Similarly, here, the two values of the current at a given gate voltage can be considered as the two logic levels (on and off state) of a memory device; positive or negative V_{GS} pulses can be used to switch between these two states to implement the write and erase operations. **Fig.65** is a proof of the concept, where reading is performed at $V_{GS} = 0$ and ± 80 V pulses are used for write and erase. The programming pulses are of course enormous for practical applications; nevertheless, with proper treatment of the SiO_2/Si or by ionic screening [228], it could be possible, in principle, to obtain transfer characteristics with the deeper dip around $V_{GS} = 0$ and accordingly considerably reduce the operating voltages. For practical technological applications, the same device could be implemented with a topgate, thus leading to significantly lower write/erase voltages.
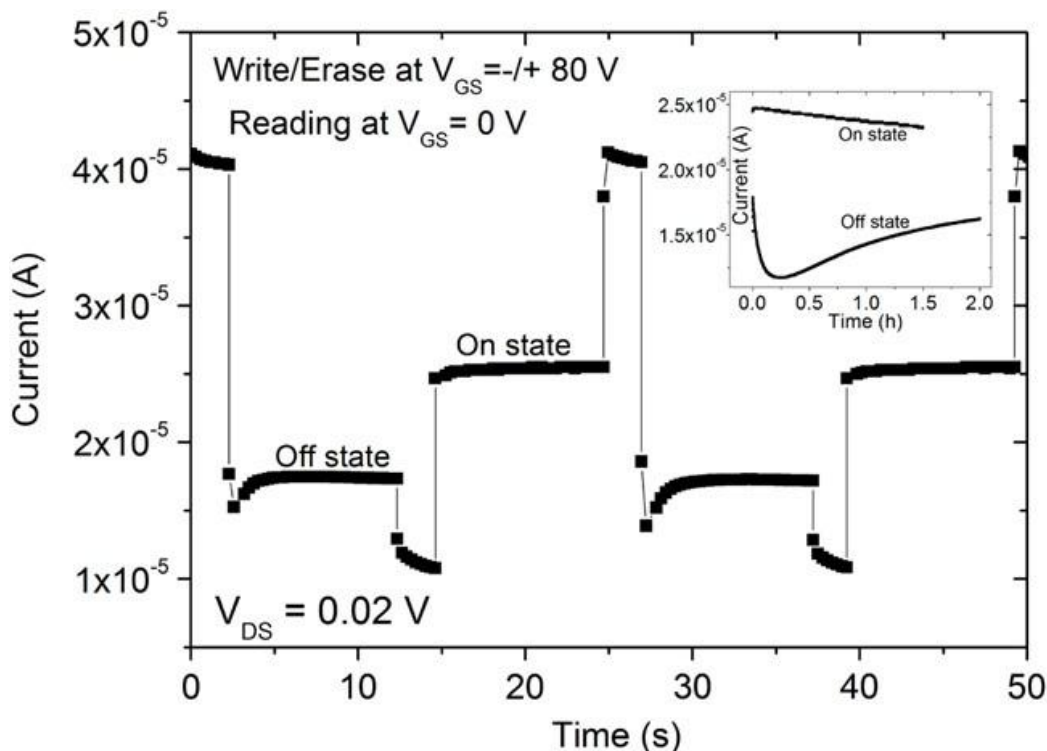

Figure 65. A GFET used as a memory device. A $V_{GS} = 80$ V pulse sets the device to its off state, while a $V_{GS} = -80$ V pulse switches it to the on state. Reading is performed at $V_{GS} = 0$ V. The on and off states constitute the two logic levels of a memory device. The inset in the figure shows that those states stay separated for a time of at least 2 h.

4.3.1.3. Transfer Characteristics in GFETS with Ni, Ti contacts

Fig.66 shows an anomaly in the conductance curves, appearing as a double-dip feature, both for Ni and for Ti (**Figs. 66a**), even though in the case of Ti, the limit on the back-gate sweeping range did not allow the full characterization of this phenomenon.
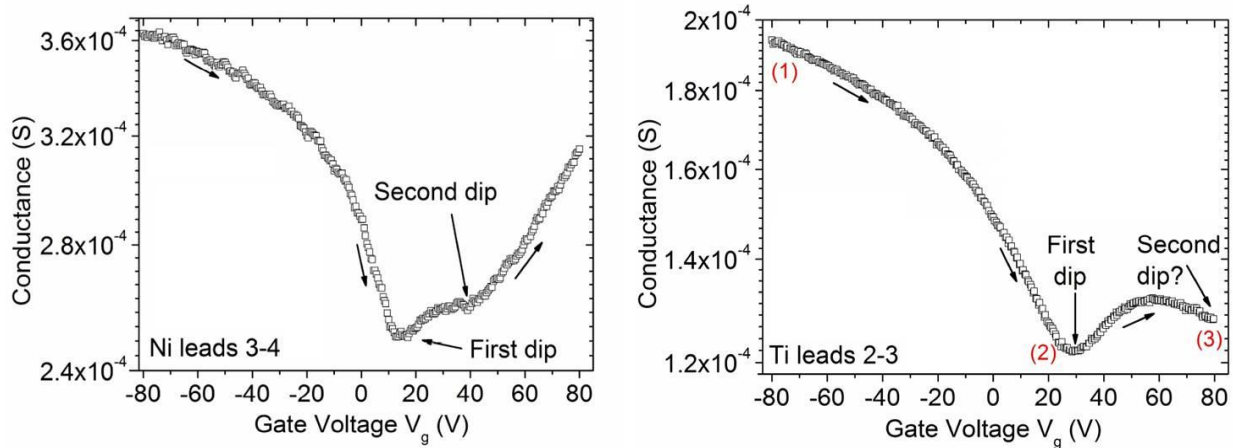

Figure 66: Appearance of a double dip in the conductance versus back-gate voltage curves both for Ni and Ti contacts.

We proved that metal doping and charge trapping at SiO_2/graphene interface, as well as partial pinning of the Fermi level at contacts, can fully explain the behavior of a whole G-V_G loops.

Here, we qualitatively summarize the key points of our model with the help of **Fig. 64b)** adapted for a device with Ti leads for the forward Vg sweep.

The electron transfer from Ti to graphene, due to the work function mismatch, makes graphene less p-doped underneath the contacts than in the channel. The application of the back-gate voltage moves the Fermi level in the graphene band diagrams, determining different conduction regions between source and drain.

At V_G= -80V (point 1 in **figures 66(right)**), p-type conduction takes place everywhere, thus giving a high conductance $p/p^+/p$ structure (source/channel/drain graphene doping). While rising V_G to positive values, electrons are attracted to the channel and a charge neutrality condition is reached at the contacts, where the graphene is less p-doped; a low conductance neutral/p/neutral structure is achieved, which corresponds to

the first valley in the G-V_G curve (point 2). A further increase in V_G gradually reduces the p-doping in the channel and increases the n-doping at contacts creating an even less conductive $n^-/p^-/n^-$ structure (point 3). A further increase in V_G leads to the formation of a low-resistance n-type structure (point 4). With Ni leads a similar behavior is obtained with the difference that graphene under the contacts is now p-doped at and a neutrality condition is first reached in the channel during the forward V_G, making the first minimum deeper than the second one.

Fig. 67 shows that lowering the temperature leads to a slight reduction of the source-to-drain conductance that makes the two minima in the G-V_G curve unresolved. At 210 K the measured conductance curve at the dips is broadened with respect to the expected V-shape.
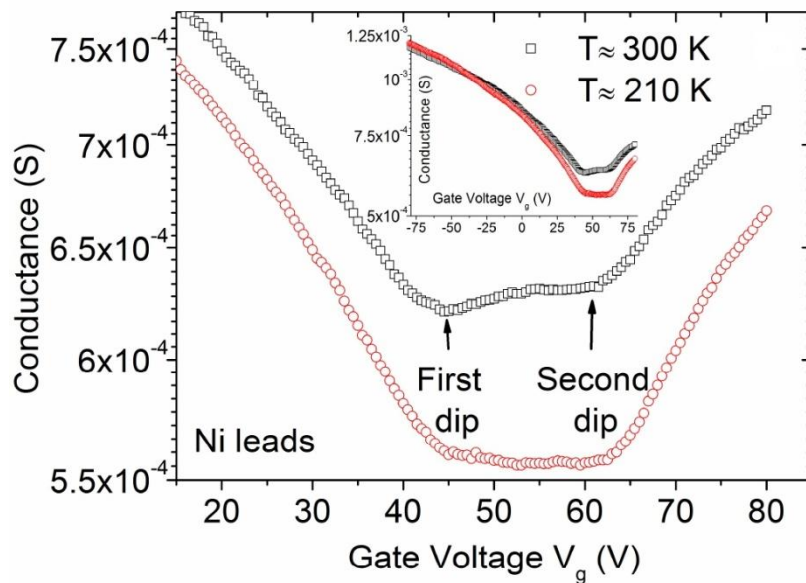

Figure 67. Conductance versus back-gate voltage curves both for Ni for two values of temperature

The double dip mechanism described, works for large-channel devices (channel length greater than 7-10 μm), while in smaller GFET devices double-dip-like structures in conductance curves should be produced by the strong proximity effects coming from the Ni-graphene interaction.

4.4. Conclusion

In conclusion, we have clarified the nature of the double dip often observed in the p-branch of the transfer characteristic of a GFET. We have shown that it is related to charge transfer between the graphene and the metal contact and that it is enhanced by the hysteresis provoked by charge storage at the graphene/SiO_2 interface. Elucidation of the origin of such an anomaly is of technological importance since the observed distortion indicates a deterioration of the gate voltage response of the device, i.e. a decrease in the field modulation of the channel conductance.

Chapter 5
Field Emission from Graphene

5.1. Introduction

Field-emission is a quantum tunneling phenomenon in which electrons pass from an emitting material (cathode) to an anode through a vacuum barrier by effect of high electric field. For a given material, cathodes with higher aspect ratios and sharper edges produce higher FE currents. For this reason, nanostructures are considered promising for commercial applications as flat-panel displays, vacuum electronics, microwave power tubes, electron sources, etc. Graphene has a very high aspect ratio (thickness to lateral size ratio) and a dramatically enhanced local electric field is expected at its edges; it shares many similar or even superior properties as carbon nanotubes [230-231] and, as CNTs, has high potentiality for FE applications [232-234]. In this thesis I have performed some work on graphene, FE properties using mono and bi layers FE from graphene has been realized in a scanning electron microscope equipped with two nanomanipulators enabling a precise probe positioning. Moreover the use of a Keithley 4200-Semiconductor Characterization System, operating as source-measurement unit gives access to high resolution measurements, with current leakage of the order of few pico-Ampere.

5.2. Theory of Field Emission

Field emission - also called Fowler-Nordheim tunneling [235]- is the process whereby electrons tunnel through a barrier in the presence of a high electric field.

Fowler and Nordheim developed their theory based on the calculated number of electrons impinging on the surface from the bulk, the tunneling of electrons through the

surface potential barrier, and solving the Schrödinger equation to find the fraction of electrons that penetrate the barrier.

Upon integrating the product of the number of electrons arriving at the surface from the bulk and the tunneling probability over all energies, they obtained a formula for the current density (J) produced by a given electric field (E) is described by the equation:

$$ J = \frac{A\beta^2 E^2}{\Phi} exp\left(-\frac{B\Phi^{\frac{3}{2}}}{\beta E}\right), \quad I = S \cdot J, \quad E = \frac{V}{d} \tag{5.1} $$

where A and B are constants, (A = $1.54\cdot10^{-6}$ A eV V^{-2}, B=$6.83\cdot 10^{7}$ eV$^{-3/2}$ V cm^{-1}), β is the field enhancement factor at the emitting surface, d is the distance between the sample and the anode, ϕ is the work function of the emitting materials, I is the emission current, S the emitting area and V the applied voltage.

According to (5.1), the FN behavior predicts a straight line when plotting $\ln(I/V^2)$ versus $1/V$. However, to justify recent observations of nonlinear FN plots for graphene, it has been proposed that FE processes can undergo a low-to-high field regime transition that could provoke an up-bending of the FN plot, suggesting the necessity of introducing a more general relation:

$$ ln\left(\frac{I}{E^\alpha}\right) \approx \frac{1}{E^\beta} \tag{5.2} $$

5.3. Device fabrication and measurements set up

Single- and few-layer graphene sheets were prepared by mechanical exfoliation of highly ordered pyrolytic graphite and transferred by scotch-tape method on SiO$_2$ layer thermally grown on p-type Si substrate. The thickness of the SiO$_2$ layer was chosen to ≈300 nm to make the single and few-layer graphene clearly visible and distinguishable under optical microscope, which was used for a first localization of the flakes in the reference frame of a regularly 100 μm spaced grid of Au crosses deposited on the substrate by conventional lithography **Fig.70a**.

FE measurements were done in a SEM chamber equipped with two metallic nanomanipulators.
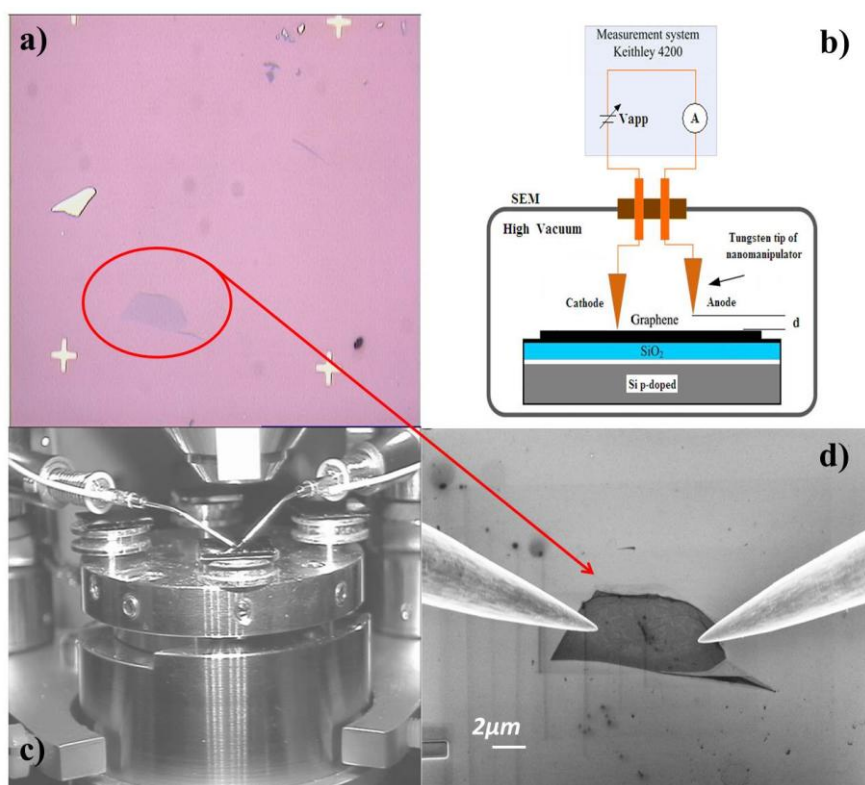

Figure 68. (a) Optical image of a graphene flake at 50x magnification; (b) Schematic view of the experimental setup using a SMU interconnected to nanomanipulators in SEM chamber. (c) Photograph of the inner SEM chamber, d) SEM image of graphene flake contacted by the nanomanipulators.

The two nanomanipulators had tungsten tips with curvature radius <100 nm. The SEM chamber was kept to a pressure of 10^{-6} Torr and at room temperature. The tips, one in contact with graphene and the second at a varying distance from it, were used as the cathode and the anode, respectively. Vacuum feed-through connected the two nanoprobes to a source-measurement unit. In **Fig.68b)** we show a scheme of the measurement setup while a real image of the inner part of SEM chamber is reported in **Fig.68c)**, with the tips pointing to the sample. As measurement procedure, we first imaged a graphene flake in the SEM profiting from a previous localization with respect

to the Au markers under optical microscope. Then we gently contacted the flake with both nanoprobes, carefully avoiding breakage of the graphene lattice, and we measured its I–V characteristics.

5.4. Results and analysis

The series resistance of the measurement loop obtained with the two tips shorted was 3Ω. Once the tips were approached on a graphene flake, the measured resistance was observed to decrease from $M\Omega$ till $k\Omega$ range for successive voltage sweeps which acted as electrical conditioning, appreciably improving the quality of the nanoprobe-graphene contacts. **Fig.69** shows an example of I–V curves when both probes were in contact with a graphene flake. Sweep 1 was reproducibly measured by limiting the maximum current to 50 μA; as soon as we forced higher current (200 μA) through the contacts, the circuit resistance was sensibly reduced (sweep 2); the third sweep is measured after electrical stress with 300 μA current. Higher current values were avoided in order to prevent graphene flake breakage. **Fig. 69** demonstrates that increasing the maximum current improves the contacts, thus lowering the resistance and making the current more stable.
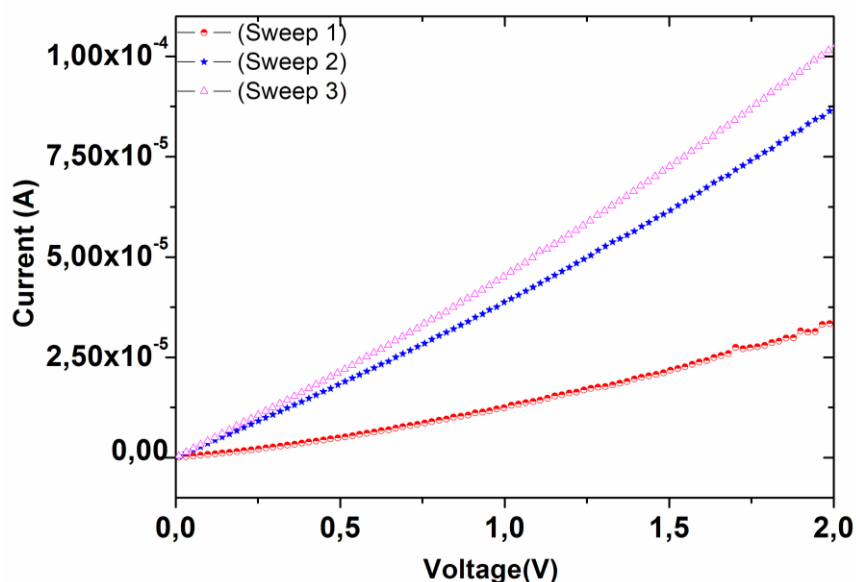

Figure 69. *I-V* characteristics obtained after electrical stress with different values of maximum current.

FE measurements were then performed by keeping the cathode tip in contact with the graphene flake and the anode one at a given distance from the flake; in this configuration, I-V characteristics were recorded for voltages ranging from 0V to 200 V. In order to avoid vacuum breakdown or damage of the graphene flake, we limited the maximum current to 10 μA.
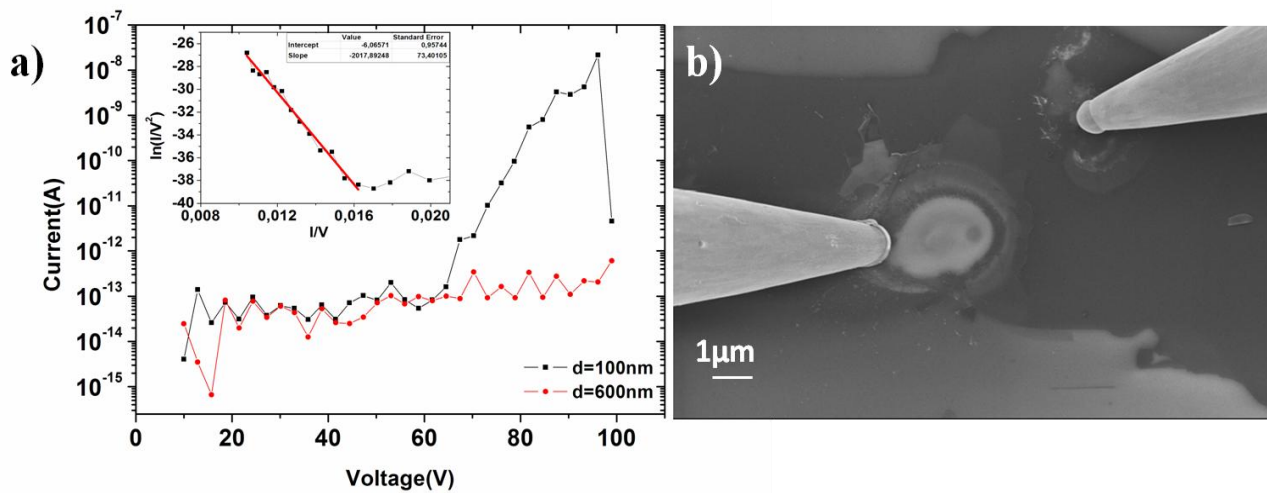

Figure 70 a) I-V curve for FE measurements at two different graphene-tip distances (100 nm, 600 nm); inset shows the Fowler-Nordheim plot for d=100nm b) Electrical breakdown resulting in melted tips and destroyed graphene as effect of high current.

Fig.70 (a) shows the current-voltage characteristics for a few-layer graphene flake at two different anode-flake distances, d~100 nm and d~600 nm. For the larger distance, we did not observe any FE current flowing between the electrodes. At reduced distance (d~100 nm), a current starts to exponentially increase for more than 5 orders of magnitude for V>60V; this current gives a linear FN plot that confirms its FE nature. Importantly, we notice that the FE current from a flat graphene layer can be described by standard FN model, no modified model being necessary to account for experimental observations. We repeated several measurements and we found them always in good agreement with equation (5.1).

The turn on field, here defined as the field needed to extract a current of 10 pA, is **$E_{on} \approx 600V/\mu m$**. This high field is not surprising since the electrons are emitted from a flat surface, which do not benefit from the high field enhancement factor of a tip-like

shape. We stress that, to the best of our knowledge, this is the first time that FE is observed from the flat, inner part of a graphene flake.

Rising the voltage, and therefore the current in the circuit, may result in a catastrophic event characterized by the melting of the tungsten tips and the local breakage of the flake. Indeed, the high current provokes high power dissipation at the graphene-tip contact (due to high resistance of the constriction), and the local heating can melt the tungsten tip and locally destroy the graphene flake (**fig.70(b)**). This phenomenon is electrically observed as a sudden drop of the FE current (last point in the I-V curve of **fig.70(a)**) resulting in an open circuit.

Furthermore we succeeded in performing FE measurements from single layer graphene. In **fig.71(b)** we show typical FE measurements, where the anode, initially in contact, was moved away from the flake at steps of ~10 nm.
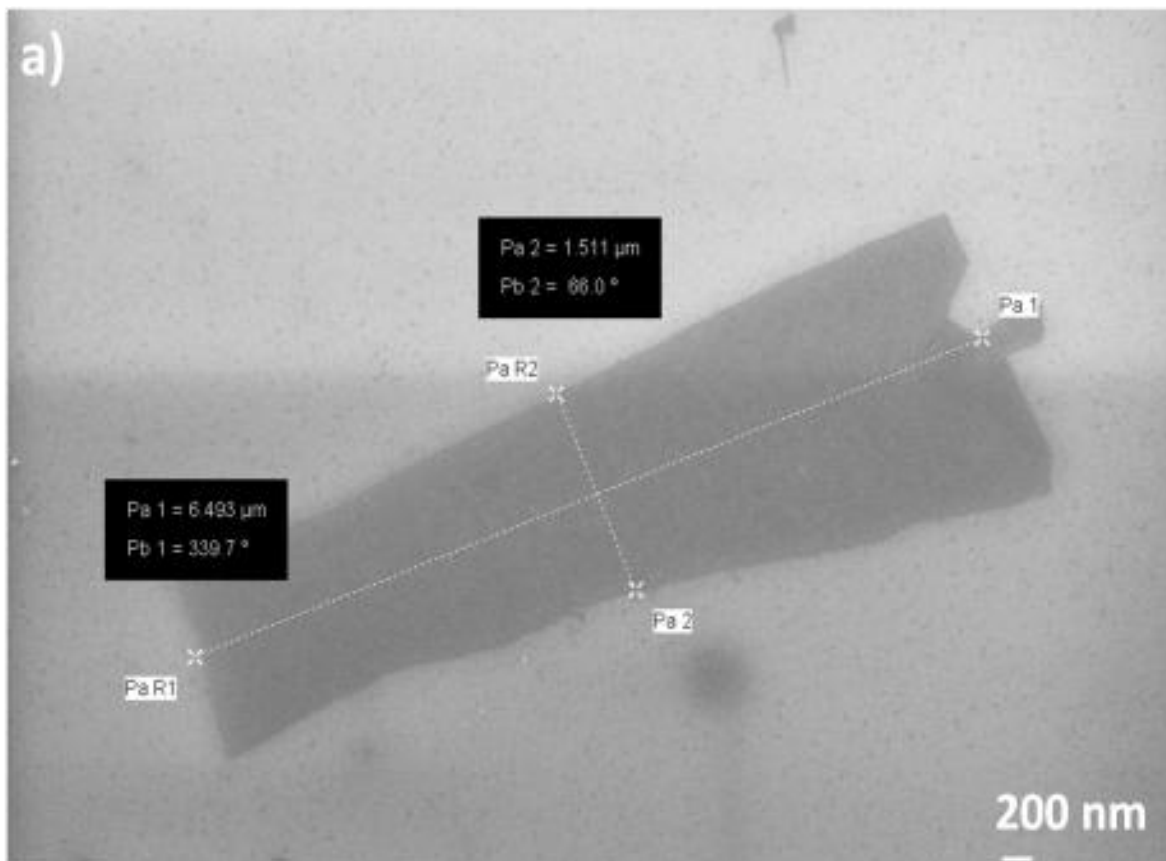

Figure 71 (a). SEM image of a single layer graphene;

SEM image of the flake that we previously characterized by optical and Raman analysis is reported in **Fig.71(a)**.

Sweep-1 and sweep-2 refer to a contact condition with a high graphene/tip contact resistance. Sweep-3 shows a change of behavior with the anode detached and FE current starting around 55 V; in this case the graphene-anode contact is soon re-established a few volts later as effect of electrostatic attraction. Moving the tip further away (sweep-4) results in the observation of FE current above 100V but for the entire voltage sweeping range (up to 175V). We point out that FE current in sweep-4 spans 6 orders of magnitude, and it follows the standard FN model, as shown in **Fig.71(c)**.
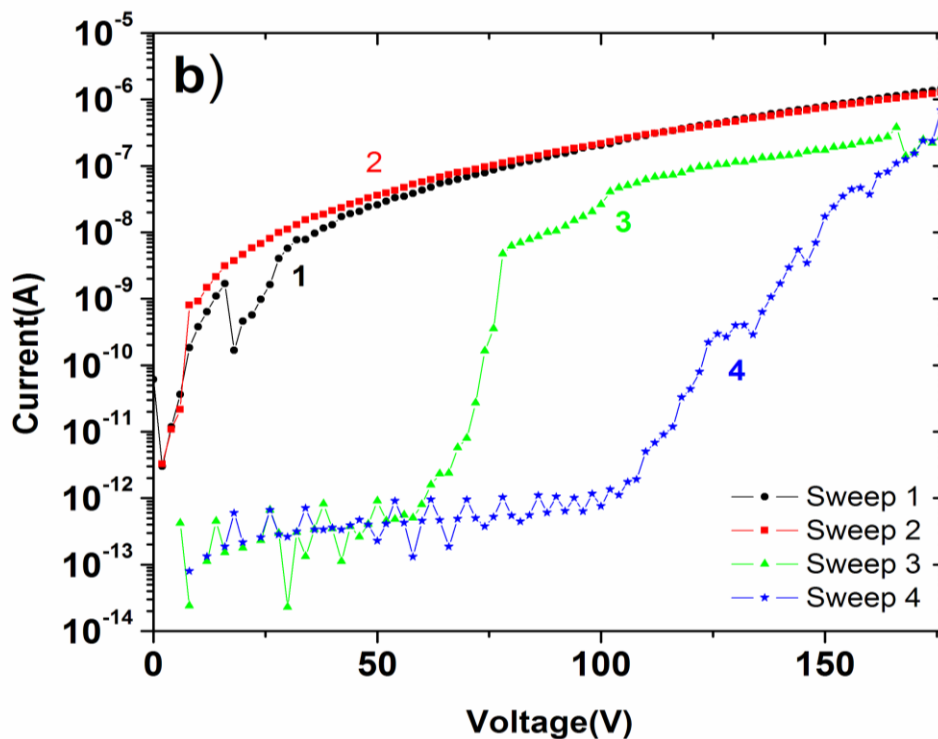

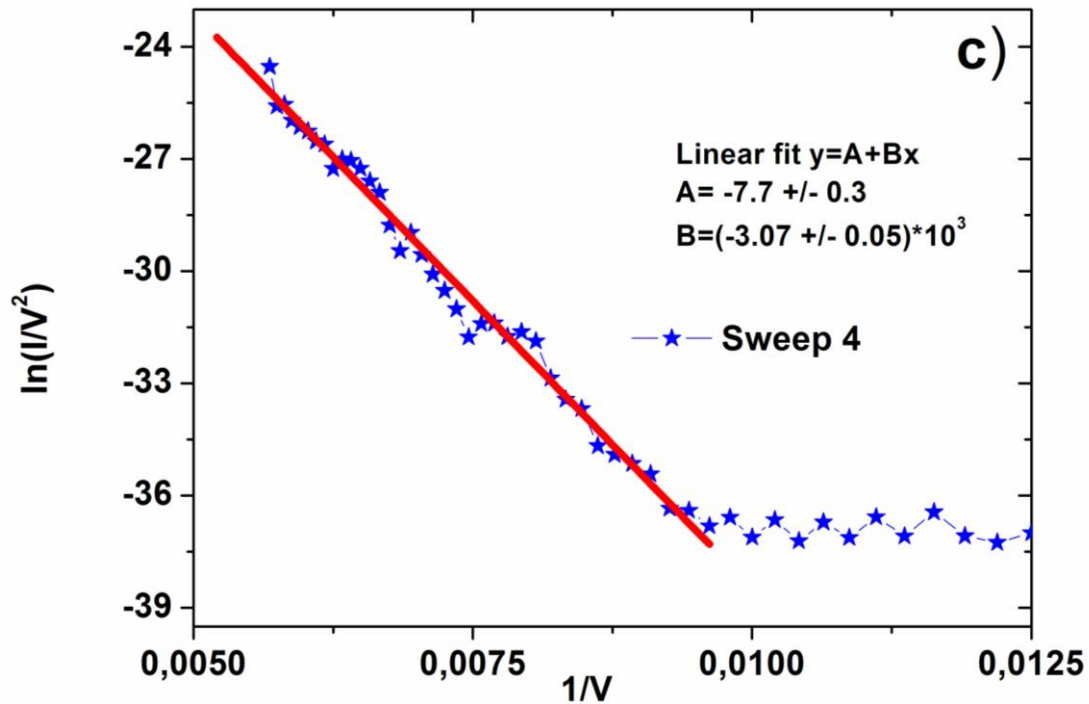**Figure 71 (b).** I-V curves measured for increasing graphene-anode distance;

Figure 71(c). Linear FN plot for FE characteristic (sweep 4).

Repeated voltage sweeps have been shown to stabilize the FE current; in particular for CNT emitters it has been shown that the electrical stabilization results also in an increase of the turn-on voltage as consequence of desorption of adsorbates and, for aligned CNT films, of burning of the longer CNTs. For graphene, we found that electrical conditioning still stabilizes the FE current which achieves a stable common value at high fields (**fig.72**); however, a different trend is observed for single layer graphene with respect to CNTs since successive sweeps reduce the turn-on field. This reverse trend can be understood considering that repeated sweeps improve the cathode-graphene contact thus changing the partition of the applied voltage among the cathode-graphene and the anode-graphene resistances. The gradually reduced cathode-graphene contact resistance makes the applied voltage mainly drop at the FE (anode-graphene) junction, where a much higher effective applied field promptly triggers FE current.
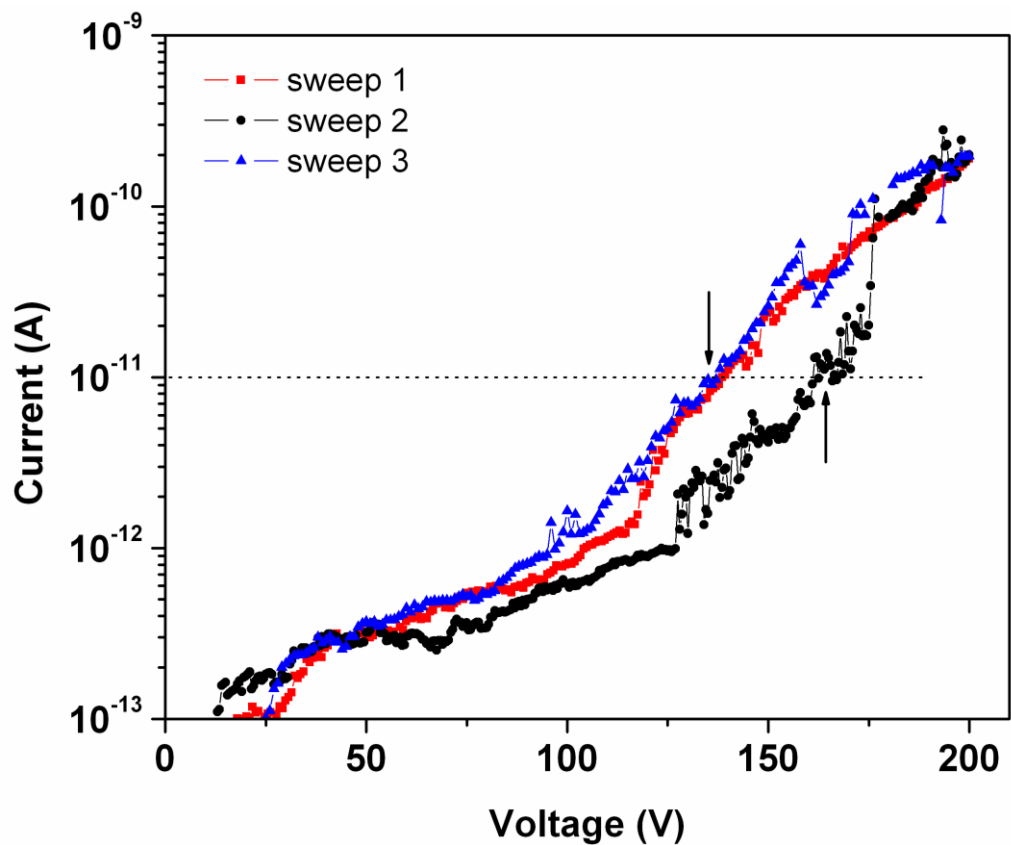
Figure 72. FE current versus bias voltage for successive sweeps at ~1μm graphene-anode distance. Arrows indicate the turn on level.
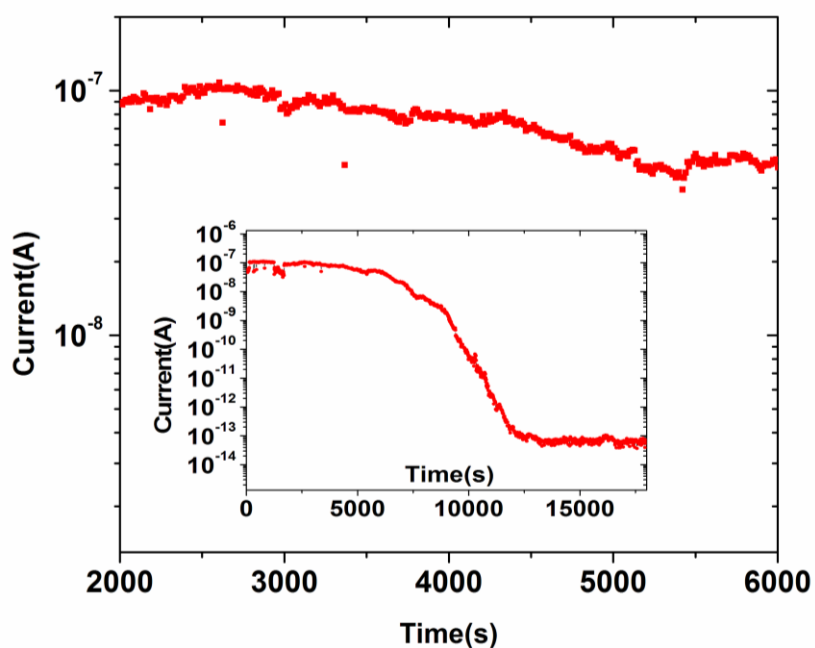

Figure 73. FE current vs time at a lower graphene-anode distance for 100V applied voltage. Inset shows the FE current over a larger time scale.

Finally, we tested the emission stability from the flat inner part of single-layer graphene flake, due to its relevance for practical applications. Experimentally, we applied a constant bias and monitored the current over periods of several hours. **Fig.73** shows the result obtained by measuring the FE current (at a graphene-anode distance adjusted to have the current at ~10^{-7} A) every 10 s under continuous bias of 100 V over a time of about 2 h. A good stability was obtained. The insert of **Fig.73** shows that for longer times thermal drift caused a gradual increase of the graphene-anode distance, leading to a current decrease till its complete suppression.

In conclusion, I presented the first observation of field emission current from the inner, flat part of single- and few-layer graphene. Taking advantage of a special setup, consisting of a two-probe nanomanipulation system operating in a scanning electron microscope (SEM) and connected to external source measurement units (SMUs), I investigated FE currents by applying electric fields up to 2 kV/μm. High and stable FE current (up to 1 μA), well described by the usual FN model over several orders of magnitude (5), was achieved with a turn-on field of ≈ 600 V/μm. The setup allowed monitoring of FE current only for few hours, over which a stable process was confirmed.

Chapter 6
Fabrication and Optical measurements of Graphene - Plasmonic Nanostructures

6.1. Introduction

Both nanophotonics and plasmonics deal with the fabrication, manipulation, and characterization of optically active nanostructures the aim of creating new tools for the nanoscale, the chemical and biomedical sensing, the information and communications technologies, enhanced solar cells and lighting, and many other applications.

Photonic materials and devices have played a pervasive role in communications, energy conversion, and sensing since the 1960s and 1970s. Photonics at the nanoscale, or nanophotonics might be defined as "the science and engineering of light-matter interactions that take place on wavelength and subwavelength scales where the physical, chemical, or structural nature of natural or artificial nanostructure matter controls the interactions".

Plasmonics aims to exploit the unique optical properties of metallic nanostructures to enable routing and active manipulation of light at the nanoscale (Barnes et al. 2003; Schuller et al. 2010; Brongersma and Shalaev 2010), [237].

Plasmonics offers a natural integration compatibility with electronics and the speed of photonics, circuits and systems formed of plasmonic and electronic devices hold promise for next-generation systems that will incorporate the best qualities of both photonics and electronics for computation and communication at high speed, broad bandwidth, and low power dissipation.

6.2. Surface plasmon photonics

6.2.1.1. Electron oscillation and dispersion relation

A surface plasmon polariton (SPP) is an electromagnetic wave propagating at the interface between a metal and a dielectric material that is coupled to a charge density oscillation of the free electrons at the surface of the metal [238, 239].
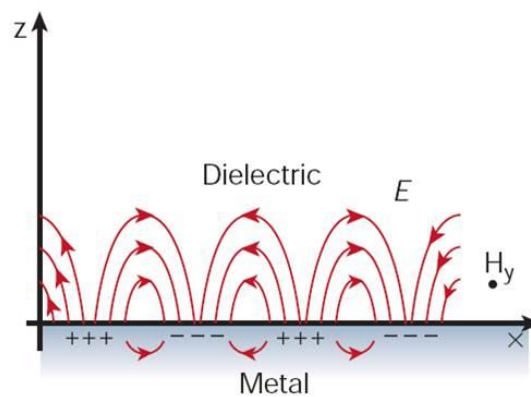

Figure 74. Polarization charges are created at the interface between two material. The electrons in metal will respond to this polarization giving rise to surface plasmon modes

Because SPPs are bound to the interface and their electric field decays exponentially perpendicular to the interface, SPPs are essentially 2-dimensional waves. This confinement and concentration of the electromagnetic field makes SPPs interesting for a wide range of applications [240- 243].

The two-dimensional confinement enables the realization of optical components with small dimensions in the out-of-plane direction [244, 245].

In the case of a metal, the bulk free electrons can oscillate with an eigenfrequency given by the plasma frequency with energies close to 10 eV. However close to the metallic surface this oscillation occurs with a lower energy and gives rise to a longitudinal charge density wave propagating along the interface [246].

This density wave is called a plasmon polariton. The coupling of this electron oscillation with the electromagnetic field is the most straightforward way to detect this wave and the resulting optical wave is the surface plasmon (SP) wave.
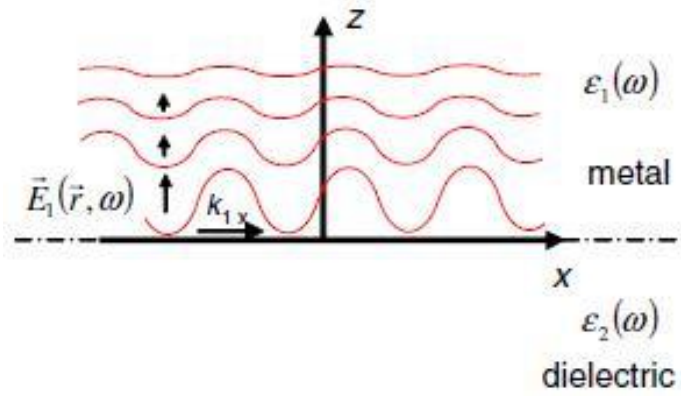
Figure 75. Structure of a surface wave (evanescent wave). The wave propagates along the *x* direction with a wavevector $k_1 x$ and has an exponentially vanishing amplitude in the direction normal to the interface (direction *z*). In the *z* direction the decay length is given by $1/kz$ and there is no propagation but an oscillation of the electric field as a whole.

The mechanical wave (oscillation of charges) and the optical wave (oscillation of the electric field) are inextricably coupled, and this explains why their names are sometimes mixed up.

The dispersion relation of the surface plasmon wave gives rise to a real $\mathbf{k_x}$ wavevector and therefore a propagation along the interface:

$$k_x{}^2 = \frac{\omega^2}{c^2} \frac{\varepsilon_1 \varepsilon_2}{\varepsilon_1 + \varepsilon_2} \tag{6.1}$$

6.2.1.2 Methods and Optical Excitation of Plasmons

The SP wave is an eigenmode of a surface wave and the most popular way of exciting it is the coupling to an external optical beam. The coupling of two electromagnetic waves requires the conservation of both the energy $\hbar\omega$ and the momentum $\hbar\mathbf{k}$ of the excitation wave. The plot of the angular frequency ω as a function of the wavevector is the best way to visualize the conditions where these two conservation laws are fulfilled. By plotting simultaneously the dispersion relations of the SP wave and the excitation

wave, it is easy to determine whether the two curves cross and the conditions that ensure this intersection.
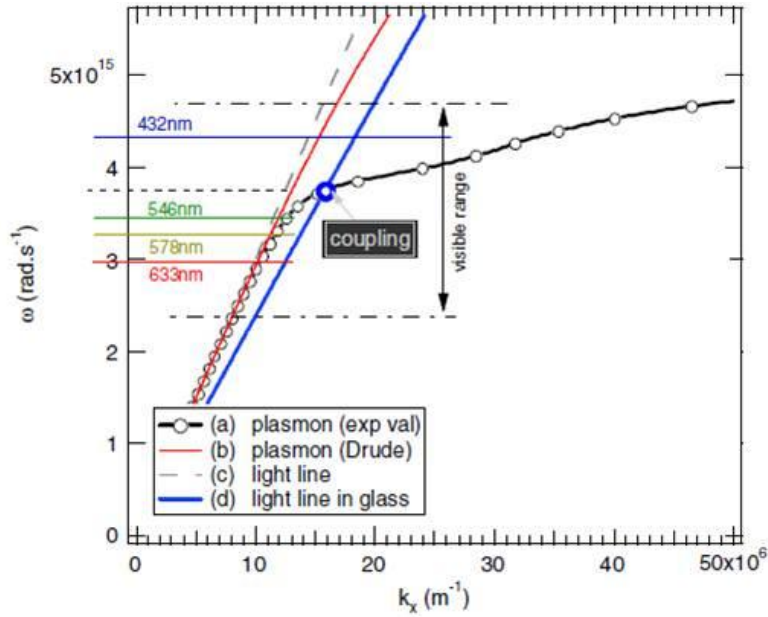

Figure 76. Dispersion relation of the surface plasmon wave at a gold/air interface.

Fig.76 is a plot of the dispersion equation of the SP wave and its coupling with an excitation wave in the case of a gold/air interface.

The dielectric function $\varepsilon_1(\omega)$ of a metal is predominantly a real number with a negative value. Materials which support these resonances must have a large and negative real component and a small positive imaginary component of its relative permittivity at the particular range of the spectrum being used. Gold (Au) and Silver (Ag) are both good candidates at the visible part of the spectrum.

On this graph two dispersion relations for the SP wave are represented according to equation below:

line (a) corresponds to the most accurate plot based on the experimental values for the dielectric function of gold and line (b) uses the simple Drude model from that only takes into account the free electrons of the metal:

$$\varepsilon_{1Drude} \sim 1 - \frac{\omega_p{}^2}{\omega^2} \tag{6.2}$$

Moreover, the dispersion of SPPs lies right from the light line, that is it has greater momentum than a free photon of the same frequency ω. This makes a direct excitation of a surface plasmon mode impossible!

To generate a surface plasmon the incident photons in plane momentum must match the momentum of the surface plasmon this cannot be achieved in air on a planer surface but can be achieved by increasing the photons momentum by passing it through a dielectric of relative permittivity greater than 1, applying a prism coupling technique. This way of exciting the SP wave is called the Kretschmann configuration and is the easiest to achieve. Another way is the Otto configuration [249] where the metallic surface is positioned away from the prism surface but close enough to capture the evanescent wave generated at a glass/air interface.

An alternative far-field excitation technique for SPPs is based on grating coupling in which a laser beam is focused onto a grating and SPPs are generated, the **fig.77** shows a schematic of this SPP excitation grating coupling technique.
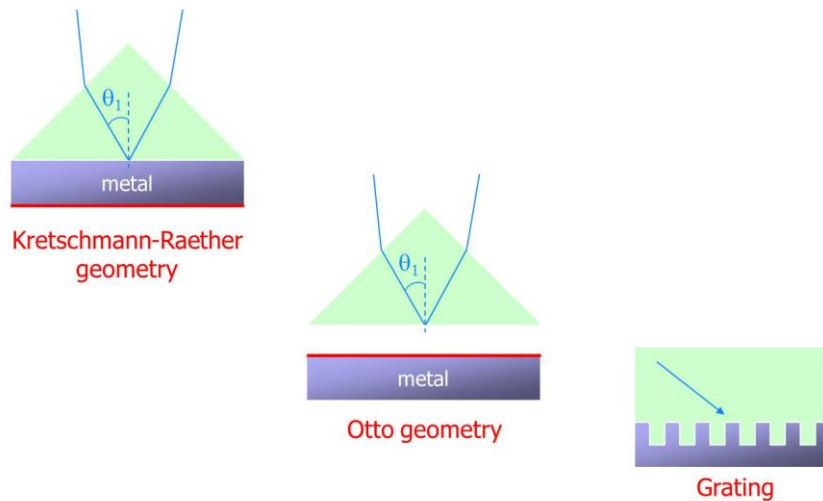

Figure 77. Three different ways to activate the SPR, in our experiments we choose the Kretschmann prism coupling configuration.

Let us consider an external wave propagating in air (medium 2, wavevector $\mathbf{k}_2$) impinging on the metallic surface with an incidence angle θ (see **fig.78**).
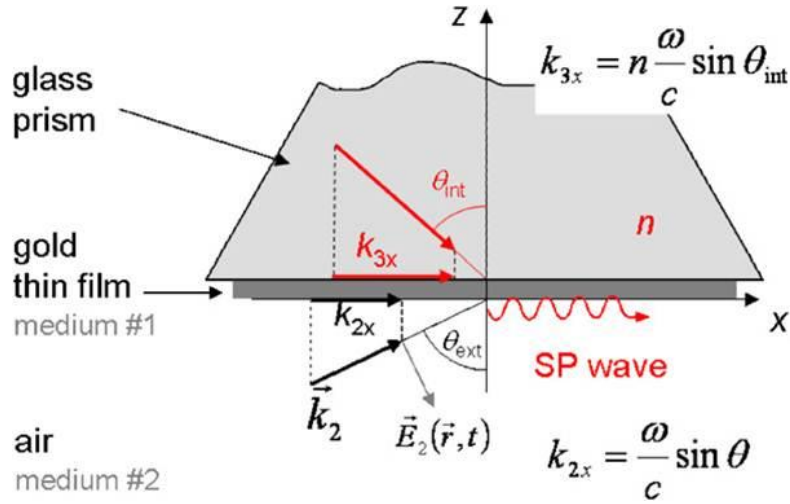
Figure 78. Sketch of impinging waves on a metallic film for exciting the SP wave in the Kretschmann configuration.

The component of the wavevector parallel to the interface $k_{2x} = k_x$ obeys the dispersion relation $\omega = k_x\, c/\sin\theta$ which is represented by the light line (c) on **fig.76** in the case $\theta = \pi/2$.

As evidenced by the graph, this light never crosses the SP dispersion relation. For an incidence angle smaller than $\pi/2$, the slope of the light line is even greater and the intersection of any of the light lines with the SP dispersion relation never occurs. Therefore, this graph shows that an external excitation always yields k_x values too small to couple with the SP wave.

One method to produce larger k_x is to launch a wave inside a medium of optical index n with an incidence angle greater than the critical angle. This third medium is often a glass prism. The wave is totally reflected and generates an evanescent wave on the other side of the interface (in the gold medium in **Fig. 78**). If θ_{int} is the incidence angle as depicted on **Fig.78**, the dispersion relation is written as:

$$\omega = \frac{k_{3x}\, c}{n\, \sin\theta_{int}} = \frac{k_x\, c}{n\, \sin\theta_{int}} \qquad (6.3)$$

Since $n > 1$, the slope of this light line in the $\omega\,(k_x)$ graph is lowered and the coupling between this wave and the SP wave is possible, as marked on **Fig.76**

Since the transfer of the momentum $\hbar k_x$ from the glass/gold interface to the gold/air interface occurs through the gold thin film, its thickness is critical. If the gold film is too thick, the energy of this evanescent wave is absorbed and the coupling is poor. Inside the gold thin film, the electromagnetic wave undergoes multiple reflections, and this can maximize the transfer of the momentum $\hbar k_x$ through the film thanks to constructive interferences.

Therefore if the film is too thin, no constructive interference takes place and the SP wave is weakly excited.

An optimal thickness, which depends on the exciting wavelength, is required to maximize the momentum transfer.
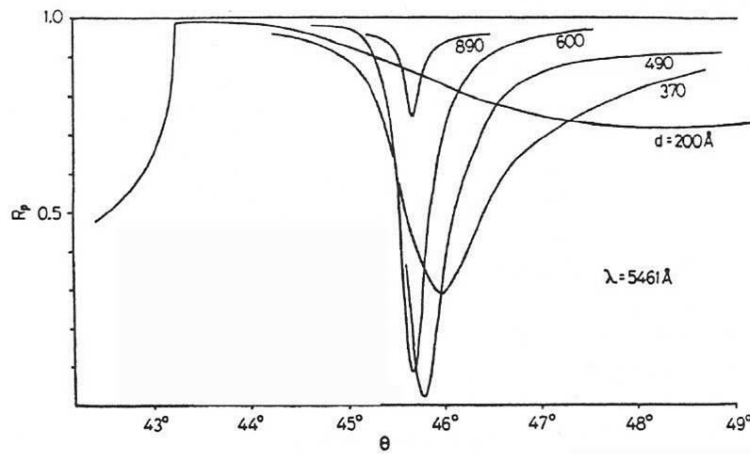

Figure 79. Reflectivity vs incident angle for different thickness d of the metal (Ag). [239]

By varying the dielectric layer thickness, the coupling between the plasmons on either side, and hence the dispersion can be tuned.

Therefore the condition for coupling the excitation wave with the SP wave is obtained by combining relations 6.1 and 6.3:

$$(n \sin \theta_{int})^2 = \frac{\varepsilon_1(\omega)\varepsilon_2(\omega)}{\varepsilon_1(\omega) + \varepsilon_2(\omega)} \tag{6.4}$$

This relation is the fundamental equation that defines the conditions for SPR to occur. Note that in the case of the gold/air interface, $\varepsilon_2 = 1$, but this formula is written in more general cases where medium 2 is a dielectric medium such as a liquid or a molecular layer adsorbed on the gold surface.

Practically, the exciting wave is generated by a laser beam with a given angular frequency ω.

In **fig.76** , this defines a point on the SP dispersion relation. The incidence angle of this laser beam θ_{int} has to be adjusted so that the light line given by relation (6.3) goes through this point. This angle θ_{int} is a solution of equation (6.4).

When this condition is fulfilled, the energy of the incident wave is converted into the SP wave and the reflected beam is damped. This is the plasmon extinction which is the usual way to detect the SPR.

6.2.1.3. Experimental Setup For Detecting The SPR and Measurements

The light source should be monochromatic and *p*-polarized. A polarized He–Ne laser ($\lambda = 543.5$ nm) with 5 mW average power is well suited to this experiment.

The addition of a half-wave plate is practical because it allows changing the polarization from *p* to *s* and is a way for turning on and off the SPR.

Another solution consists in replacing the laser with a white lamp with an interferential filter and a polarizer. The filter should have a narrow bandwidth of less than 3 nm. The resulting energy may be very low on the detector and makes accurate measurement difficult. However this solution offers the possibility of tuning the excitation wavelength by changing the filter.

A high-index equilateral prism is used n = 1.465 ± 0.007 .

5nm Cr + 55nm Gold, was evaporated on a thin layer glass of 100um, and attached on the base of the prism using a special glue.

The thickness of the metal thin film is critical (**Fig.79**) and in the case of a SP wave at the gold/air interface excited at λ = 632.8 nm, the thickness that ensures 100% coupling is 60 nm. A laser beam is incident on the rear side through the prism. SPPs on the metal surface are then excited by matching the wavelength of SPPs and incident beam in the glass, by optimizing the incident angle.

To do this, a rotation stage with an accuracy of 0.1∘ is used for measuring the angle $\boldsymbol{\theta_{ext}}$ defined in **Fig.80**. The prism is positioned on the stage so that the 180∘ angle corresponds to the laser beam being back reflected to the laser, and the angles are oriented according to the counter-clockwise orientation of the plane as indicated.

The reflected beam is collected with a reversed biased photodiode and its intensity can be read with a lock-in amplifier and goes through a minimum when the coupling with the plasmon wave occurs.

This allows us to directly measure the angle marked $\boldsymbol{\theta_{ext}}$ in **Fig.80** but the value of $\boldsymbol{\theta_{int}}$ of relation (6.4) is obtained by the following relation:

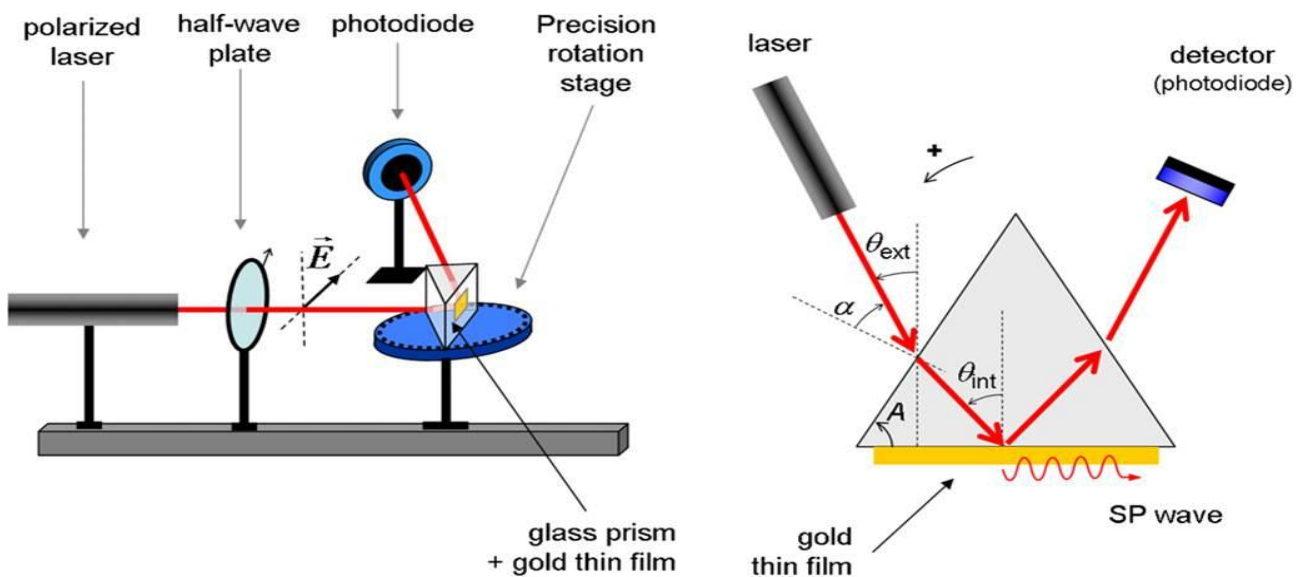$$\theta_{int} = arcsin \frac{sin(\theta_{ext} - A)}{n} + A \qquad (6.5)$$

Figure 80. Schematic of Morley Kit, Optical setup for measuring the plasmon extinction , where A is the angle of the prism 45°

Fig.81 presents the results obtained with this setup. The reflected intensity measured with the photodiode has been recorded as a function of the external angle θ_{ext}.

The intensity almost drops to zero which is the sign that the excitation beam transfers its energy to the SP wave.

The signature of the plasmon excitation is the sharp dip in the reflection curve around $\theta_{int} = \theta_{plasmon} = 14.5 \pm 0.1°$.

Nevertheless if the surface of the gold film is damaged or exhibits some roughness, the near-field of the surface wave is converted into far-field propagating waves and causes diffusion. In this case the coupling with the plasmon wave can be visualized when the gold surface starts to glow. The angular position of the SPR is extremely dependent on the quality and the cleanliness of the gold surface.

The reflectivity curve displays a drop indicated by (Critical Angle in **Fig.81**) which corresponds to the critical angle of total internal reflection given by **arcsin $1/n$ = 43°**. For an angle larger than the CA, the excitation beam is fully reflected on the internal interface of the prism, which creates the evanescent wave needed to excite the SP wave as discussed above. The measured value of $\theta_{plasmon}$ at which the SPR occurs can be used to estimate the dielectric function of gold, using relation 6.4.
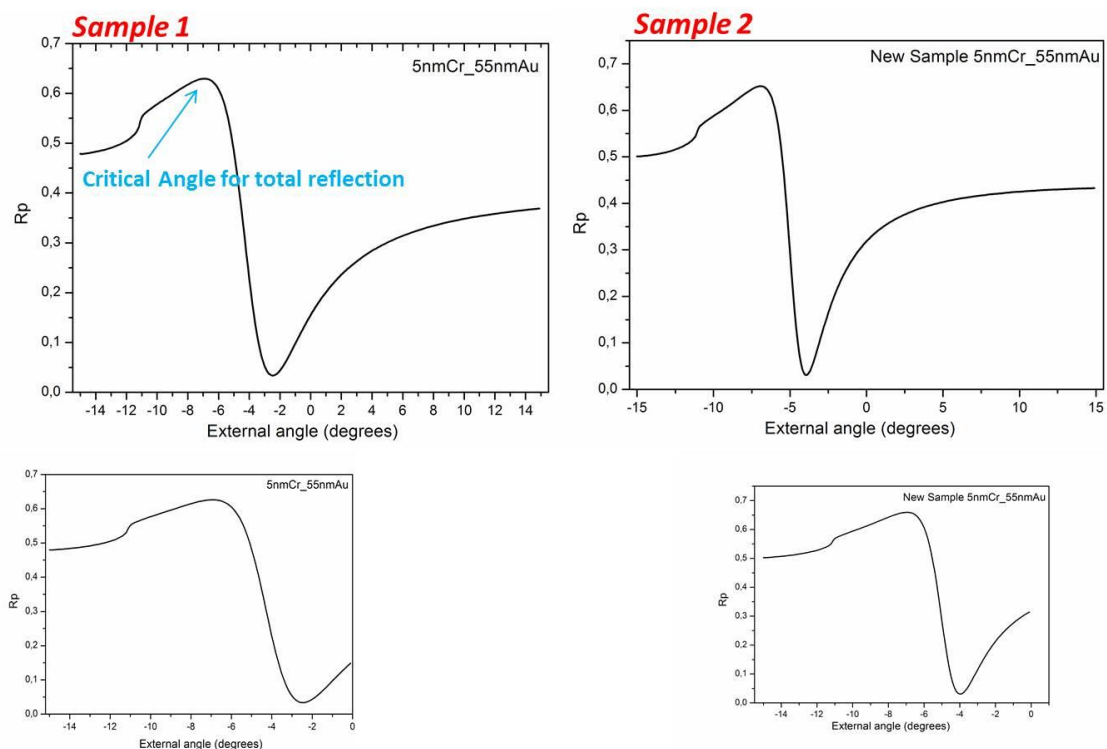
Figure 81. Surface plasmon extinction curve for a gold/air interface measured at a wavelength of 632.8 nm in p-polarization.

$$Sample_1 \; \theta_{int} = \theta_{plasmon} = 14.5 \pm 0.1°$$
$$Sample_2 \; \theta_{int} = \theta_{plasmon} = 13.8 \pm 0.1°$$
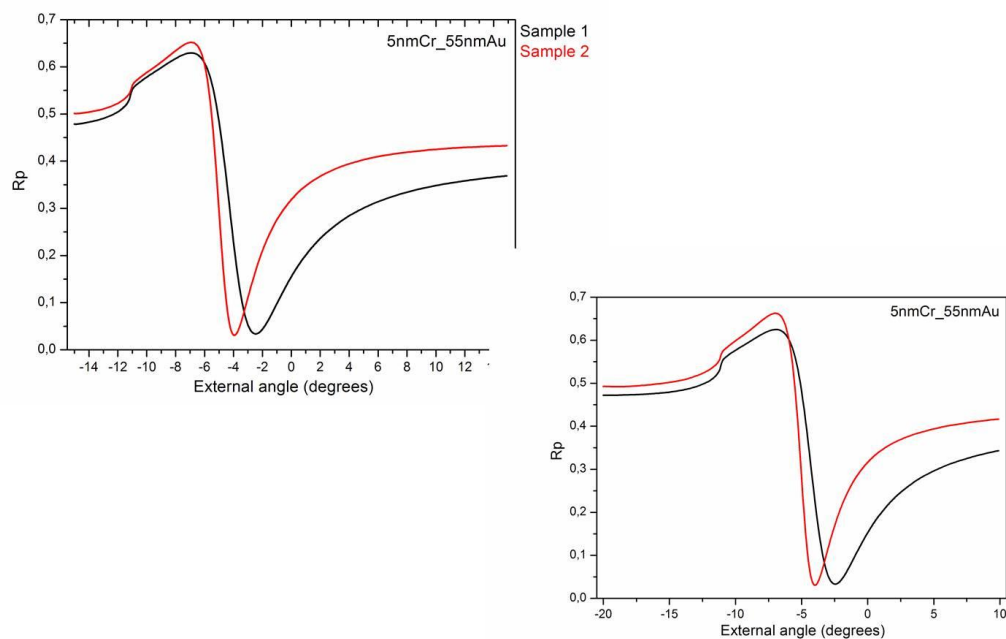

Figure 82. The angular position of the SPR is extremely dependent on the quality and the cleanliness of the gold surface and the plasmon shifts as the wavelength decreases.
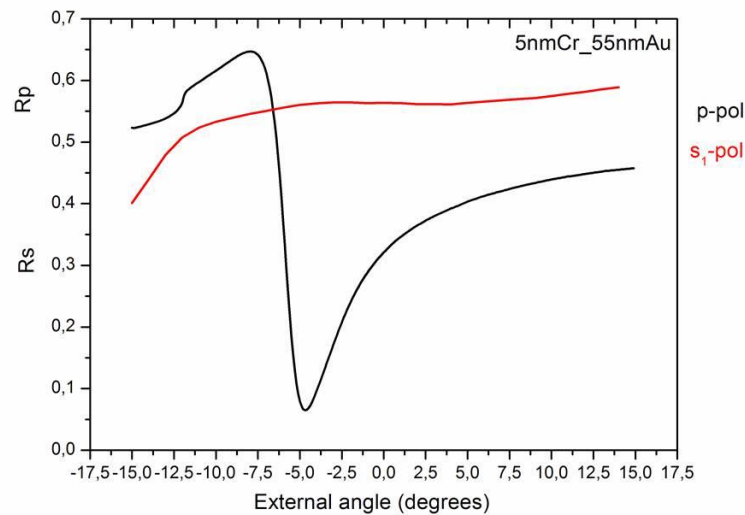
Figure 83. Difference between P and S Polarization S-polarized incident radiation does not create polarization charges at the interface. It thus can not excite surface plasmon modes. changing 90°the Polarizer.

On the other hand, the exact calculation of the reflected intensity as a function of the internal angle reproducing the plasmon extinction is possible. It can be achieved with the Fresnel relations applied in a three-layer model. The crucial part is to implement a calculation based on the complex dielectric function of gold.

6.2.1.4. Simulation of Reflectivity Spectra of the Surface Plasmon

The Fresnel equations for a three layer and two interfaces system allow one to extract the complex permittivity and thickness of the film from a fit to the resonance spectrum. In the first medium we have an incoming wave and a reflected. In the sandwiched layer we also have two waves, one going in the positive direction and one in the negative direction. In the third medium we only have one wave travelling in the positive direction. We use the same type of boundary conditions as we used in the single interface geometry at both boundaries and find the amplitudes and angles for the waves.

The total reflected amplitude, r, is obtained from an infinite summation of waves due to the multiple reflections in the middle layer. Each time a wave impinges on an interface

the Fresnel equations are used and the phases of the waves are taken into account. All coefficients are complex valued.
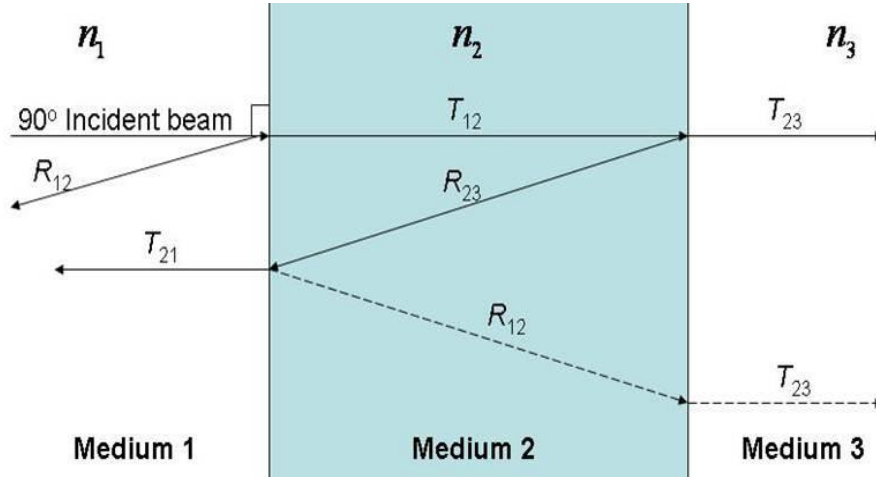

Figure 84. Waves contributing to the total reflected and transmitted waves in a three layer structure

The phase $2\delta_2$ is the phase difference for two waves: one wave that is transmitted through the first interface, passing through layer 2, is reflected at the second interface, passing through layer *2* again and is finally transmitted through the first interface; the second wave is one that is reflected at the first interface. This second wave has furthermore traveled a longer distance in layer 1 before it impinges on the interface. Summering the results we obtain:

$$r = \frac{r_{12}e^{-i\delta_2} + r_{23}e^{i\delta_2}}{e^{-i\delta_2} + r_{12}r_{23}e^{i\delta_2}} = \frac{r_{12} + r_{23}e^{i2\delta_2}}{1 + r_{12}r_{23}e^{i2\delta_2}} \tag{6.6}$$

$$t = \frac{e^{i\delta_2}t_{12}t_{23}}{1 + r_{12}r_{23}e^{i2\delta_2}} \tag{6.7}$$

Using Mathematica program is easy to write the algorithm of the reflectance R vs the angle of incidence and the **Fig.85** shows the plot of the extracted algorithm from my data and from the general case:
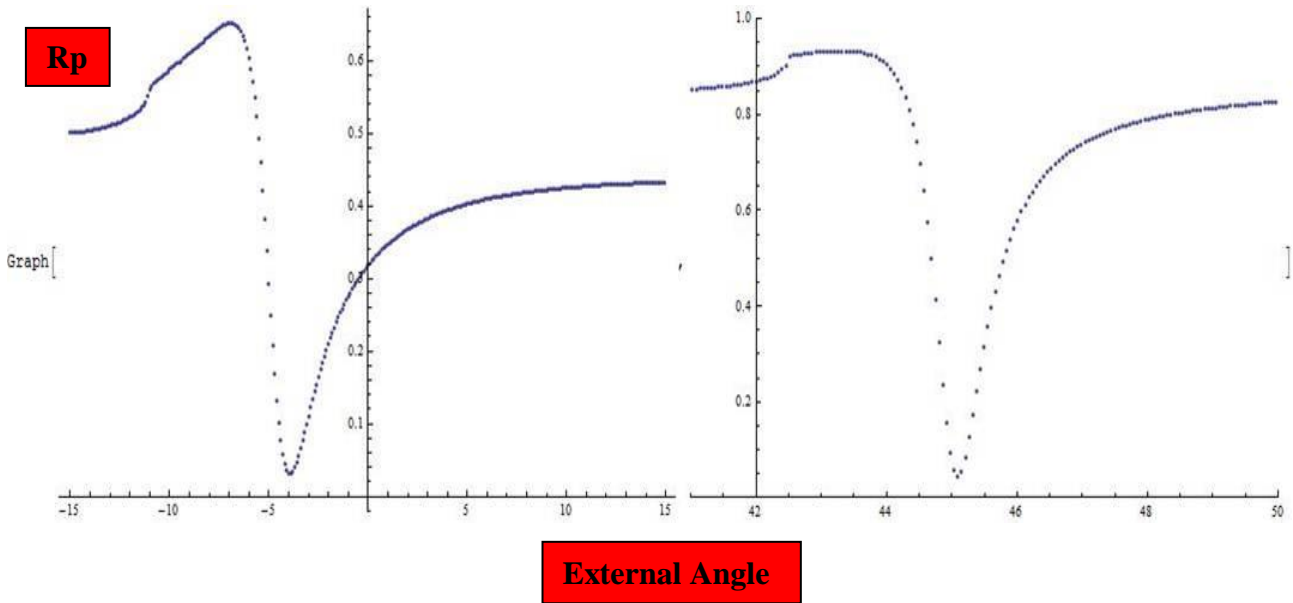

Figure 85. Calculated reflectivity spectra

Both the prism and grating coupling technique are rather bulky geometries and are therefore impractical for the use in small integrated circuits or sensors.

But in the next's we will explore another way to go down in sub-wavelength scale.

6.3. Localized Surface Plasmons (LSP)

The second fundamental excitation of plasmonics is localized surface plasmons.

Localized surface plasmon resonance (LSPR), takes place in small metallic particles and corresponds to a global oscillation of the free surface electrons on a nanoparticle (plasma oscillation) **Fig.86** constrained by the tight boundary conditions imposed by the spheroidal shape of the particles.

Light may interact with metallic particles much smaller than the wavelength of light making them visible under dark field microscopy. The LSPR is very sensitive to the size and shape of the nano particle and both the SPR and LSPR wavelength are extremely sensitive to the dielectric environment which is locally surrounding it [247].
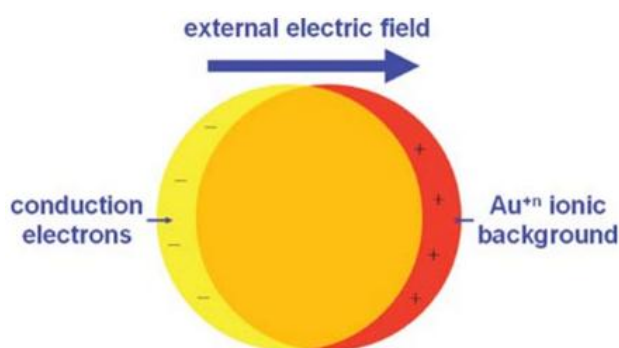

Figure 86. Oscillation of the free surface electrons on a nanoparticle

We have seen that SPPs are propagating, dispersive electromagnetic waves coupled to the electron plasma of a conductor at a dielectric interface. Localized surface plasmons on the other hand are non-propagating excitations of the conduction electrons of metallic nanostructures coupled to the electromagnetic field. These modes arise naturally from the scattering problem of a small, sub-wavelength conductive nanoparticle in an oscillating electromagnetic field. The curved surface of the particle extracts an effective restoring force on the driven electrons, so that a resonance can arise, leading to field amplification both inside and in the near-field zone outside the particle.

This resonance is called the localized surface plasmon or short localized plasmon resonance. Another consequence of the curved surface is that plasmon resonances can be excited by direct light illumination, in contrast to propagating SPPs, where the phase-matching techniques described have to be employed.

Here, I briefly discuss the physics of localized surface plasmons by first considering the interaction of metal nanoparticles with an electromagnetic wave in order to arrive at the resonance condition.

For gold and silver nanoparticles, the resonance falls into the visible region of the electromagnetic spectrum. A striking consequence of this is the bright colors exhibited by particles both in transmitted and reflected light, due to resonantly enhanced absorption and scattering. This effect has found applications for many hundreds of years, for example in the staining of glass for windows or ornamental cups.

The interaction of a particle of size d with the electromagnetic field can be analyzed using the simple quasi-static approximation provided that $d \ll \lambda$, i.e. the particle is much smaller than the wavelength of light in the surrounding medium. In this case, the phase of the harmonically oscillating electromagnetic field is practically constant over the particle volume, so that one can calculate the spatial field distribution by assuming the simplified problem of a particle in an electrostatic field.

We start with the most convenient geometry for an analytical treatment: a homogeneous, isotropic sphere of radius a located at the origin in a uniform, static electric field $\mathbf{E} = E_0 \mathbf{z}$ (**Fig.87**). The surrounding medium is isotropic and non-absorbing with dielectric constant ε_m and the field lines are parallel to the z-direction at sufficient distance from the sphere. The dielectric response of the sphere is further described by the dielectric function $\varepsilon (\omega)$, which we take for the moment as a simple complex number ε.
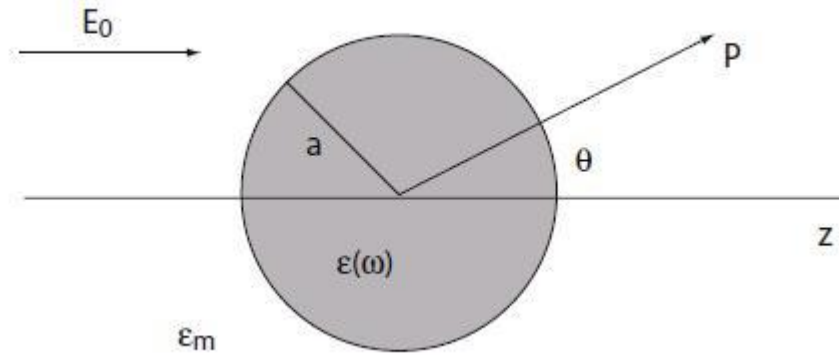
Figure 87. Sketch of a homogeneous sphere placed into an electrostatic field

An applied field induces a dipole moment inside the sphere of magnitude proportional to $|\mathbf{E}_0|$. If we introduce the polarizability *a*, defined via $\mathbf{p} = \varepsilon_0\varepsilon_m\, \alpha\, \mathbf{E}_0$, we arrive at:

$$\alpha = 4\pi a^3 \frac{\varepsilon - \varepsilon_m}{\varepsilon + 2\varepsilon_m} \tag{6.8}$$

Equation is the central result of this section, the (complex) polarizability of a small sphere of sub-wavelength diameter in the electrostatic approximation.

We can see from the equation that a peak in the response will occur if :

$$\mathrm{Re}\,[\varepsilon\,(\omega)] = -2\varepsilon_m \tag{6.9}$$

This relationship is called the Fröhlich condition and it is associated (in an oscillating field) to the dipole surface plasmon of the metal nanoparticle.

This relation expresses the strong dependence of the resonance frequency on the dielectric environment: The resonance red-shifts as ε_m is increased. Metal nanoparticles are thus ideal platforms for optical sensing of changes in refractive index and the resonance in α also implies a resonant enhancement of both the internal and dipolar fields. It is this field-enhancement at the plasmon resonance on which many of the prominent applications of metal nanoparticles in optical devices and sensors rely.

Thus, for a small sphere with $a << \lambda$, its representation as an ideal dipole is valid in the quasi-static regime, i.e. allowing for time-varying fields but neglecting spatial retardation effects over the particle volume. Under plane-wave illumination with $\mathbf{E}(\mathbf{r},\ t) = \mathbf{E}_0 e^{-i\omega t}$, the fields induce an oscillating dipole moment $\mathbf{p}(t) = \varepsilon_0 \varepsilon_m a \mathbf{E}_0 e^{-i\omega t}$, with a given by the electrostatic result . The radiation of this dipole leads to scattering of the plane wave by the sphere, which can be represented as radiation by a point dipole.

From the viewpoint of optics, another consequence of the resonantly enhanced polarization a is a concomitant enhancement in the efficiency with which a metal nanoparticle scatters and absorbs light.

The corresponding cross sections for scattering and absorption C_{sca} and C_{abs} can be calculated via the Poynting-vector.

The theory of scattering and absorption of radiation by a small sphere predicts a resonant field enhancement due to a resonance of the polarizability a (6.8) if the Frölich condition (6.9) is satisfied.

Under these circumstances, the nanoparticle acts as an electric dipole, resonantly absorbing and scattering electromagnetic fields.

This theory of the dipole particle plasmon resonance is strictly valid only for vanishingly small particles with dimensions below 100 nm illuminated with visible or near-infrared radiation.

For particles of larger dimensions, where the quasi-static approximation is not justified due to significant phase-changes of the driving field over the particle volume, a rigorous electrodynamics approach is required.

A good approximation to the scattering from a small arbitrary shaped particle is developed by Mie in 1908 in a seminal paper, in which he described an exact field solutions to Maxwell's wave equation for a spherical geometry [247, 250] of arbitrary radius and of arbitrary refractive index, and a complete theory of the scattering and absorption and back scattering cross sections of electromagnetic radiation by a sphere, in order to understand the colors of colloidal gold particles in solution. [251].

6.4. Graphene plasmonics

6.4.1.1. Introduction

Graphene plasmons provide a suitable alternative to noble-metal plasmons because they exhibit much larger confinement and relatively long propagation distances, with the advantage of being highly tunable via electrostatic gating.

In particular, graphene plasmons are confined to volumes $\approx 10^6$ times smaller than the diffraction limit, thus facilitating strong light-matter interactions. Furthermore, tuning of the plasmon spectrum is possible through electrical or chemical modification of the charge carrier densities, [252, 253].

Graphene offers an interesting prospect as an optoelectronic substrate, it is transparent, can be made conductive, and is very thin. At the same time the unique properties displayed by the plasmon modes associated with metallic nanoparticles allow the manipulation and control of visible light deep into the sub-wavelength regime, with applications ranging from treatment of cancer [254] to data storage [255] and bio-sensing based on propagating surface plasmon resonances (PSPR) and localized surface plasmon resonances (LSPR) [247,256].

The combination of these two classes of material, graphene and metallic nanoparticles, offers exciting prospects not available from either material on its own.

With regard to sensing, graphene/plasmonic-nanoparticle materials show great promise for surface enhanced Raman spectroscopy (SERS)[257–259], and have significant potential for future plasmon-based sensors and biosensors [260].

Firstly, the graphene surface exposed between the nanoparticles could be easily modified for additional, selectivity-enhancing functionality (including bio-functionality) using the non-covalent but irreversible π-π stacking of linker molecules based on moieties such as pyrene [261].

Secondly, the ability to produce transparent, layered structures of nanoparticles interspersed with graphene sheets opens up the possibility of multiple-plasmon readout. Thirdly, combinations of LSPR and electrochemical sensing are possible on these nanoparticle-decorated electrodes. Arrays of metallic nanoparticles have often been made on ITO by electron-beam lithography [262–264] and by electrochemistry [265-267]; more recently they have also been made on graphene by electrochemistry [268–275] but, to the best of the authors' knowledge, the present work is the first instance of gold or silver nanoparticles being electrodeposited onto graphene on a transparent (here glass) substrate.

With regard to optoelectronics, the use of graphene rather than ITO as a substrate for metallic nanoparticles also opens up many possibilities; may find application in flexible optoelectronics, for example in plasmonically enhanced flexible photovoltaic cells [276].
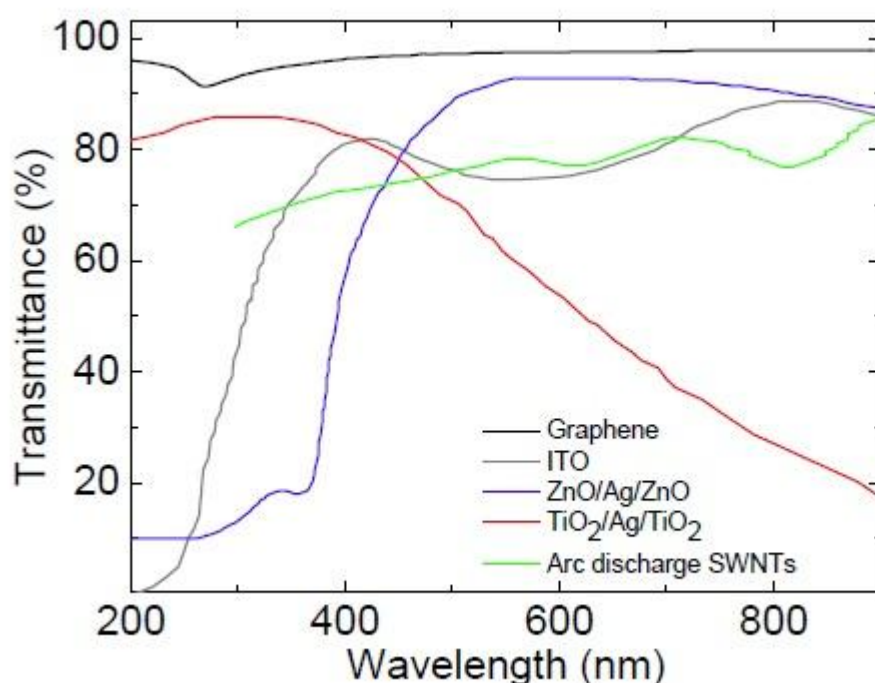

Figure 88. Graphene films have higher T over a wider wavelength rangewith respect to SWNT films, thin metallic films, and ITO

6.4.1.2. Graphene as a substrate for plasmonic nanoparticles

During my research activities at Centre for Graphene Science, I have been involved in the investigation of the plasmonic properties of metallic nanoparticles supported by substrates made of graphene. Here, I present the results we obtained after an intense work and many efforts.

Specifically, we studied the properties of plasmonic nanoparticles supported by graphene substrates, fabricated using electron-beam lithography to produce ordered arrays of metallic nanoparticles.

The results show that both pristine graphene and the more conducting intercalated variant, graphExeter [277], are excellent substrates for plasmonic nanoparticles owing to their transparency and atomically thin nature, opening an interesting route for building plasmon-based bio- and chemical-sensors, and for developing transparent and flexible optoelectronics.

To explore the properties of plasmonic nanoparticles on graphene substrates, we undertook an investigation employing two very different methods. In the first we used electron-beam lithography as a top-down nanofabrication route, in the second method we used electro-deposition as a bottom-up approach that is attractive for low cost, large scale applications.

Here, I report the first method, and we study for the first time the effect of graphene on the plasmon resonances. Metal particles have been produced on graphene by electron-beam lithography before [278], but the effect of the graphene on the plasmon resonance of particles in direct contact with the graphene was not investigated.

The focus of the work reported here was to assess how the plasmonic response of metallic nanoparticles is modified by the presence of a graphene substrate.

The peak and spectral position of the plasmon response of a metallic sphere in the scattering intensity is strongly dependent on the size and shape of the nanoparticle and also on the dielectric environment surrounding them, and can be understood by looking at an expression for its polarizability, α, in the electrostatic limit as calculated upon (equation 6.28).

The permittivity of silver and gold is negative and is a strongly varying function of wavelength in the visible part of the spectrum. As a result a peak response for the metal sphere occurs, its spectral position depending on the permittivity (refractive index) of the environment ϵ_m.

This dependence of the resonance on the refractive index of the region around the particle is central to the use of LSPRs as sensors [247]. Part of the reason for our study was to see whether the presence of graphene leads to a shift in the spectral position of the plasmon resonance: graphene has a higher refractive index than typical glass substrates so one might expect its presence to shift the spectral position of the plasmon resonance [279, 280].

6.4.1.3. Periodic arrays of metallic nanoparticles produced on graphene by electron-beam Lithography

Localized plasmon resonances can readily be observed using far-field extinction microscopy on colloidal or nanofabricated metal nanostructures under illumination with visible light. A convenient way to create particles with a variety of shapes, is electron beam lithography or Nano Beam Lithography (NBL), followed by a metal lift-off process. If far-field extinction microscopy is employed, the small size of nanoparticles with $d \ll \lambda$ compared to the at-best diffraction-limited illumination spot requires excitation of plasmons in arrays of particles of equal shape in order to achieve an acceptable signal-to-noise ratio in the extinction spectra. Typically, the particles are arranged on a square grid [Craighead and Niklasson, 1984], with a sufficiently large interparticle spacing to prevent interactions via dipolar coupling.
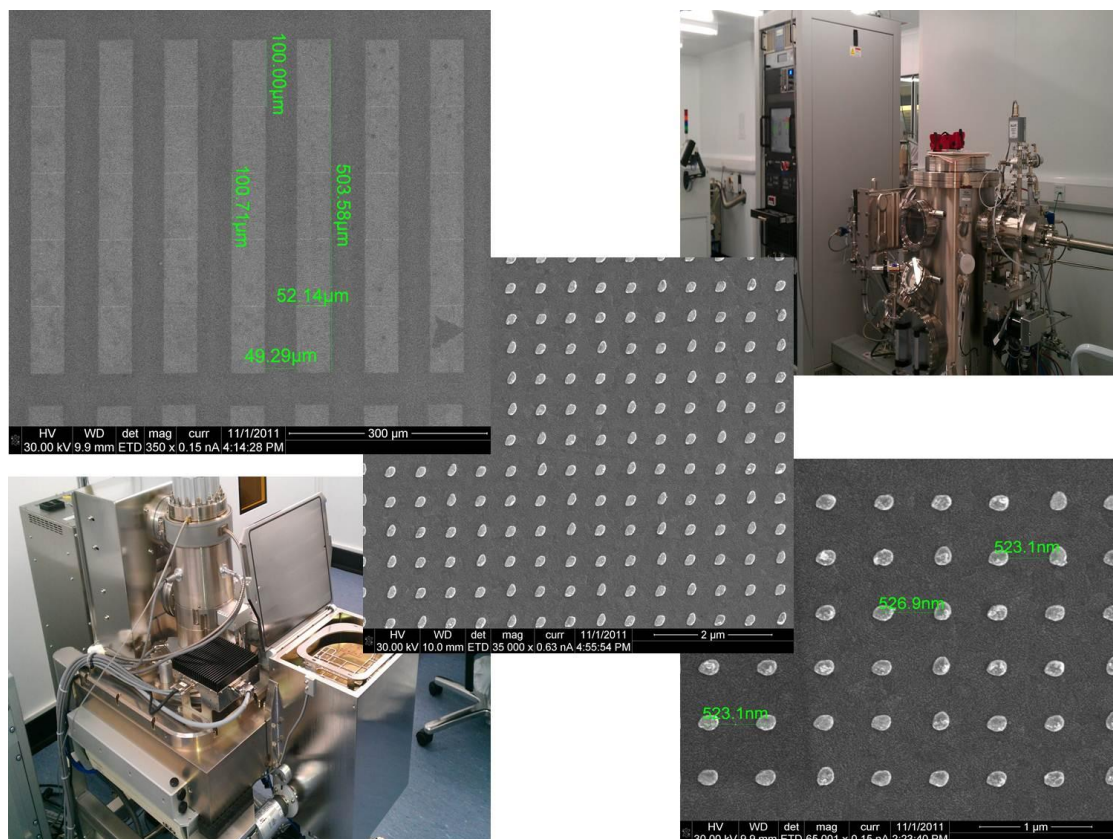
Figure 89. Array of gold nanoparticles of 200nm with spacing of 500nm on ITO substrate, on the left: Nano Beam Lithography to produce the array and on top the sputtering system to evaporate metal.
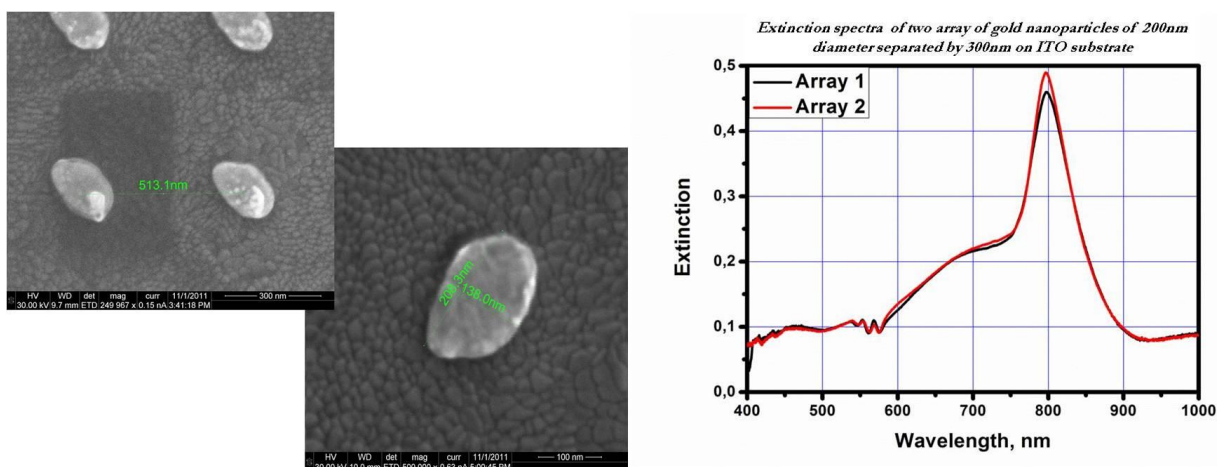

Figure 90. SEM images of the nanoparticles, showing the size and the shape completely ellipsoidal. The geometry plays an important rule because it changes the excitation of the plasmons and consequently the spectral position of the plasmon resonance. On the right the spectra resonance associated to the particles.

Silver metallic nanoparticles were made by electron-beam lithography (EBL), silicon wafers coated with 300 nm of SiO_2 were used as substrates. First, graphene flakes were deposited on these substrates by mechanical exfoliation, and flakes of different thicknesses (ranging from 1-6 layers) were identified using optical microscopy, the number of layers being determined through examination of their optical contrast (further details in methods section). Regular arrays of silver nanoparticles were patterned on the graphene flakes by standard electron-beam lithography, evaporation and lift-off processes. The arrays consist of nano-discs of 100 nm diameter and 50 nm thickness on a square lattice of period 1.0 µm (see **fig.91**).
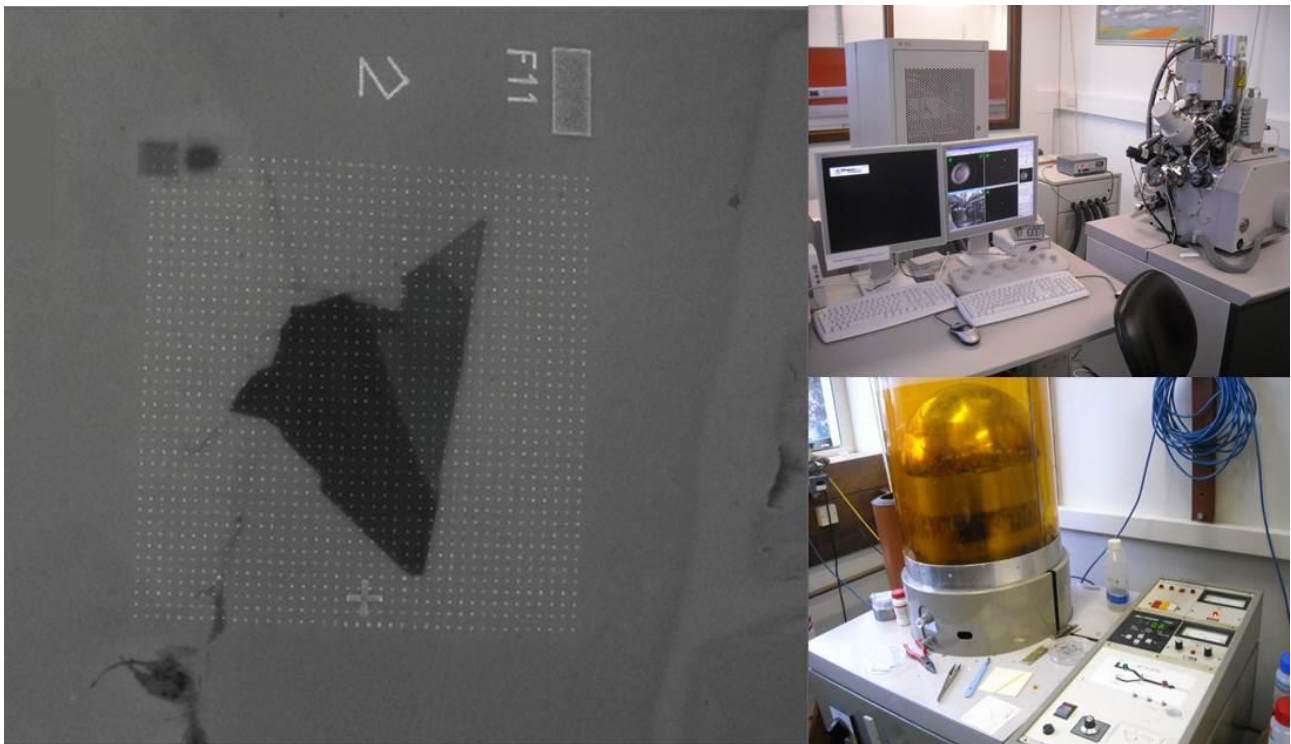

Figure 91. Scanning electron micrograph of an array of silver nanoparticles deposited onto a graphene flake by electron-beam lithography and sample structure and geometry. The regions of the flake visible through their different grey scales are: thick, ~ 10 layers of graphene, darkest; 2 layers, middle; and 1 layer, lightest. The scale bar is 500 nm

6.4.1.4. Measurement Setup

In contrast to far-field extinction microscopy techniques, far-field dark-field optical microscopy and near-field optical extinction microscopy enable the observation of plasmon resonances of a *single* particle. In dark-field optical microscopy, only the light scattered by the structure under study is collected in the detection path, while the directly transmitted light is blocked using a darkfield condenser. This enables the study of single particles dilutely dispersed on a substrate.

So, to characterize the optical properties of the fabricated particles we performed dark-field scattering measurements in reflection mode (see **Fig.92**) [281].
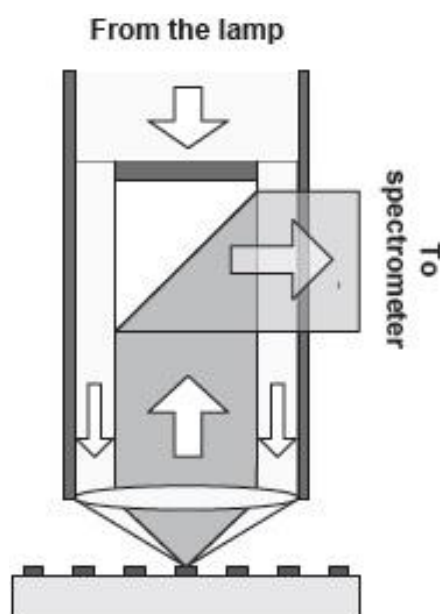

Figure 92. Arrangement used to acquire dark-field scattering spectra. Light is sent through the outer cladding of the objective so as to illuminate samples at grazing angles of incidence. Scattered light is collected and directed to the spectrometer.

Fig.93 shows a schematic of a dark field setup the incident light comes in an incident angle to the surface normal. If there is no scattering object in the path of the incident light then the scattered intensity will be zero.

If on the other hand there is a scattering object present such as metal nanoparticle some of the light will be scattered into the condenser lens, this light will then be directed onto a detector and a measure of the scattering intensity can be made. The source for DF microscopy is an unpolarised white light source.
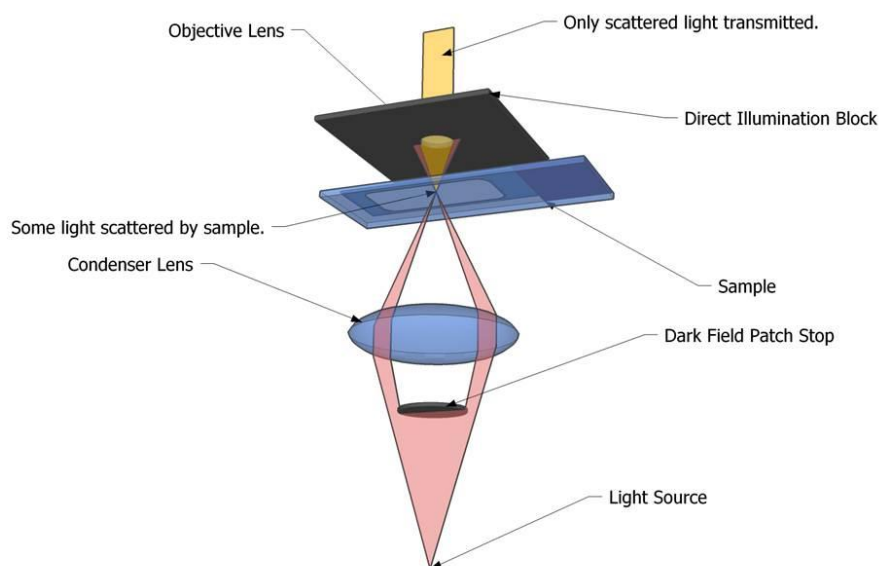

Figure 93. Dark field microscopy

Particles with diameter of 100nm can easily be resolved under DF illumination so long as the particle-particle separation is ≈ 1μm, this separation distance is required so that the particles are far enough apart so that they do not interact, **Fig.94**.
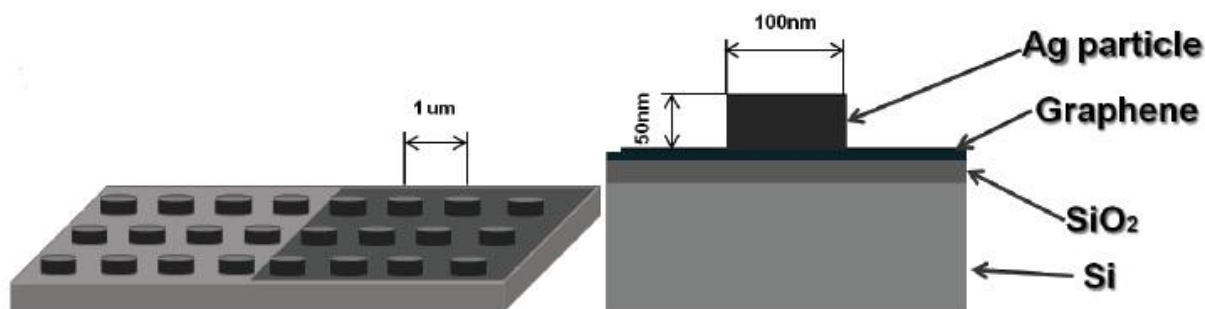

Figure 94. The arrays into which silver nanoparticles were formed in and the design details of the circular disc shaped silver nanoparticles.

An inverted optical microscope (Nikon Eclipse TE200-U) and spectrometer (Princeton Instruments, Spectra Pro 2500i) with a charge-coupled device (CCD) camera (Princeton Instruments, Pixis) see **Fig.95,** were used to acquire spectra from the scattered light. Illumination was provided by a tungsten filament lamp, via the outer cladding of a dark-field objective (Nikon x150, NA 0.90, LU Plan Apo, WD 0.42) so as to illuminate the sample at grazing angles of incidence. We chose an entrance slit of 500μm for the spectrometer so as to allow spectra to be obtained from ~ 20 particles at once with a resolution better than 10 nm.

Figure 95. Optical Microscope, Spectrometer, CCD

6.4.1.5. Results and Analysis

The scattered light spectra, I_{scat} (λ) were normalized with reference to the background scattering spectra. The intensity distribution of the lamp and also the small scattered intensity which will be present if no particle were present and also the background noise of the detector must be removed from the signal. The normalized scattering intensity in this cone is then where all the intensity's have had a background spectrum subtracted from it. Therefore, I_{scat} (λ) obtained from the substrate as follows:

$$I_{norm}\ (\lambda) = \frac{I_{scat}(\lambda) - I_{back}(\lambda)}{I_{back}(\lambda)} \tag{6.10}$$

Here I_{scat} is the signal recorded by the CCD camera with the sample in place, and I_{back} is the measured spectrum of light scattered by the bare substrate, which we found to be indistinguishable (to within experimental error) to the scattering arising from pristine graphene on an otherwise bare substrate.

Representative normalized scattering spectra from arrays of silver nanoparticles on graphene flakes and intercalated graphene flakes are shown in **Fig.96** respectively. Both figures show spectra obtained from particle arrays on top of few-layer graphene flakes consisting of different numbers of layers. For single layers of both types of graphene – pristine and intercalated – a broad (150 nm) peak is seen in the scattering spectra, centered at ~ 530 nm. This peak is a result of the localized surface plasmon resonance associated with the silver nanoparticle [280, 282]. As the number of graphene layers is increased the major difference in the scattering spectra is that the plasmon resonance becomes weaker. This attenuation of the scattering spectra with increasing number of graphene layers is highlighted in **Fig.97** from which we can see that the degree of the attenuation for the pristine graphene is somewhat greater than for the intercalated graphene. Here attenuation refers the numerical factor by which the intensity is decreased, an attenuation of 2 means the intensity is halved.
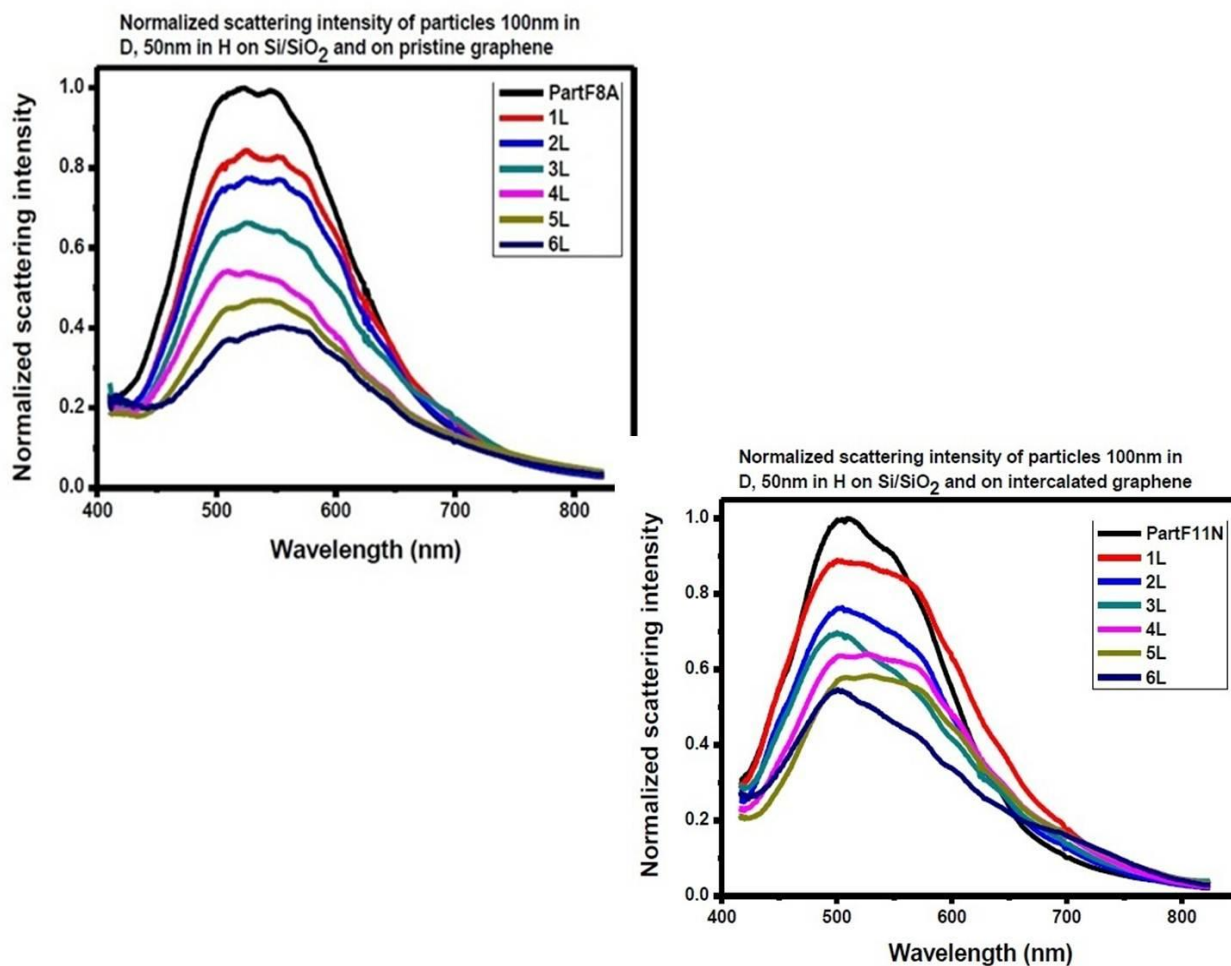
Figure 96. Experimental scattering spectra from the EBL particles on pristine graphene of different thicknesses (1 – 6 layers), and on the bare substrate(on left) and scattering spectra from the EBL particles on intercalated graphene(on right)
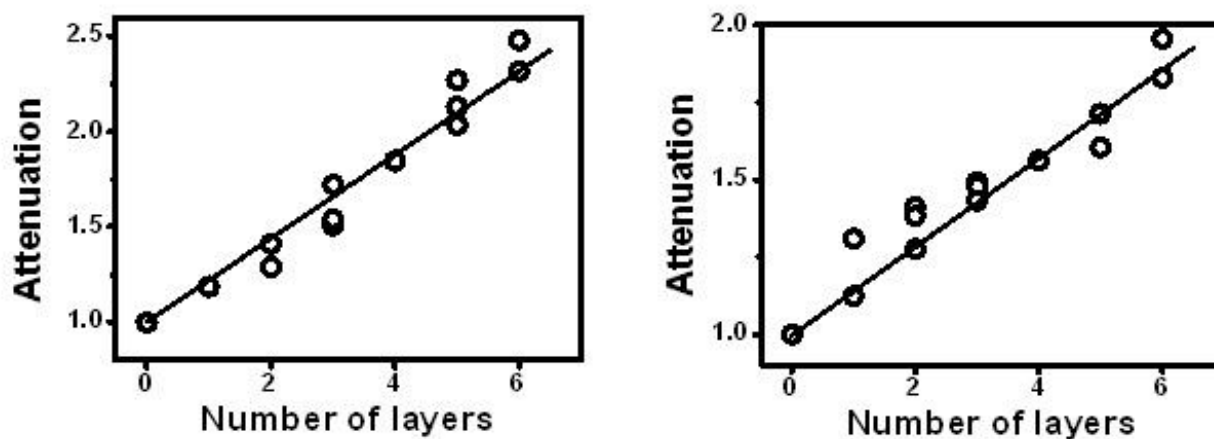

Figure 97. Extent of attenuation of the scattered intensity as a function of layer thickness. Pristine graphene on the left and intercalated on the right.

Previous experimental studies have shown that an increase of the effective refractive index (permittivity) of the region surrounding the nanoparticles, leads to a red shift in the spectral position of the particle plasmon resonance [280]. For few-layer graphene one might expect that increasing the thickness of the graphene substrate would increase the effective refractive index of the region surrounding the particle, thus leading to a red-shift in the spectral position of the plasmon resonance.

However, this expectation is in contrast with our observation that the spectral position of the plasmon resonance is only attenuated as the number of graphene layers are increased, irrespective of the graphene doping level (from 0 up to 10^{14} electrons cm^{-2}, see **Fig.96**).

This difference between expectation and observation can be explained by considering the thickness of 6 layers of graphene, it is just ~ 2nm, at least an order of magnitude less than the optical field penetration depth associated with localized surface plasmon resonances [247].

The key feature that we need to account for in these data is the decrease in scattering strength with increasing thickness of the graphene layer. One way in which the graphene can modify the scattering is to alter the strength of the optical field at the surface of the substrate – the presence of the graphene layer, of relatively high refractive index, is to alter the strength of the reflected field. This reflected field interferes with the incident field, and it is this interference that can lead to a modified strength of the field at the surface – the field that drives the scattering process. To investigate this possibility we conducted a simple calculation based on Fresnel reflection coefficients.

In the Fresnel model we incorporated the Si wafer substrate (permittivity = 16 + 0.5i) covered with a 300nm thick layer of SiO$_2$ (permittivity = 2.13 + 0.0i). We then added graphene of different thicknesses (1 – 6 layers) and finally included air above the structure. The optical constants of the graphene were taken to be n = 2.6, k = 1.3 [283] and each layer thickness to be 0.35nm.

The dark-field objective used in the experiments numerical aperture (NA) 0.90, corresponding to maximum angle of $\theta_0 = \arcsin(0.90) \approx 64°$. To collect only scattered light the structure should be illuminated at angles higher than θ_0. For comparison the results for different angles of incidence are also included, specifically data for illumination angles $\theta_1 = \arcsin(0.85)$ and $\theta_1 = \arcsin(0.95)$ (see **fig.98**).
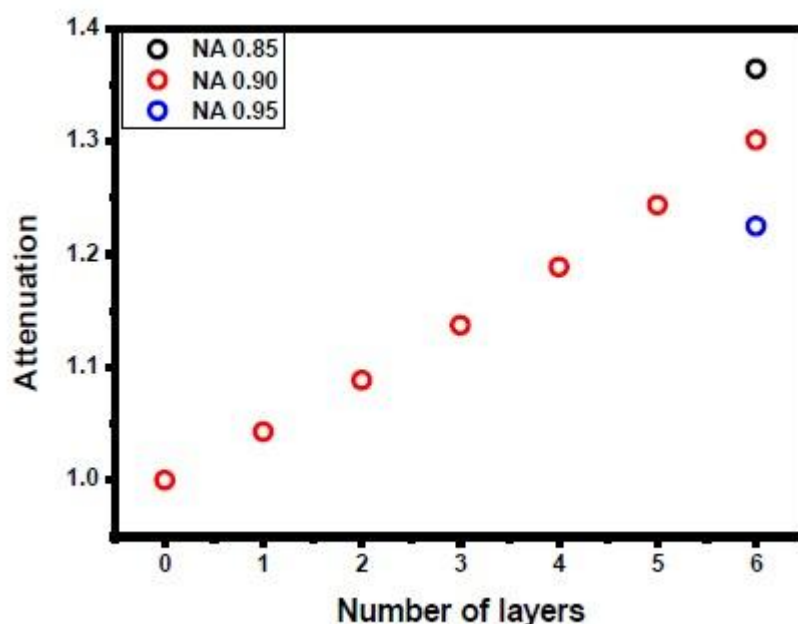

Figure 98. Calculated ratio of the relative electric field strength on the substrate/air interface, and the graphene/air interface for different numbers of layers. The data in red correspond to an incident angle of 64°. The data for 6 layers are shown also for incident angles of 58°and 72°.

These data (**fig.98**) show that one should expect an attenuation of the scattered signal as the number of graphene layers is increased, here by ~ 40 % for 6 layers. This compares with the observed attenuation of ~ 80% seen in the experimental data (**Fig.96**). The lack of quantitative agreement is to be expected, the angle dependence of the scattering process makes the quantitative comparison of dark-field spectra with numerical models an involved task [284], one that was beyond the scope of the present study.

In conclusion, we have shown that graphene can be used as an excellent substrate for plasmonic (metallic) nanoparticles. Our experiments using arrays of metallic nanoparticles produced by electron-beam lithography have shown that the plasmon resonances associated with metallic nanoparticles are retained when graphene is used as the substrate.

The motivation for this application is twofold: the field enhancement sustained by the metallic nanostructures upon resonant excitation can lead to a reduction in the threshold for achieving inversion in the optically active surrounding medium, and the presence of gain can counteract the inherent absorption losses in the metal.

Such architectures also offer a platform for biomolecule immobilization in a bio-sensing device in which electrochemical detection can be combined with two LSPR. Taken together these results show that the combination of graphene and the plasmonics of metallic nanoparticles offer great promise, for example for flexible and transparent electronics and for advanced bio- and chemical sensors.